



|              |   |
|--------------|---|
| Title        | Thermoelectric properties of InSb- and CoSb <sub>3</sub> -based compounds   |
| Author(s)    | Kim, Donghun  |
| Citation     | 大阪大学, 2013, 博士論文  |
| Version Type | VoR   |
| URL          | <a href="https://doi.org/10.18910/26171">https://doi.org/10.18910/26171</a> |
| rights       |   |
| Note         |   |

*The University of Osaka Institutional Knowledge Archive : OUKA*

<https://ir.library.osaka-u.ac.jp/>

The University of Osaka

**Doctoral Dissertation**

**Thermoelectric properties of InSb- and  
CoSb<sub>3</sub>-based compounds**  
(InSb 及び CoSb<sub>3</sub> 基化合物の熱電特性)

**DONGHUN KIM**

**July 2013**

**Graduate School of Engineering**  
**Osaka University**

# Contents

---

| Chapter  | Page |
|--|------|
| <b>I. Introduction</b> .....                                 | 1    |
| 1.1 Background.....  | 1    |
| 1.2 Thermoelectric Phenomena .....                           | 2    |
| 1.3 Figure of Merit and Thermoelectric Performance.....      | 4    |
| 1.4 The Optimization of Thermoelectric Performance .....     | 5    |
| 1.4.1 Carrier Concentration .....                            | 5    |
| 1.4.2 Effective Mass.....                                    | 7    |
| 1.4.3 Minimizing Thermal Conductivity.....                   | 7    |
| 1.5 Brief Overview on Advanced Thermoelectric Materials..... | 10   |
| 1.5.1 Classical Thermoelectric Materials .....               | 11   |
| 1.5.2 Advanced Thermoelectric Materials .....                | 13   |
| 1.6 Purpose of Present Study.....                            | 15   |
| Reference.....   | 16   |
| <br>   |      |
| <b>II. Experimental Method</b> .....                         | 19   |
| 2.1 Characterization Methods.....                            | 19   |
| 2.1.1 X-ray powder Diffraction .....                         | 19   |
| 2.1.2 Morphology of Surface Microstructure .....             | 22   |
| 2.1.3 Elastic Moduli and Debye Temperature .....             | 23   |
| 2.1.4 Electrical Resistivity and Seebeck Coefficient .....   | 24   |
| 2.1.5 Carrier Concentration and Mobility .....               | 26   |
| 2.1.6 Thermal conductivity.....                              | 27   |
| Reference.....   | 29   |

|  |     |
|--|-----|
| <b>III. Thermoelectric properties of InSb-based system</b> .....                 | 31  |
| 3.1 InSb-ZnSiSb <sub>2</sub> system .....  | 31  |
| 3.1.1 Introduction.....  | 31  |
| 3.1.2 Experimental Procedures .....  | 33  |
| 3.1.3 Results and Discussion .....   | 36  |
| 3.1.4 Conclusion .....   | 43  |
| 3.2 InSb-ZnGeSb <sub>2</sub> system .....  | 45  |
| 3.2.1 Introduction.....  | 45  |
| 3.2.2 Experimental Procedures .....  | 46  |
| 3.2.3 Results and Discussion .....   | 48  |
| 3.2.4 Conclusion .....   | 55  |
| 3.3 InSb-ZnSnSb <sub>2</sub> and InSb-ZnPbSb <sub>2</sub> system .....           | 57  |
| 3.3.1 Introduction.....  | 57  |
| 3.3.2 Experimental Procedures .....  | 58  |
| 3.3.3 Results and Discussion .....   | 60  |
| 3.3.4 Conclusion .....   | 65  |
| 3.4 InSb-In <sub>2</sub> XTe (X = Si, Ge, or Sn) system .....                    | 67  |
| 3.4.1 Introduction.....  | 67  |
| 3.4.2 Experimental Procedures .....  | 68  |
| 3.4.3 Results and Discussion .....   | 70  |
| 3.4.4 Conclusion .....   | 75  |
| Reference.....   | 76  |
| <br>   |     |
| <b>IV. Thermoelectric properties of CoSb<sub>3</sub>-based system</b> .....      | 79  |
| 4.1 Tl <sub>x</sub> Fe <sub>1</sub> Co <sub>3</sub> Sb <sub>12</sub> system..... | 79  |
| 4.1.1 Introduction.....  | 79  |
| 4.1.2 Experimental Procedures .....  | 83  |
| 4.1.3 Results and Discussion .....   | 85  |
| 4.1.4 Conclusion .....   | 92  |
| Reference.....   | 94  |
| <br>   |     |
| <b>V. Summary</b> .....  | 97  |
| <br>   |     |
| <b>Research Achievements</b> .....   | 101 |
| <b>Acknowledgements</b> .....  | 103 |

# CHAPTER I

## Introduction

### 1.1 Background

The world's energy and environment have become some of the most critical current issues. Due to the present global energy shortage and predicted increase in future energy demands, we need to develop a technology which is able to be an alternative energy conversion and transition to the post-fossil fuel era. Likewise, the environmental impact of global climate change due to the combustion of fossil fuels is becoming increasingly alarming [1]. One of the types of energy conversion technologies that has received renewed attention is thermoelectric (TE) energy conversion, where heat is converted directly into electricity using a class of materials known as TE materials. Thermoelectric generators can potentially convert waste heat in a variety of applications including home heating, automotive exhaust and industrial processes. As TE generators are solid-state devices with no moving parts, they are silent, reliable and scalable, making them an idea for small, distributed power generation [2].

However, in order to fully benefit from all the advantages of TE generators, it is required to improve the efficiency with the TE material converts heat into electricity. In the middle 1990s, theoretical predictions suggested that thermoelectric efficiency could be greatly enhanced through nano-structural engineering, which led to experimental efforts to demonstrate the proof-of-principle and high-efficiency materials [3, 4]. Although a high efficiency has been reported in nanostructured materials, many of these materials are not practical for large-scale commercial use because they are fabricated by atomic layer deposition process, making them slow and expensive to fabricate and restricting the amount of material that can be produced. At the same time, complex bulk materials (such as skutterudites, clathrates, and Zintl phases) have been explored and found that high efficiencies could indeed be obtained.

These efforts have already been made to implement TE materials instead of alternators on car engines to increase the fuel efficiency, in deep space probes for power generation from a nuclear source and in numerous other applications. Today commercially available the-state-of-art TE materials have a figure of merit ( $ZT$ ) of 0.8 and efficiency of about 5-6 % but wide commercial success of TE technology is expected when overall conversion efficiency reaches 20 % [5].

## 1.2 Thermoelectric Phenomena

Thermoelectric phenomena were discovered in the 19<sup>th</sup> century. However, because of advancements in the semiconductor technologies, practical applications for thermoelectric devices became feasible only after mid-20<sup>th</sup> century.

In 1821, Seebeck [1] noticed that the needle of a magnet is deflected in the presence of dissimilar metals that are connected (electrically in series and thermally in parallel) and exposed to a temperature gradient. The effect observed is the basis for thermoelectric power generation. As shown in Figure 1.1(a), if the junctions at the top are heated and those at the bottom are cooled, electron/hole pairs will be created at the hot end and absorb heat in the process. The pairs recombine and reject heat at the cold ends. A voltage potential, the Seebeck voltage, which drives the hole/electron flow, is created by the temperature difference between the hot and cold ends of the thermoelectric elements. The net voltage appears across the bottom of the thermoelectric element legs. The Seebeck effect forms the basis of the operation of thermoelectric couples (thermocouples) used extensively in temperature-measurement systems. Electrical connections can be made from the thermoelectric to an external load to extract power.

In 1834, Peltier [1] observed that if a current is applied across a junction of dissimilar electrically conductive materials, either heating or cooling can occur at the junction. When the current is reversed, the opposite effect is observed. Figure 1.1(b) illustrates how this occurs. Electric current is propagated by electrons in  $n$ -type materials and by holes in the  $p$ -type materials; it is also be in the form of semiconductors, metal, or semimetals. If voltage is applied in the right direction across a  $p$ - $n$  junction, electron/hole pairs are created in the vicinity of the junction. Electrons will flow away from the junction in the  $n$ -type material, and holes will flow away in the  $p$ -type material. The energy to form them comes from the

junction region, cooling it. On the opposite end, electrons and holes stream toward junctions where pairs recombine. This process releases energy and heats the junctions.

Figure 1.1(c) shows a typical thermoelectric module, which contains many thermoelectric couples consisting of  $n$ -type and  $p$ -type thermoelectric elements wired electrically in series and thermally in parallel.

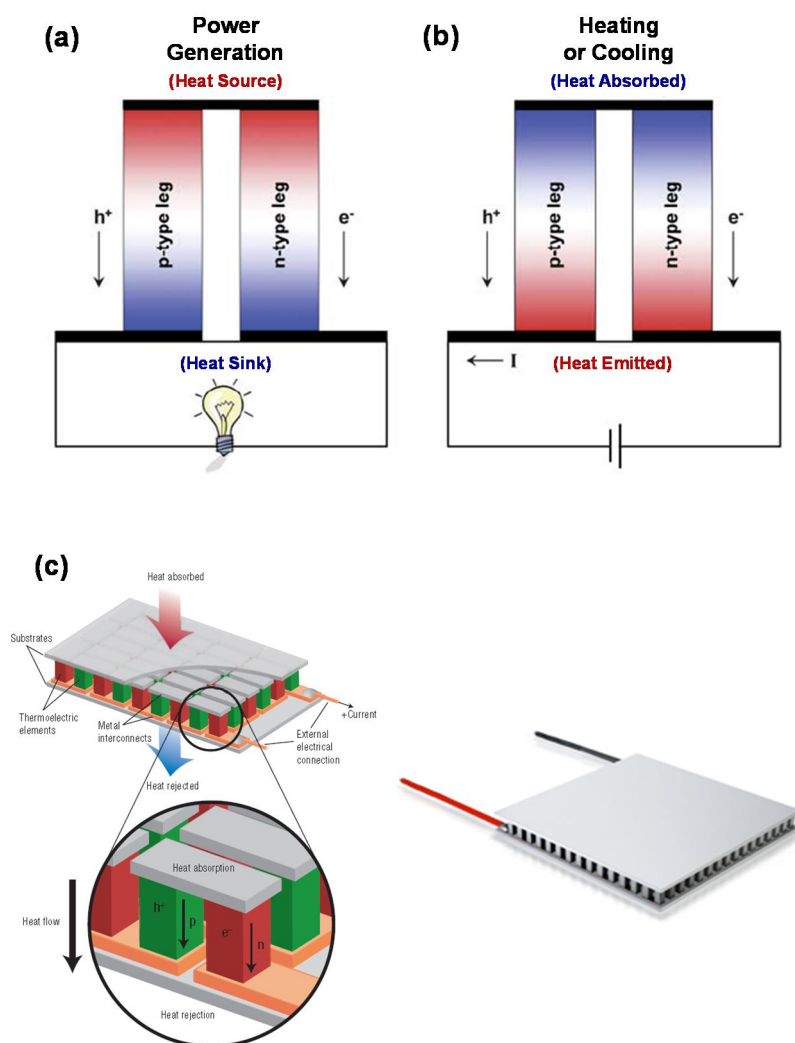


**Figure 1.1** (a) Schematic illustrations of a thermoelectric module for (b) Power generation (Seebeck effect) [6], (b) Refrigeration (Peltier effect) [6], (c) Thermoelectric modules [1].

### 1.3 Figure of Merit and Thermoelectric Performance

As the author discussed about thermoelectric devices above, it is easy to see that thermoelectric devices have many advantages. In spite of their various advantages, thermoelectric materials have not been widely used in commercial applications because of the low efficiency. The major goal of thermoelectric material research is to design materials that will improve the efficiency of these solid-state devices. The maximum efficiency ( $\eta$ ) of a thermoelectric device for power generation is defined as the output of electrical power ( $P$ ) divided by the thermal power ( $Q$ ) supplied [7]:

$$\eta = \frac{P}{Q} = \frac{T_H - T_C}{T_H} \frac{\sqrt{1 + ZT_M - 1}}{\sqrt{1 + ZT_M + \frac{T_C}{T_H}}} \quad 1.1$$

$T_H$  and  $T_C$  are referred to the temperature of hot and cold sides of the sample, and  $T_M$  is the average temperature respectively. Efficiency depends on materials properties through the thermoelectric figure of merit,  $ZT$  is given by [7]:

$$ZT = \frac{S^2 T}{\rho \kappa} \quad 1.2$$

Where  $S$  is the Seebeck coefficient,  $\rho$  is the electrical resistivity,  $\kappa$  is the thermal conductivity, and  $T$  is the absolute temperature.

The term  $(1 + ZT_M)^{1/2}$  varies with the average temperature  $T_M$ . Although the TE performance of materials was measured with a temperature dependency, the efficiency of real TE device was evaluated and used through the average temperature  $T_M$ . Generally, the higher is the figure-of-merit or  $Z$ , the higher the conversion efficiency; however, each TE material possesses high  $Z$  only with a certain temperature range, while outside it  $Z$  drops precipitously, decreasing the conversion efficiency.

Figure 1.2 shows the generating efficiency ( $\eta$ ) of the ideal thermoelectric as a function of the dimension less figure of merit ( $ZT$ ). The generating efficiency increases with increasing  $ZT$  value. Moreover, infinity  $Z$  leads to the Carnot efficiency.  $ZT = 1$  roughly means the generating efficiency of around 10 % at  $T_H = 600$  K. It has been considered that practical use of a thermoelectric material needs  $ZT = 1$ . The  $ZT = 1.5$  would translate into a 10 % increase in the fuel economy of cars if the devices are used to replace alternators in

automobiles by generating electricity from the heat in exhaust. The  $ZT = 3$  would be a 15 % increase in fuel economy of cars and trucks. To be getting up to  $ZT = 5$  or so with a cheap enough system then it can replace most of the moving parts of an engine with thermoelectric material.

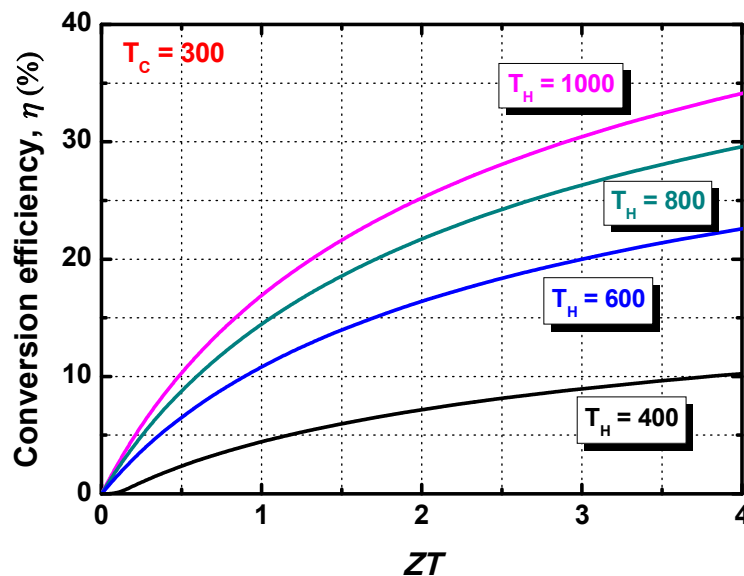


**Figure 1.2** The conversion efficiency ( $\eta$ ) as a function of thermoelectric figure of merit ( $ZT$ ) and operating temperature for ideal thermoelectric generator.

## 1.4 The Optimization of Thermoelectric Performance

Fundamental to the field of thermoelectric materials is the need to optimize a variety of conflicting properties. Again, to maximize  $ZT$  value of a material, a large  $S$  and the low  $\rho$  as well as the low  $\kappa$  are required. As these transport characteristics are interrelated with each other, a number of parameters are needed to be optimized to maximize  $ZT$ . Here, the author discusses some parameters for optimizing the thermoelectric performance.

### 1.4.1 Carrier Concentration

To ensure that the Seebeck coefficient is large, there should only be a single type of carrier. Mixed  $n$ -type and  $p$ -type conduction will lead to both charge carriers moving to the cold end, cancelling out the induced Seebeck voltages. The interrelationship between carrier

concentration and Seebeck coefficient can be seen from relatively simple models of electron transport. For metals or degenerate semiconductors, the Seebeck coefficient ( $S$ ) is given by [8]:

$$S = \frac{8\pi^2 k_B^2}{3e\hbar^2} m^* T \left( \frac{\pi}{3n} \right)^{\frac{2}{3}} \quad 1.3$$

where  $n$  is the carrier concentration and  $m^*$  is the effective mass of the carrier. Equation (1.3) shows that low carrier concentration insulators and even semiconductors have large Seebeck coefficient. However, low carrier concentration also results in low electrical conductivity; see equation (1.4). The electrical conductivity ( $\sigma$ ) and electrical resistivity ( $\rho$ ) are related to  $n$  through the carrier mobility  $\mu$ :

$$\frac{1}{\rho} = \sigma = ne\mu \quad 1.4$$

Figure 1.3 shows the compromise between large thermopower and high electrical conductivity in thermoelectric materials that must be struck to maximize the figure of merit ( $ZT$ ). This peak typically occurs at carrier concentrations between  $10^{18}$  and  $10^{21}$  carriers per  $\text{cm}^3$ , which fall in between common metals and semiconductors, that is, the concentration must be found in heavily doped semiconductors.

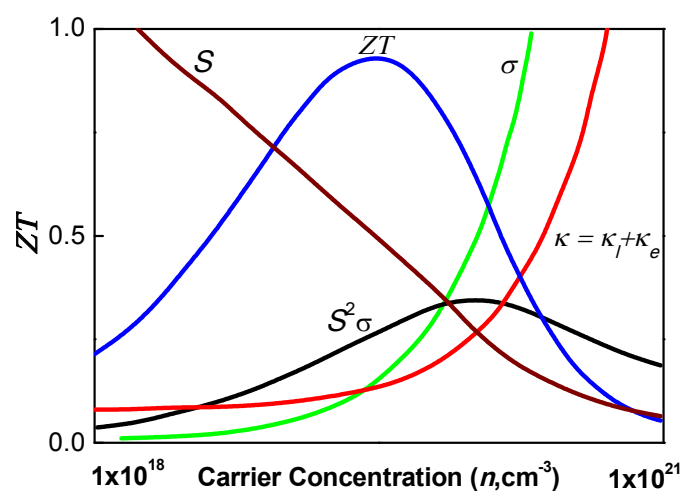


**Figure 1.3** Schematic dependence of electrical conductivity ( $\sigma$ ), Seebeck coefficient ( $S$ ), power factor ( $S^2\sigma$ ), and thermal conductivity ( $\kappa$ ) [2].

### 1.4.2 Effective Mass

The effective mass of the charge carrier provides another conflict as large effective masses produce high thermopower but low electrical conductivity. The  $m^*$  in equation (1.3) refers to the density-of-states effective mass, which increases with flat, narrow bands with high density of states at the Fermi surface. However, as the inertial effective mass is also related to  $m^*$ , heavy carriers will move with slower velocities, and therefore small mobilities, which in turn leads to low electrical conductivity (equation 1.4). The exact relationship between effective mass and mobility is complex, and depends on electronic structure, scattering mechanisms and isotropy [2].

A balance must be found for the effective mass (or bandwidth) for the dominant charge carrier, forming a compromise between high effective mass and high mobility. High mobility and low effective mass is typically found in materials made from elements with small electronegativity difference whereas high effective masses and low mobilities are found in materials with narrow bands such as ionic compounds. It is not obvious which effective mass is optimum; good thermoelectric materials can be found within a wide range of effective masses and mobilities: from low-mobility, high-effective-mass polaron conductors (oxides [9], chalcogenides [10]) to high-mobility, low-effective-mass semiconductors (SiGe, GaAs).

### 1.4.3 Minimizing Thermal Conductivity

Additional materials design conflicts stem from the necessity for low thermal conductivity. Thermal conductivity in thermoelectrics comes from two sources: (1) electrons and holes transporting heat ( $\kappa_{el}$ ) and (2) phonons travelling through the lattice ( $\kappa_{lat}$ ). Most of the electronic term ( $\kappa_{el}$ ) is directly related to the electrical conductivity through the Wiedemann-Franz law [7]:

$$\kappa = \kappa_{el} + \kappa_{lat} \quad 1.5$$

and

$$\kappa_e = \frac{\pi^2}{3} \frac{n}{m} k_B^2 T \tau, \quad \sigma = \frac{ne^2 \tau}{m}$$

and then

$$L = \frac{\kappa_{el}}{\sigma T} = \frac{\kappa_{el}}{ne\mu T} = \left(\frac{k_B}{e}\right)^2 \frac{\pi^2}{3} \approx 2.45 \times 10^{-8} [W\Omega/K^2] \quad 1.6$$

where  $L$  is the Lorenz factor for free electrons.

The Lorenz factor can vary particularly with carrier concentration. Accurate assessment of  $\kappa_{el}$  is important, as  $\kappa_l$  is often computed as the difference between  $\kappa$  and  $\kappa_{el}$  (equation 1.5) using the experimental electrical conductivity. A common source of uncertainty in  $\kappa_{el}$  occurs in low-carrier-concentration materials where the Lorenz factor can be reduced by as much as 20% from the free-electron value. Additional uncertainty in  $\kappa_{el}$  arises from mixed conduction, which introduces a bipolar term into the thermal conductivity [2, 7].

As high  $ZT$  requires high electrical conductivity but low thermal conductivity, the Wiedemann-Franz law reveals an inherent materials conflict for achieving high thermoelectric efficiency. For materials with very high electrical conductivity (metals) or very low  $\kappa_{lat}$ , the Seebeck coefficient alone primarily determines  $ZT$ , as can be described using equation (1-5), where  $\frac{\kappa_{lat}}{\kappa_{el}} \ll 1$

$$ZT = \frac{\frac{S^2}{L}}{1 + \frac{\kappa_{lat}}{\kappa_{el}}} \quad 1.7$$

In many areas of research related to new TE materials, attempts are being made to reduce the lattice part of the thermal conductivity essentially to its minimum value; that is, where a minimum lattice thermal conductivity is achieved (when all the phonons have a mean free path essentially equal to the interatomic spacing of the constituent atoms). What is the phonon? If an atom in the crystal lattice is thermally excited, the crystal bonding will pass the excitation to the neighboring atoms. Through this mechanism, heat is transported through the bulk. Because of the periodic structure of the crystal lattice, these vibration effects can be described by quasi-particles called phonons. These phonons travel through the crystal, carrying a certain amount of energy in form of heat. Considering the phonons, the representation of the lattice thermal conductivity is able to be obtained by solving the

Boltzmann equation for phonons with the same procedure as that of charged carriers, electrons.

The lattice thermal conductivity is derived by the transport properties of phonon. The transport of phonon also can be described by the relaxation time approximation. Therefore, the lattice thermal conductivity  $\kappa_{\text{lat}}$  is expressed as [2, 7, 11]

$$\kappa_{\text{lat}} = \int \tau \frac{E^2}{T} v_x^2 \left( -\frac{\partial f_B}{\partial E} \right) G(E) dE \quad 1.8$$

The distribution of phonons in thermal equilibrium state is given by the Bose distribution ( $f_B(E)$ ) as follow:

$$f_B(E) = \frac{1}{\exp\left(\frac{E}{k_B T}\right) - 1} \quad 1.9$$

where  $G(E)$ ,  $E$ ,  $v_x$ ,  $\tau$  are the phonon density of states, the energy, the group velocity, and the relaxation time of phonon scattering, respectively. The relaxation time  $\tau$  can be expressed for several scattering mechanisms by

$$\frac{1}{\tau} = \frac{1}{\tau_{PP}} + \frac{1}{\tau_{PC}} + \frac{1}{\tau_{PA}} + \frac{1}{\tau_{PG}} + \dots \quad 1.10$$

where  $\tau_{PP}$ ,  $\tau_{PC}$ ,  $\tau_{PA}$ , and  $\tau_{PG}$  are the phonon-phonon scattering by Umklapp process, the phonon-carrier scattering, the phonon-alloying scattering, and the phonon-grain boundary scattering, respectively. If  $\xi$ ,  $M$ ,  $\delta$ ,  $\gamma$ ,  $\theta_D$ ,  $N$ ,  $m^*$ ,  $v_s$ ,  $y(1-y)$ ,  $\Delta M$ ,  $\Delta r$ , and  $L$  are the Fermi energy, the average mass per atom, the cubic root of the average atomic volume, the Gruneisen parameter, the Debye temperature, the number of atom in a unit cell, the effective mass, the sound velocity, the product of alloy composition, the difference atomic mass, the difference atomic radius, and the mean free path, then either relaxation time can be explained as

$$\frac{1}{\tau_{PP}} = \frac{280}{27} \frac{\sqrt[3]{3} \pi^3}{\sqrt[3]{2}} \frac{\hbar N \gamma}{M \delta^2} \left( \frac{T}{\theta_D} \right)^{\frac{1}{3}} \xi \quad 1.11$$

$$\frac{1}{\tau_{PC}} = \frac{E^2 m^* v_s}{4\pi \hbar^4 \rho \phi} \left\langle \xi - \ln \frac{1 + \exp\left[\phi - \frac{\xi_F}{16\phi^2} + \xi/2\right]}{1 + \exp\left[\phi - \frac{\xi_F}{16\phi^2} - \xi/2\right]} \right\rangle \quad 1.12$$

$$\phi = \frac{m^* v_s^2}{2k_B T}$$

$$\tau_{PA} = \frac{1}{4\pi} \frac{\delta^3}{v_s^3} \left( \frac{k_B T}{\hbar} \right)^4 y(1-y) \left\langle \left( \frac{\Delta M}{M} \right)^2 + \varepsilon_s \left( \frac{\Delta r}{r} \right)^2 \right\rangle \xi^4 \quad 1.13$$

$$\tau_{PG} = \frac{v_s}{L} \quad 1.14$$

On the other hand, according to a model proposed by G. A. Slack [12], low lattice thermal conductivity can be expected in the materials which satisfy the conditions as a low melting point, a large average mass of its constituent atoms, and a large unit cell. In addition, the minimization of the lattice thermal conductivity is very useful in enhancing the  $ZT$  value. Empirically, the  $\kappa_{\text{lat}}$  is proportional to  $T^3$  at low temperature, has maximum at around  $0.05\theta_D$ , and be proportional to  $T^{-1}$  at high temperature. Same success in predicting high-temperature lattice thermal conductivity is achieved by G. Leibfried and E. Schomann [12]. By using a variational method, they found that

$$\kappa_{\text{lat}} \approx 3.5 \left( \frac{k_B}{\hbar} \right)^3 \frac{M\delta\theta_D^3}{\gamma} \frac{1}{T} \propto \frac{M\delta\theta_D^3}{\gamma} \frac{1}{T} \quad 1.15$$

Since  $\theta_D$  is empirically proportional to  $M^{-1}$ , so the  $\kappa_l$  becomes low with a large molecular weight. The materials with a small  $\delta$  also have a large  $N$ , where  $N$  is the number of atoms per unit cell. Therefore, a low thermal conductivity is obtained by a low  $\theta_D$  and a large  $N$ . In other words, the materials with a low lattice thermal conductivity have a large unit cell with a complex structure, a low Debye temperature and a large molecular weight. These conditions are consistent with the Slack's conditions.

## 1.5 Brief Overview on Advanced Thermoelectric Materials

During the search for good thermoelectric materials since 1950s, some material systems stand out with high potential for achieving excellent thermoelectric performances. These materials contain high electrical and thermopower, while maintaining the relatively low thermal conductivity. In the following, the author will show some conventional bulk thermoelectric materials and more recent advanced thermoelectric materials.

### 1.5.1 Classical Thermoelectric Materials

Over the past 30 years, alloy based on  $\text{Bi}_2\text{Te}_3$ ,  $\text{PbTe}$ , and  $\text{Si}_{1-x}\text{Ge}$  traditional small band gap materials system have been extensively studied. The classical approaches to achieving high values of  $ZT$  rely on strategies aimed at either increasing the power factor or decreasing the thermal conductivity.

#### **$\text{Bi}_2\text{Te}_3$ based alloys**

$\text{Bi}_2\text{Te}_3$  has been studied extensively since 1954 [13] and is one of the most widely used TE materials which is a narrow-gap semiconductor with an indirect gap of approximately 0.15 eV. Although It has been described the compound  $\text{Bi}_2\text{Te}_3$  as a rhombohedral structure of the space group ( $R\bar{3}m$ ), it is easier to represent this structure by an hexagonal cell. The hexagonal cell is formed by the stacking of layers (Te1-Bi-Te2-Bi-Te1), stacked by van der Waals interactions along the  $c$ -axis in the unit cell. The most commonly studied  $p$ -type composition are near  $(\text{Sb}_{0.8}\text{Bi}_{0.2})\text{Te}_3$  whereas  $n$ -type compositions are close to  $\text{Bi}_2(\text{Te}_{0.8}\text{Se}_{0.2})$  [14, 15]. The maximum  $ZT$  value for these materials are typically in the range of 0.8 to 1.1 with  $p$ -type materials achieving the highest values.

#### **$\text{PbTe}$**

$\text{PbTe}$  is the premiere thermoelectric material for mid-range temperature (600 - 800 K) applications. It crystallizes in the NaCl crystal structure (space group,  $Fm\bar{3}m$ ) with Pb atoms occupying the cation sites and Te forming the anionic lattice. A band gap of 0.32 eV allows it to be doped either  $n$ - or  $p$ -type with appropriate dopants. The lattice thermal conductivity of  $\text{PbTe}$  is approximately  $2.2 \text{ Wm}^{-1}\text{K}^{-1}$  at room temperature and falls at higher temperature with a  $T^{-1}$  dependence [16]. The maximum  $ZT$  value for  $\text{PbTe}$  has been reported to be 0.8 - 1.0 at about 650 K.

#### **$\text{Si}_{1-x}\text{Ge}$ alloys**

$\text{Si}_{1-x}\text{Ge}$  alloys were first used in space on the nuclear reactor and radioisotope thermoelectric generators (RTGs). Neither Si nor Ge is a good thermoelectric material, as the lattice thermal conductivity is very large ( $150 \text{ Wm}^{-1}\text{K}^{-1}$  for Si and  $63 \text{ Wm}^{-1}\text{K}^{-1}$  for Ge). The lattice thermal conductivity can be substantially reduced by alloy formation between the two

elements. The best alloy composition is  $\text{Si}_{0.7}\text{Ge}_{0.3}$ ; its thermal conductivity about  $10 \text{ Wm}^{-1}\text{K}^{-1}$ . Since the 1960s, efforts have been made to improve the  $ZT$  of SiGe alloys, with the peak  $ZT$  of  $n$ -type SiGe reaching 1 at 1173-1223 K. The addition of germanium to silicon increase  $ZT$  to technically useful values, primarily due to increased scattering of phonon associated with the random distribution of Si and Ge atoms in the alloy [17].

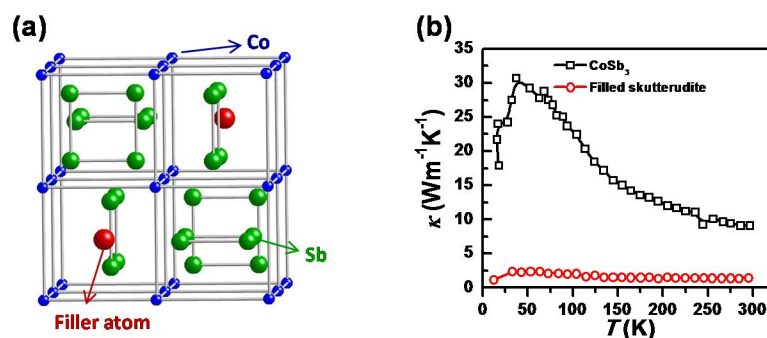


**Figure 1.6** (a) The unit cell of skutterudite structure [18]. (b) Thermal conductivity of filled skutterudite [19].

The binary skutterudites possess a  $\text{CoAs}_3$ -type structure with the general chemical formula  $\text{MX}_3$ , where M is the transition-metal Co, Rh or Ir, and X is P, As or Sb. Figure 1.6(a) shows the crystal structure of  $\text{CoSb}_3$ -based filled skutterudite. Among the skutterudite family,  $\text{CoSb}_3$  has received the most interest to day because of its higher weighted mobility  $(m^*)^{3/2}\mu$  compared to other family members, where the  $m^*$  and  $\mu$  are the carrier effective mass and mobility.  $\text{CoSb}_3$  can have a very high power factor, but its high thermal conductivity ( $10 \text{ Wm}^{-1}\text{K}^{-1}$ ) prevents it from competing with state-of-the-art  $\text{Bi}_2\text{Te}_3$  ( $1.0 - 1.5 \text{ Wm}^{-1}\text{K}^{-1}$ ). However, this compound has a specific lattice structure with a large ‘cage’ located at the center of the unit cell, which could be filled with a small metal atom. Since the cage is much larger ( $1.89 \text{ \AA}$ ) than most elemental ions, the filler is likely to rattle at the equilibrium position and hence generate significant scattering of phonons. In 1996, Sales et al. [19] reported  $\text{Ce}_{0.9}\text{Fe}_3\text{CoSb}_{12}$  and  $\text{La}_{0.9}\text{Fe}_3\text{CoSb}_{12}$  with a remarkably low  $\kappa_{\text{lat}}$  of  $1.4 \text{ Wm}^{-1} \text{ K}^{-1}$  as shown in Figure 1.6(b), one-seventh of that of unfilled  $\text{CoSb}_3$ , and a consequently high  $ZT$  of greater than 1.0. Recently, broad-ranging investigations have been carried out on  $\text{CoSb}_3$ -based TE materials with respect to both doping strategies and synthesis processes, and some innovative results have been obtained.

### 1.5.2 Advanced Thermoelectric Materials

Most of the earlier investigation mentioned so far focused on binary intermetallic semiconductor system. Recent approaches concerning high performance bulk thermoelectric materials focus on ternary and quaternary compounds as follow.

#### $\text{AgPb}_m\text{SbTe}_{m+2}$ (LAST- $m$ : lead antimony silver telluride)

$\text{AgPb}_m\text{SbTe}_{m+2}$  (LAST- $m$ : lead antimony silver telluride), reported to achieve  $ZT > 1$ , derives from the combination of PbTe and AgSbTe<sub>2</sub>. The LAST compounds possess an average NaCl structure (space group  $Fm-3m$ ) as shown in Figure 1.4(a), and could thus be considered to be antimony and silver co-doped PbTe.

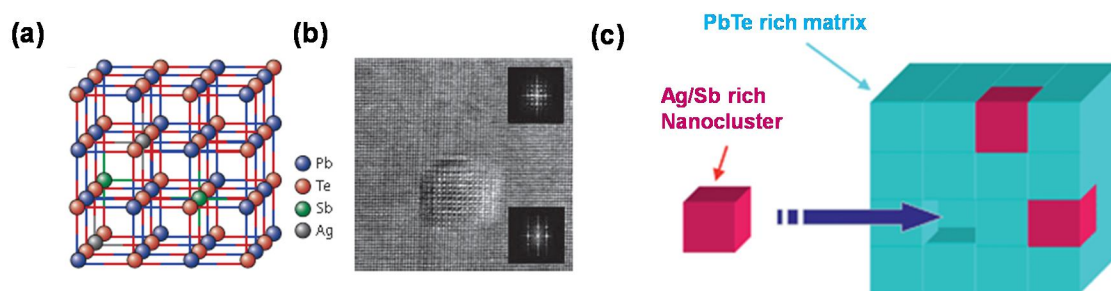


**Figure 1.4** (a) Average  $Fm-3$  structure of LAST system [20]. (b) High-resolution image of a nano-inclusion in  $\text{Ag}_{0.53}\text{Pb}_{18}\text{Sb}_{12}\text{Te}_{20}$  taken along the  $[001]$  zone axis [21]. (c) A schematic of the nanostructure of the  $\text{Ag}_{1-x}\text{Pb}_m\text{SbTe}_{m+2}$  phases [22].

This compound has been prepared a melting plus extremely slow-cooling method to develop a nanocomposite with many nanoscale inhomogeneities embedded in PbTe matrix as shown in Figure 1.4(c) and 1.4(b). The nano-inclusions correspond to the endotaxial embedding of regions of one composition inside a matrix of a different composition and preferentially orient along the  $[001]$  and appear to scatter acoustic phonon with minimal scattering of charge carrier, with the result that high figures-of-merit result. Due to the special nanostructure,  $\text{Ag}_{1-x}\text{Pb}_{18}\text{SbTe}_{20}$  showed a very high  $ZT$  value of 2.2 at 800 K [20].

#### $(\text{AgSbTe}_2)_{1-m}(\text{GeTe})_m$ (TAGS- $m$ ; telluride antimony germanium silver)

The reaction of GeTe with AgSbTe<sub>2</sub> gives alloys of the form  $(\text{AgSbTe}_2)_{1-m}\text{GeTe}_m$ . These materials have been studied for several decades and they are commonly referred to by

the acronym (TAGS- $m$ ; telluride antimony germanium silver), where  $m$  represents mole percent GeTe. The discovery of a high  $ZT$  value of approximately 1.4 and 1.5 at 750 K for  $m = 80$  and 85, respectively, motivated subsequent studies on the (GeTe)-rich compositions. The TAGS system undergoes a polymorphic transformation at 510 K, from a low-temperature polar rhombohedral ( $R3m$ ) to a high-temperature NaCl-type cubic ( $Fm-3m$ ) structure. Although twinning is pervasive in the rhombohedral structure, high-temperature X-ray diffraction and TEM analysis showed no evidence for any second phases, coherent and incoherent, in this composition. In other words, the (GeTe):(AgSbTe<sub>2</sub>) system appears to be a proper solid solution although a recent report seems to indicate nanostructuring as shown in Figure 1.5 [23].

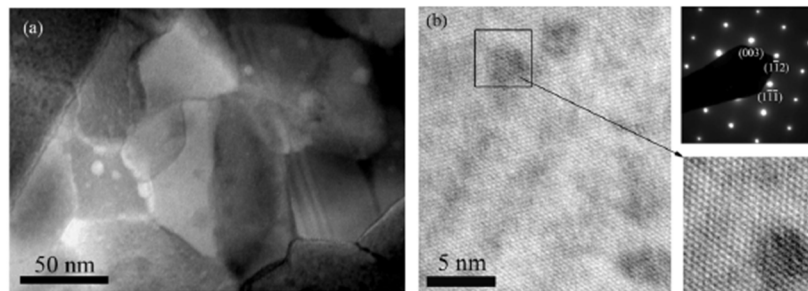


**Figure 1.5** TEM images for TAGS-80

### Half-Heusler compounds

Half-Heusler compounds are crystallized in the MgAgAs-type structure with space group  $F4-3m$ , which can be regarded as two interpenetrating cubic face-centered-cubic (FCC) motifs with a simple embedded cubic motif at the center [24]. Since half-Heusler compounds have a good combination of narrow band-gap and sharp slope of DOS near the Fermi level, a very high power factor is expected. As there are three sublattice positions in a half-Heusler compound, isoelectronic alloying on different sublattice positions is the most common approach to reducing  $\kappa$ . Compared with the PbTe or LAST systems, half-Heusler compounds are more environmentally benign and hence have attracted increasing levels of interest [25-27].

## 1.6 Purpose of the Present Study

The aim of the present study is the reduction of thermal conductivity in the materials to achieve high thermoelectric performance. Recent improvements in thermoelectric efficiency have been achieved by effort to reduce the lattice thermal conductivity through a various approaches: introducing point defects of isostructural solid solution, PGEC (phonon glass electron crystal) approach, interface scattering of phonon (nanostructured materials).

First of all, a successful strategy to increase the  $ZT$  value has been to modify an already promising compound by introducing point defect through the synthesis of isostructural solid solution. The solid solution provide an environment of atomic mass fluctuation throughout the crystal lattice (i.e. disorder) which induces strong phonon scattering and generally can lead to significantly lower thermal conductivity and a larger  $ZT$  value. A second approach was proposed by Slack [28] and is referred as the PGEC (phonon glass electron crystal) approach. A PGEC material features cages or tunnel in its crystal structure inside which reside massive atoms that are small enough relative to the cage to “rattle”. This situation produces a phonon damping effect that can result in dramatic reduction of the lattice thermal conductivity. Third, the thermal conductivity can be decreased by increasing the lattice period (i.e. large unit cell parameters) thus providing short mean path lengths for the heat carrying phonons. Finally, another approach is to grow superlattice with a nanostructured phases within a matrix material and nanostructuring bulk materials through top down approaches [18].

In the present dissertation, two approaches, point defects through the synthesis of isostructural solid solution (chapter 3), PGEC approach (chapter 4) were applied to reduce the thermal conductivity of InSb and CoSb<sub>3</sub>, respectively. In this chapter, the author has already explained the basic theories on thermoelectric conversion. In the next chapter, the author will provide some more details on the experimental technique, as well as the general physical property characteristics. In chapter 3, the author investigates the thermoelectric properties of structural derivatives of InSb. In chapter 4, thermoelectric properties of *p*-type Tl-filled skutterudite will be demonstrated. Finally, the summarizations and suggestions were described and future work was proposed in Chapter 5.

## References

- [1] G. J. Snyder and E. S. Toberer, *Nature Mater.* 7 (2008) 105.
- [2] D. M. Rowe, *CRC handbook of thermoelectrics*, (Boca Raton, FL, CRC Press, 1995).
- [3] G. Chen, M. S. Dresselhaus, G. Dresselhaus, J. P. Fleurial and T. Caillat, *Int. Mater. Rev.* 48 (2003).
- [4] M. S. Dresselhaus, G. Chen, M. Y. Tang, R. G. Yang, H. Lee, D. Z. Wang, Z. F. Ren, J. P. Fleurial and P. Gogna, *Adv. Mater.* 19 (2007).
- [5] L. E. Bell, *Science* 321 (2008).
- [6] J. R. Szczech, J. M. Higgins and S. Jin, *J. Mater. Chem.* 21 (2011).
- [7] A. F. Ioffe, *Semiconductor thermoelements, and Thermoelectric cooling*, (Infosearch, ltd., London, 1957).
- [8] M. Cutler, J. F. Leavy and R. L. Fitzpatrick, *Physical Review* 133 (1964).
- [9] K. Koumoto, I. Terasaki and R. Funahashi, *MRS Bull.* 31 (2006).
- [10] G. J. Snyder, T. Caillat and J. P. Fleurial, *Phys. Rev. B* 62 (2000).
- [11] G. S. Nolas, J. Sharp and J. Goldsmid, *Thermoelectrics: Basic Principles and New Materials Developments*, (Springer, New York, 2001).
- [12] G. A. Slack, *Solid State Physics Volume 34* (1979).
- [13] H. J. Goldsmid and R. W. Douglas, *British Journal of Applied Physics* 5 (1954).
- [14] Scherrer, *Thermoelectric Properties of BismuthAntimony Telluride Solid Solutions*, (CRC Press, 2005).
- [15] V. A. Kutasov, L. N. Lukyanova and M. V. Vedernikov, *Thermoelectric Handbook Macro to Nano*, (CRC Press, Boca Raton, 2006).
- [16] Z. H. Dughaish, *Physica B: Condensed Matter* 322 (2002).
- [17] V. Cronin, Silicon Germanium, in: *CRC Handbook of Thermoelectrics*, CRC Press, 1995.
- [18] J. R. Sootsman, D. Y. Chung and M. G. Kanatzidis, *Angew Chem Int Ed Engl* 48 (2009).
- [19] B. C. Sales, D. Mandrus and R. K. Williams, *Science* 272 (1996).
- [20] K. F. Hsu, S. Loo, F. Guo, W. Chen, J. S. Dyck, C. Uher, T. Hogan, E. K. Polychroniadis and M. G. Kanatzidis, *Science* 303 (2004).
- [21] B. A. Cook, M. J. Kramer, J. L. Haringa, M.-K. Han, D.-Y. Chung and M. G. Kanatzidis, *Adv. Funct. Mater.* 19 (2009).

- [22] P. Vaqueiro and A. V. Powell, *J. Mater. Chem.* 20 (2010).
- [23] S. H. Yang, T. J. Zhu, T. Sun, J. He, S. N. Zhang and X. B. Zhao, *Nanotechnology* 19 (2008).
- [24] J. Yang, H. Li, T. Wu, W. Zhang, L. Chen and J. Yang, *Adv. Funct. Mater.* 18 (2008).
- [25] C. Uher, J. Yang, S. Hu, D. T. Morelli and G. P. Meisner, *Phys. Rev. B* 59 (1999).
- [26] Q. Shen, L. Chen, T. Goto, T. Hirai, J. Yang, G. P. Meisner and C. Uher, *Appl. Phys. Lett.* 79 (2001).
- [27] M. Zou, J.-F. Li, B. Du, D. Liu and T. Kita, *J. Solid State Chem.* 182 (2009).
- [28] S. Glen, *New Materials and Performance Limits for Thermoelectric Cooling*, in: D.M. Rowe (Ed.) *CRC Handbook of Thermoelectrics*, CRC Press, Boca Raton, 1995.



## CHAPTER II

### Experimental Methods

#### 2.1. Characterizations Methods

##### 2.1.1 X-ray Powder Diffraction

The sample identifications were made carried out using the X-ray diffraction (XRD) technique. Figure 2.1 illustrates the basic principle of XRD according to Bragg's law [1]. Consider a set of lattice planes ( $hkl$ ), of equidistance  $d(hkl)$ . Consider an incident plane wave of wave vector  $\vec{k}_0$  and of incidence angle  $\theta$  with respect to the planes. The incident angle  $\theta$ , called the *Bragg angle*, is the complementary angle to the conventional incident angle in optics. Any points of one lattice plane ( $hkl$ ) are scattering waves being in phase in a direction  $\vec{k}$  which corresponds to the classical reflection law. If this condition is met, the optical path difference between the waves scattered by two adjacent planes is therefore the same whatever the position of the points in the planes, in particular between two points  $O$  and  $O'$  on a normal common to the planes; it follows easily from Figure 2.1 that:

$$\delta = HO + OK = 2d(hkl)\sin\theta \quad 2.1$$

The in-phase condition, called the *Bragg condition* (or Bragg law or Bragg equation), becomes accordingly

$$2d(hkl)\sin\theta = n\lambda \quad 2.2$$

where  $\lambda$  is the wavelength and  $n$  is an integer called diffraction (or reflection) order. A set of *d-spaces* obtained from a single compound will represent the set of planes that can pass through the atoms and can be used for comparison with sets of *d-spaces* obtained from standard compounds.

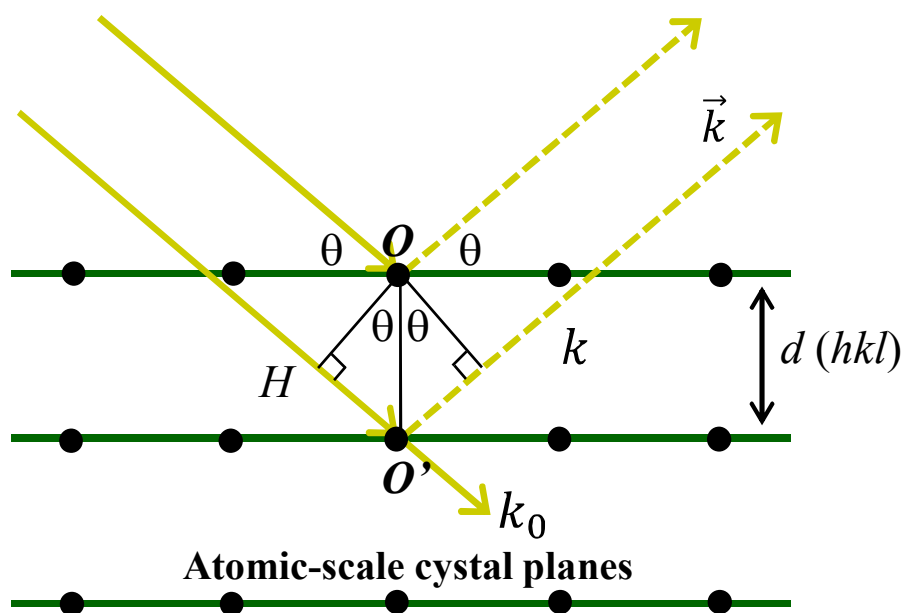


**Figure 2.1** The relationship between wavelength, atomic spacing ( $d$ ) and angle is described by the Bragg equation.

In the most common layout of the resulting powder diffractometer, the ray diagram is derived from the focusing camera, as explained by Figure 2.2. The diffractometer is operated through a continuous ( $\omega, 2\omega$ ) rotation. The amplified and integrated detector output is fed into a chart recorder with calibrated and adjustable paper speed. In recent diffractometers, the recorder is often replaced by a video display screen which enables computer processing of the diffraction pattern.

In this research, X-ray diffraction (XRD) measurements were performed on a Rigaku, RINT2000/PC series Figure 2.2 X-ray diffractometer using  $Cu-K\alpha 1$  radiation at room temperature ( $\lambda = 1.5406\text{\AA}$ ). The lattice parameter, unit cell volume and theoretical density were estimated from the XRD results. When X-ray radiation passes through the matter, the radiation interacts with the electrons in the atoms, resulting in scattering of the radiation. If the atoms are regularly organized in planes (i.e. the matter is crystalline) and the distances between the atoms are of the same magnitude as the wavelength of the X-rays, constructive and destructive interference of the scattered X-rays will occur. These result in diffraction in which X-rays are emitted at characteristic angles based on the spaces between the atomic

planes in the crystal structure. Most crystals have many sets of planes passing through their atoms. Each set of planes has a specific interlunar distance and will give rise to a characteristic angle for diffracted X-rays.

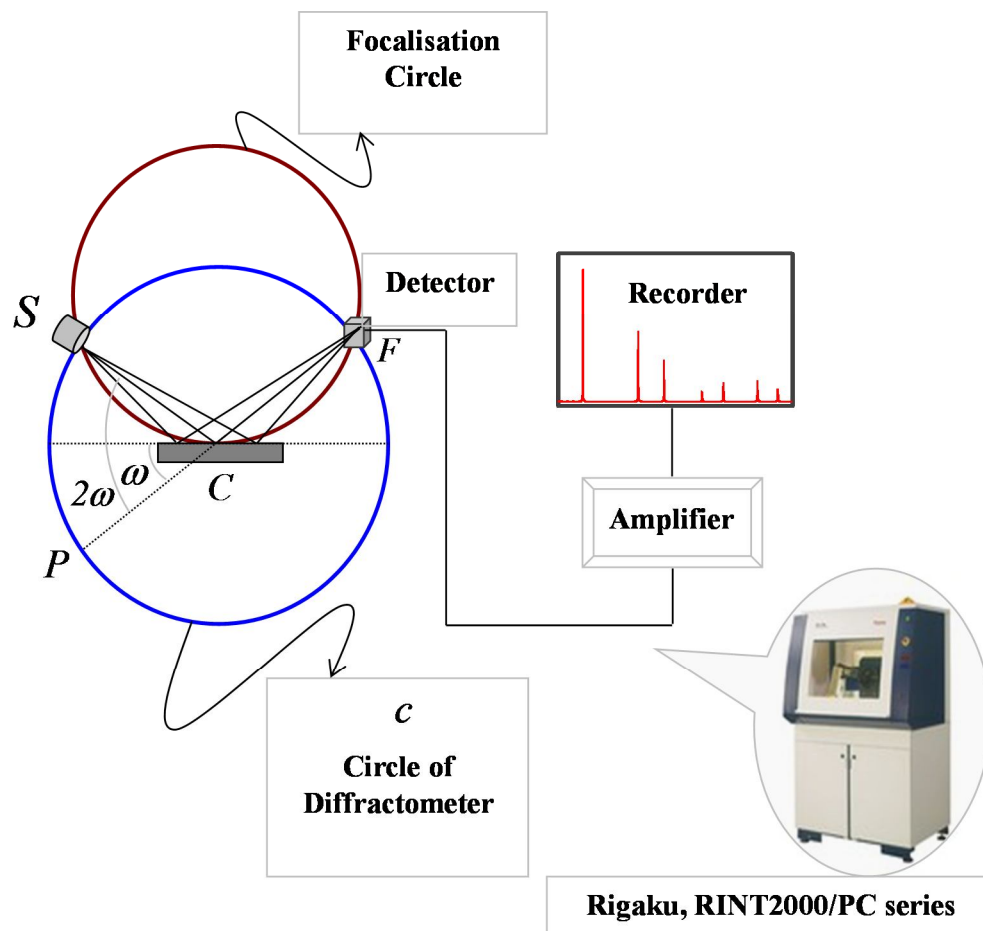


**Figure 2.2** Principle of the powder diffractometer. The line source  $S$  is placed on the circle  $c$  of the diffractometer, normal to its plane. The specimen is flat, with its reference plane passing through the diffractometer axis and rotating about this axis, at a constant and adjustable angular velocity  $\omega$ . The inlet slit  $F$  of a counter is made to move along the circle  $c$  with twice the angular velocity of the specimen, i.e.  $2\omega$ . At any moment the specimen plane is positioned so as to reflect the source  $S$  into the counter slit  $F$  [1].

### 2.1.2 Morphology of the Surface Microstructure

The surface microstructure measurements were revealed by the Scanning electron microscopy (SEM). The SEM was assessed as early as 1935 by Knoll [1], i.e. at about the same time and by the same research group as the conventional TEM. Whereas the later soon developed, the SEM had to wait until the 1960s for practicing the implementation. Its development has been closely linked to the progress of electronics and video techniques. The SEM was used to observe microstructures of the samples. In this thesis, the SEM observations were performed on a Hitachi High Technologies, S-2600H. The schematic diagram of the SEM equipment is shown as outlined in Figure 2.3.

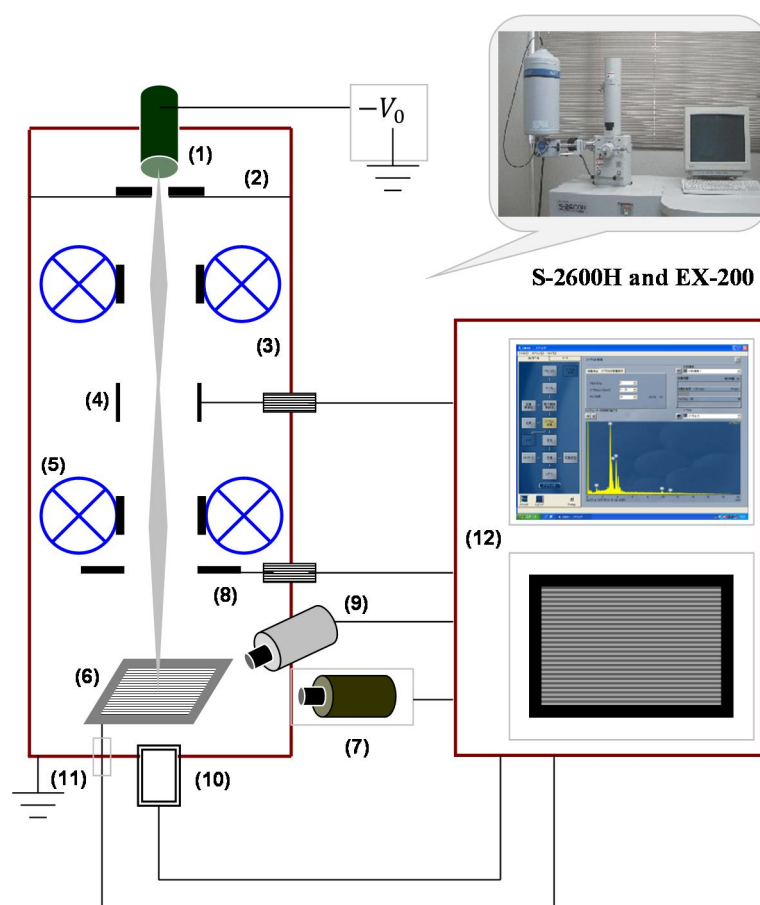


**Figure 2.3** Diagram of an SEM. (1) Electron source at negative high voltage ( $-V_0$ ); (2) grounded anode; (3) condenser lenses; (4) beam deflection and scanning system; (5) objective lens; (6) specimen on a goniometric stage; (7) electron detector; (8) backscattered electron detector; (9) X-ray spectrometer (EDS); (10) transmitted electrons detector; (11) absorbed current measurement; (12) control unit, data acquisition and processing, display screen [1].

### 2.1.3 Elastic Moduli and Debye Temperature

The elastic moduli are consisting of the shear modulus ( $G$ ), Young's modulus ( $E$ ), Bulk modulus ( $K$ ), Bulk compressibility ( $\beta$ ), and Debye temperature ( $\theta_D$ ). These parameters are evaluated from sound velocities of the samples. The sound velocities, i.e. longitudinal velocity ( $V_L$ ) and shear velocity ( $V_S$ ), of the sample were measured by an Ultrasonic pulse echo method (Nihon Matech, Echometer 1062). The schematic view of the apparatus is shown in Figure 2.3.

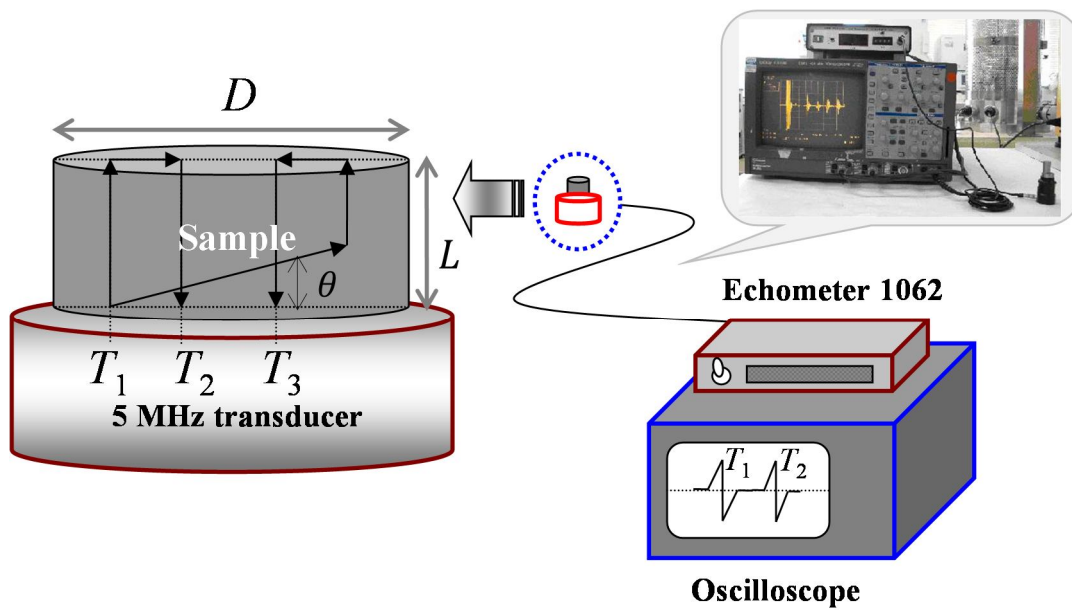


**Figure 2.3** Schematic view of the Ultrasonic pulse echo method and Nihon Matech, Echometer 1062.

The sound velocities in the sample can be calculated from the sample length and the time separation between the ultrasonic echoes [2]. The longitudinal sound velocity ( $V_L$ ) and shear sound velocity ( $V_S$ ) are described by the following equation:

$$V_L = \frac{2L}{T_2 - T_1} \quad 2.3$$

$$V_S = \left[ \left( \frac{T_3 - T_2}{D} \right)^2 + \left( \frac{T_2 - T_1}{2L} \right)^2 \right]^{-\frac{1}{2}} \quad 2.4$$

In equation (2.3) and (2.4),  $T_1$  is the reflection time of the longitudinal sound velocity from the bottom face of the sample,  $T_2$  is the reflection time of the longitudinal sound velocity from the top face of the sample,  $T_3$  is the reflection time of the shear sound velocity from the top face of the sample,  $D$  is the diameter of the sample, and  $L$  is the length of the sample. A 5.0 MHz longitudinal wave pulse and shear wave pulse were used for measuring the longitudinal sound velocity ( $V_L$ ) and the shear sound velocity ( $V_S$ ), respectively.

In case of isotropic materials, the Debye temperature ( $\theta_D$ ) [3], Shear modulus ( $G$ ), Young's modulus ( $E$ ), and Bulk compressibility ( $\beta$ ) can be evaluated:

$$\theta_D = \left(\frac{h}{k_B}\right) \left[\frac{9N}{4\pi V(V_L^{-3} + 2V_S^{-3})}\right]^{\frac{1}{3}} \quad 2.5$$

$$G = dV_S^2 \quad 2.6$$

$$E = G \left[\frac{3V_L^2 - 4V_S^2}{V_L^2 - V_S^2}\right] \quad 2.7$$

and

$$\beta = \frac{1}{d(V_L^2 - \frac{3}{4}V_S^2)} \quad 2.8$$

where  $h$  is the Plank's constant,  $k_B$  is the Boltzmann constant,  $N$  is the number of atoms in a unit cell, and  $V$  is the unit cell volume.  $d$  is total density.

#### 2.1.4 Electrical Resistivity and Seebeck Coefficient

The electrical resistivity ( $\rho_{Sample}$ ) measurement was performed in a helium atmosphere using the thermopower measuring device (ULVAC ZEM-1). The schematic view of equipment is shown in Figure 2.4.

The electrical resistivity was measured by the standard four probe method with a constant current of approximately 100 mA. The electrical resistivity is represented by the following equation [4]:

$$\rho_{Sample} = \frac{V_{Sample}}{V_{Ref}} R_{Ref} \frac{A_{Sample}}{L_{Sample}} \quad 2.9$$

In Equation (2.9),  $V_{Sample}$  is the measured voltage between two probes placed on the sample,  $R_{Ref}$  is a standard resistor incorporated into the equipment,  $V_{Ref}$  is the voltage dropped across the standard resistor,  $A_{Sample}$  is the cross section of the sample, and  $L_{Sample}$  is the distance between two thermocouples on the sample. The Seebeck coefficients were also measured using ULVAC ZEM-1 in helium atmosphere and over the temperature range of 300-730 K. The Seebeck coefficient ( $S$ ) is given by the following equation:

$$S = \frac{V_{Sample}}{T_H - T_L} \quad 2.10$$

In Equation (2.10),  $V_{Sample}$  is the Seebeck voltage developed between two points on the sample, along the direction of the temperature gradient.  $T_H$  and  $T_L$  are the measured absolute temperatures at the two points from which  $V_{Sample}$  was measured. The measurement was carried out by applying three temperature gradients of  $\Delta T$ : 20, 30, and 40 K between two blocks at each temperature  $T$ , the average value of three data is used as the experimental value.

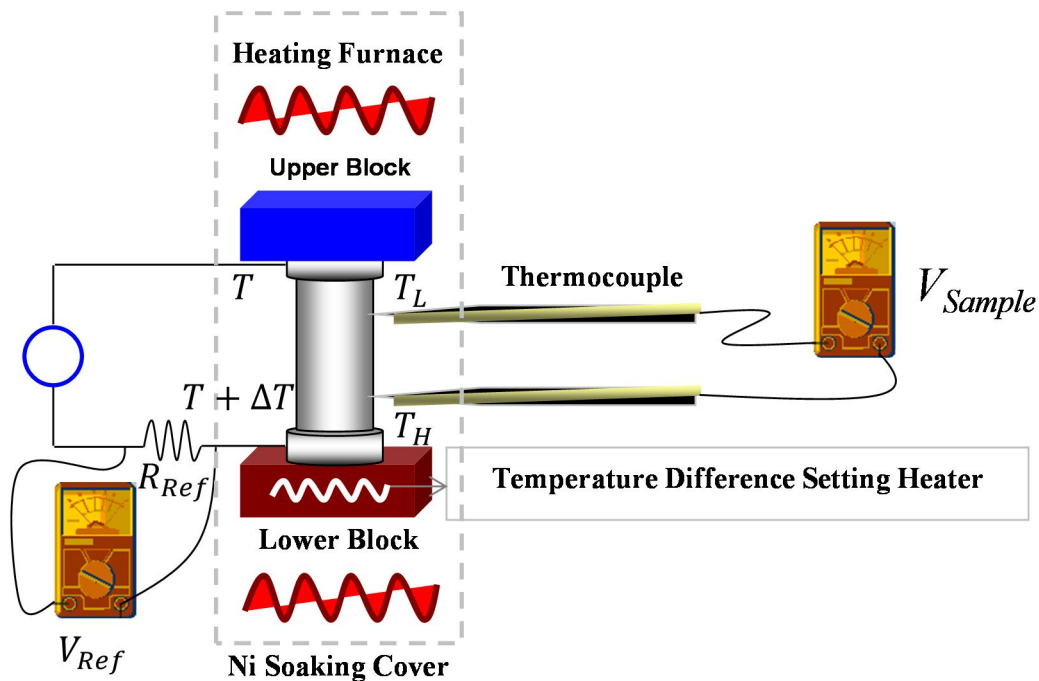


**Figure 2.4** Diagrams of the electrical properties and the Seebeck coefficient measurement using ULVAC ZEM-1 in helium atmosphere.

### 2.1.5 Carrier Concentration and Mobility

Hall measurement was carried out by van der Pauw method [5]. In general, an arbitrary shaped thin-plate sample is used, and must not contain holes, and nonconducting islands and inclusion. The sample shape was square ( $\sim 8 \times 8 \text{mm}^2$ ) with the thickness of  $\sim 1 \text{mm}$ , and probes were contacted on four corners of the surface of the sample through ohmic contacts. The electrical resistivity ( $\rho$ ) and sheet resistance  $R_{sheet}$  are calculated by the following equations:

$$\rho = \frac{\pi L_3 R_a + R_b}{\ln 2} F \quad 2.11$$

and

$$R_{sheet} = \frac{\rho}{L_3} \quad 2.12$$

where  $L_3$  is the sample thickness,  $R_a$  and  $R_b$  are the averages of the opposite side resistances, and  $F$  is the balance factor, The  $F$  value can be regressively calculated from

$$\sinh\left(\frac{r_{ratio} - \ln 2}{r_{ratio} + 1F}\right) = \frac{1}{2} \exp\left(\frac{\ln 2}{F}\right), 0 \leq F \leq 1 \quad 2.13$$

The  $r_{ratio}$  is equal to  $|R_a/R_b|$ . Then, the Hall coefficient  $R_H$  is given by

$$R_H = \frac{L_3 V_H}{B I_s} = \frac{L_3}{B} \left| \frac{R_c + R_d}{2} \right| \quad 2.14$$

where  $V_H$  is the measured Hall voltage,  $B$  is the applied magnetic field,  $I_s$  is the electric current, and  $R_c$  and  $R_d$  are the averages of the Hall resistances for each electric current direction. The noise ratio  $N_{ratio}$  and direction dependence  $D_{ratio}$  are determined by the following equations:

$$N_{ratio} = \frac{2N_{cd}}{|R_c + R_d|} \times 100 [\%] \quad 2.15$$

and

$$D_{ratio} = \frac{|R_c - R_d|}{|R_c + R_d|} \times 100 [\%] \quad 2.16$$

where  $N_{cd}$  represents the root-mean-square deviation of  $(R_c+R_d)/2$ . The  $D_{ratio}$  is the indicator to represent sample nonuniformity. In this study, the author used the measured  $R_H$  as the analytical data, if  $N_{ratio} \leq 3\%$  and  $D_{ratio} \leq 5\%$ .

### 2.1.6 Thermal Conductivity

The thermal properties of the bulk samples can be measured by the laser flash thermal diffusivity (LFTD) method. The laser flash method is by far the most favored for measuring the thermal diffusivity ( $\alpha$ ) of bulk samples at temperatures well above ambient. A typical apparatus is shown in Figure 2.5. The sample, typically a wafer, whose diameter is much greater than the thickness ( $L$ ), is irradiated on one face with pulses of laser light not more than a millisecond long. The temperature of the opposite face of the sample is monitored, perhaps with an infrared sensor.

In this thesis, the systems of measurement on thermal diffusivity ( $\alpha$ ) by laser flash method (Thermal-constantan Analyzer, ULVAC, TC 7000) in vacuum (Figure 2.5). In the complete absence of heat loss from the sample, the temperature would rise monotonically to a limiting value. In a real situation, the measured temperature will peak and then return to ambient temperature. The time required to reach one-half of the peak temperature at the rear face of the specimen,  $t_{\frac{1}{2}}$  can be used to determine  $\alpha$  according to [4]

$$\alpha = \frac{1.37L^2}{\pi^2 t_{\frac{1}{2}}} \quad 2.17$$

The thermal conductivity ( $\kappa$ ) is calculated from the temperature rise vs. time profile. The thermal diffusivity is related to the thermal conductivity as shown below:

$$\kappa = \alpha d C_p \quad 2.18$$

where  $\kappa$  is the thermal conductivity of the specimens,  $d$  is the experimental density, and  $C_p$  is the heat capacity.

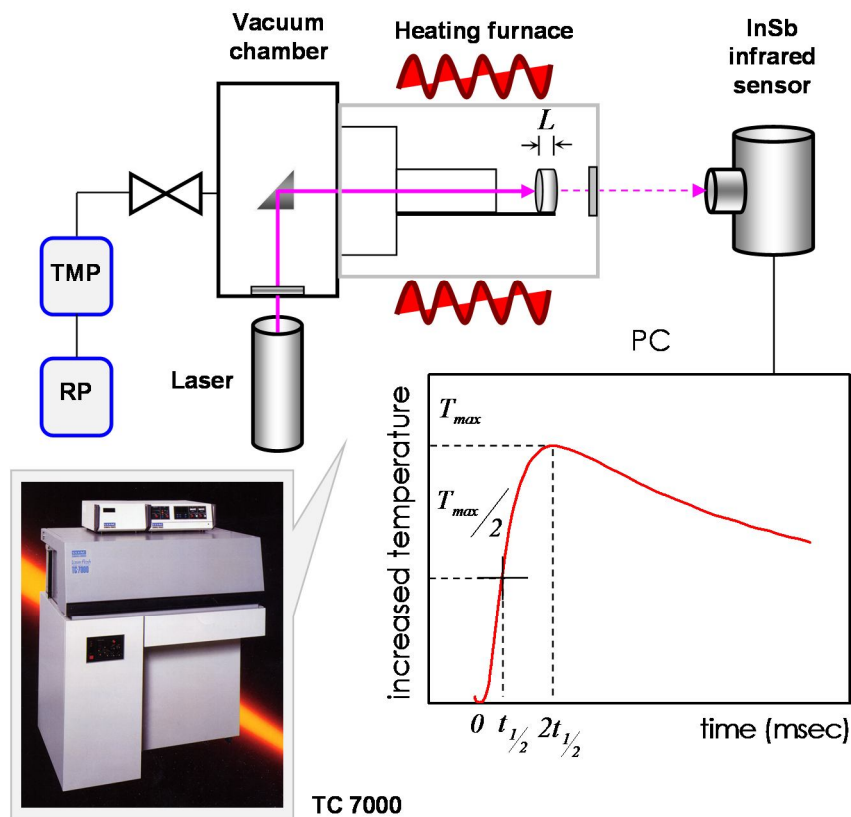


**Figure 2.5** Schematic view of the laser flash method.

The densities ( $d$ ) of the samples were calculated from the measured weight and dimensions. Density is a measure of mass per unit of volume. The higher an object's density, the higher its mass per volume. A denser object (such as iron) will have less volume than an equal mass of some less dense substance (such as water). The unit of density is the kilogram per cubic meter ( $\text{kg/m}^3$ )

$$d = \frac{m}{V} \quad 2.19$$

where  $m$  is total mass and  $V$  is the total volume

The heat capacity ( $C_p$ ) approaches the classical value  $3nR$  at high temperature, i.e. above the Debye temperature, while at low temperature  $C_p$  varies according to the  $T^3$  law of Debye [6]. In the research,  $C_p = 3nR$  is used for estimated the heat capacity of the samples.

## References

- [1] J. Gilfrich, X-Ray Spectrom. 22 (1993).
- [2] S. Yamanaka, A. Kosuga and K. Kurosaki, J. Alloys Compd. 350 (2003).
- [3] H. Inaba and T. Yamamoto, Netsu Sokutei 10 (1983) 132.
- [4] D. M. Rowe, *CRC handbook of thermoelectrics*, (Boca Raton, FL, CRC Press, 1995).
- [5] L. J. v. d. Pauw, Philips Tech. Rev. 20 (1958) 220.
- [6] G. A. Slack, Solid State Physics Volume 34 (1979).



## CHAPTER III

### Thermoelectric Properties of InSb-based System

#### 3.1 InSb-ZnSiSb<sub>2</sub> System

##### 3.1.1 Introduction

InSb (indium antimonide) has a narrow band gap of 0.18 eV at room temperature, and its electron mobility ( $77,800 \text{ cm}^2\text{V}^{-1}\text{s}^{-1}$ ) and power factor are the highest among III-V semiconductor such as GaAs, InP, InSb and InAs [1-3]. Hence, it has been considered to be a good candidate as a thermoelectric (TE) material. However, a high  $ZT$  value has not been achieved in InSb because of its high thermal conductivity ( $\kappa$ ) of  $\sim 17 \text{ Wm}^{-1}\text{K}^{-1}$ . [4] Thus, most research on InSb-based TE materials has focused on reducing its large  $\kappa$  [3, 5-7].

Substitution of other elements into a crystal lattice is known to be an effective method for enhancing phonon scattering due to the differences in atomic mass and size between the host and impurity atoms [1, 8]. Solid solutions with the same crystal structure show good performance in the TE system, e.g., PbTe-PbSe, Bi<sub>2</sub>Te<sub>3</sub>-Bi<sub>2</sub>Se<sub>3</sub>, InSb-GaSb, and Si-Ge [9-12] systems. Recently, Skoung *et al.* synthesized a copper-based ternary solid solution to reduce  $\kappa_{\text{lat}}$  and improve TE properties [8]. Moreover, the AgPb<sub>*m*</sub>SbTe<sub>*m+2*</sub> (LAST-*m*, LAST for lead antimony silver tellurium) system has attracted great attention due to its high  $ZT$  value of 1.7 at 700 K by a high power factor and rather low  $\kappa_{\text{lat}}$  [13]. The LAST compounds possess an average NaCl structure (*Fm-3m*), and could thus be considered to be antimony and silver co-doped PbTe. In the LAST-*m* system, the Pb<sup>2+</sup> ions are partly replaced by Ag<sup>1+</sup> and Sb<sup>3+</sup> ions to form alloys of AgPb<sub>*m*</sub>SbTe<sub>*m+2*</sub>, which leads to the formation of Ag-Sb nano-inclusions.

Against this background, in the present study, we prepared isostructural and isoelectronic solid solution of InSb, i.e.,  $\text{In}^{3+}$  in InSb was partly replaced by a bivalent ion and a tetravalent ion. InSb and II-IV-Sb<sub>2</sub> compounds have the zinc-blende (e.g.,  $Fm-3m$ ) and the chalcopyrite (e.g.,  $I-42d$ ) structures as shown in Figure 3.1, respectively. The chalcopyrite structure can be considered as a superlattice of the zinc-blende structure, in which two kinds of cations are ordered on the two different cation sites. If these systems show perfect stoichiometry, they may be expected to show low  $\kappa$  due to scattering of phonons by impurities and inclusions in the matrix. Thus, these isostructural and isoelectronic substitutions would be expected to result in reduced  $\kappa_{\text{lat}}$  and enhancement of the TE properties of InSb. Polycrystalline samples of  $\text{ZnIn}_{18}\text{SiSb}_{20}$  were prepared by solid state reaction and hot-pressing. Additionally, we investigated the TE properties of samples cooled at different rates because it is well known that the TE performance of the LAST- $m$  ( $m = 18$ ) system is sensitive to the fabrication conditions and procedure, in particular, the cooling rate and the annealing time. The different cooling conditions may be expected to show the different microstructure, as well as affect the TE performance.

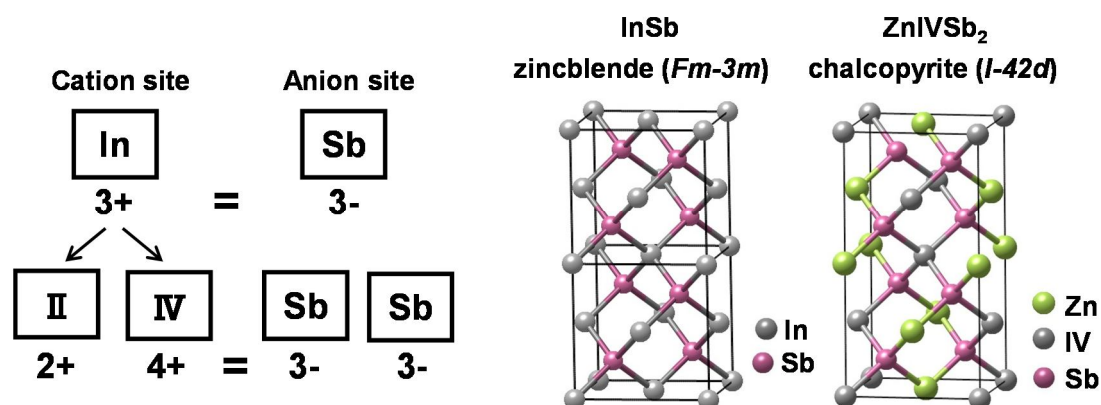


**Figure 3.1** Schematic diagrams of the isoelectronic substitution and crystal structures of InSb (zincblende) and ZnIVSb<sub>2</sub> (chalcopyrite).

### 3.1.2 Experimental Procedure

#### 3.1.2.1 Sample Preparation

The synthesis of the polycrystalline samples of ZnIn<sub>18</sub>SiSb<sub>20</sub> prepared from the starting materials was chunks of InSb (99.999 %), Zn (99.99 %), Si (> 99.99 %), and Sb (99.99 %). The starting materials were weighed out in a stoichiometric ratio and loaded into the silica tubes which were covered by carbon sheet. The silica tube was sealed under vacuum and transferred into a programmable furnace. The silica tube was heated to 1273 K at 5 K/min and kept for 12 h, and annealed at 783 K for 3 days to correct crystallographic phase. The completely reacted solid was removed from the silica tube and cleaned to remove small amounts of carbon from the surface. The obtained ingots of ZnIn<sub>18</sub>SiSb<sub>20</sub> were crushed into fine powders. The as-prepared powders of ZnIn<sub>18</sub>SiSb<sub>20</sub> were sintered by hot pressing in graphite dies under pressure of 45 MPa at a temperature slightly below the melting temperature of InSb for 1.5 h under flowing Ar. The hot-pressed samples were quenched or slowly cooled after annealing at 783 K for 72 h. The details of the temperature profile are shown in Figure 3.2. The bulk samples were cleaned the surface for measuring the weight and dimensions.

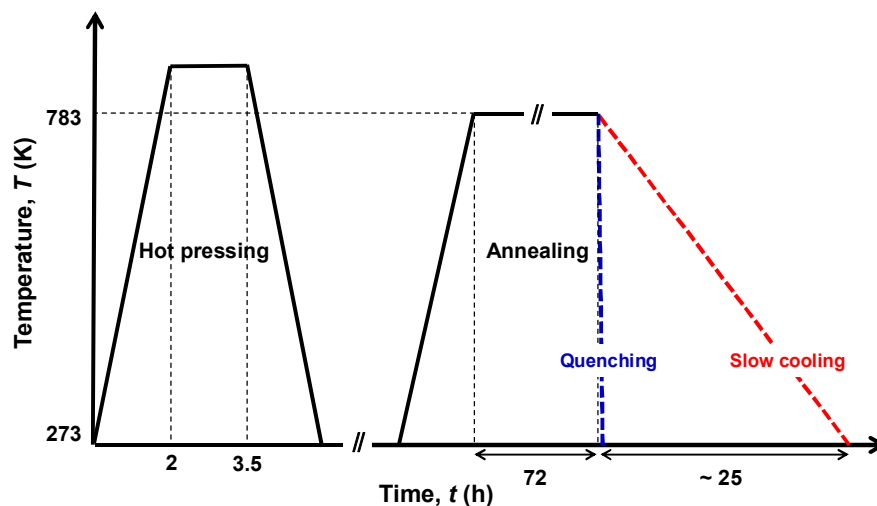


**Figure 3.2** Temperature profile for the hot pressing and annealing process.

### 3.1.2.2 Experimental Details

#### 3.1.2.2.1 X-ray Diffraction Analysis

X-ray diffraction (XRD) measurements were performed on a Rigaku, RINT2000 series X-ray diffractometer using Cu-K $\alpha$  radiation at room temperature. The powder X-ray diffraction patterns were taken from 10 to 120°. The lattice parameter, unit cell volume and theoretical density were estimated from the XRD results.

#### 3.1.2.2.2 Electrical Resistivity and Seebeck coefficient

The electrical resistivity ( $\rho$ ) and the Seebeck coefficient ( $S$ ) were performed by using a commercially available apparatus ULVAC, ZEM-1 in a helium atmosphere and over the temperature range of 300 to 723 K.

#### 3.1.2.2.3 Carrier Concentration and Mobility

The Hall effect was measured by the van der Pauw method using a dc Hall effect measurement apparatus Resitest8300 (Toyo Technica) in vacuum at room temperature under an applied magnetic field of 0.5 T.

#### 3.1.2.2.4 Thermal Diffusivity

The thermal diffusivity was performed by the laser flash method using ULVAC, TC-7000 in vacuum and over the temperature range of 300 to 723 K. The thermal conductivity ( $\kappa$ ) of the specimens was evaluated from the thermal diffusivity ( $\alpha$ ), the heat capacity ( $C_P$ ) and the experimental density ( $d$ ) using the following relationship ( $\kappa = \alpha C_P d$ ).

#### 3.1.2.2.5 Heat Capacity

The heat capacity ( $C_P$ ) of the sample was estimated from the Dulong-Petit model,  $C_P = 3nR$ , where  $n$  is the number of atoms per formula unit and  $R$  is the gas constant.

#### 3.1.2.2.6 Density

The densities ( $d$ ) of the samples were calculated on the basis of the measured weight and dimensions. Density is a measure of mass per unit of volume. The unit of density

is the kilogram per cubic meter (kg/m<sup>3</sup>). To obtain accurate densities, the measurements were performed several times after careful polishing of all samples.

#### **3.1.2.2.7 Scanning Electron Microscopy**

The Field Emission Scanning Electron Microscopy (FE-SEM) was used to observe microstructures of the samples. The FE-SEM observations were performed on a JEOL, JSM-6500F in vacuum at room temperature.

#### **3.1.2.2.8 Energy Dispersive X-Ray Spectroscopy**

Energy Dispersive X-ray spectroscopy (EDX) is a micro-analytical technique that uses the characteristic spectrum of X-rays emitted by the specimen after excitation by high-energy electrons to obtain information about its elemental composition. The EDX analysis here was performed on a JEOL, JSM-6500F in vacuum at room temperature.

#### **3.1.2.2.9 Dimensionless Figure of Merit**

The dimensionless figure of merit ( $ZT$ ) was calculated by using the above mentioned values of the Seebeck coefficient ( $S$ ), electrical resistivity ( $\rho$ ) and thermal conductivity ( $\kappa$ ), according to the relation  $\left(ZT = \frac{S^2T}{\rho\kappa}\right)$ .

### 3.1.3 Results and Discussion

#### 3.1.3.1 Sample identification

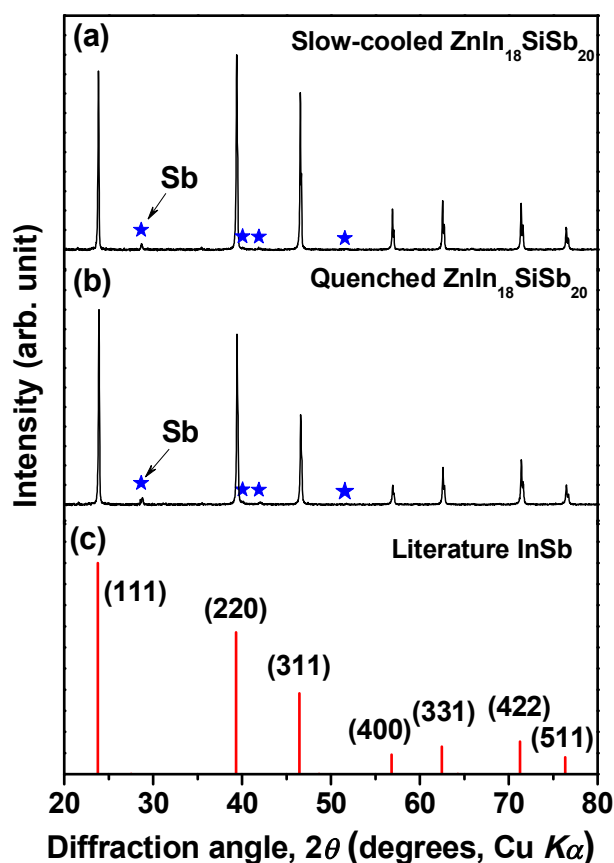


**Figure 3.3** XRD pattern of the  $\text{ZnIn}_{18}\text{SiSb}_{20}$  samples: (a) slow-cooled sample, and (b) quenched sample, and the literature  $\text{InSb}$ .

Figure 3.3(a) and 3.3(b) show the XRD patterns of the slow-cooled and quenched  $\text{ZnIn}_{18}\text{SiSb}_{20}$  samples, respectively. The XRD patterns of both samples were identified to have mainly zincblende structure, but they contained a small amount of Sb as impurities owing probably to a segregation of excess Sb or lost as a vapor phase during hot-pressing and annealing process.

To investigate the TE properties of  $\text{ZnIn}_{18}\text{SiSb}_{20}$  prepared under different cooling conditions, slow-cooled and quenched samples were prepared after hot-pressing process. In practically, it has been known that the synthesis conditions affect the performance of TE materials. The microstructures of the hot-pressed  $\text{ZnIn}_{18}\text{SiSb}_{20}$  samples with different cooling conditions are shown in Figure. 3.4.

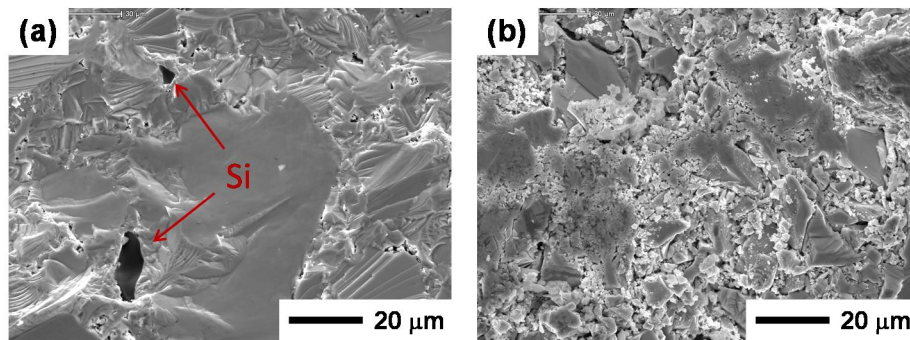


**Figure 3.4** Microstructures of the ZnIn<sub>18</sub>SiSb<sub>20</sub> samples: (a) slow-cooled sample, and (b) quenched sample.

The difference in cooling rate led to remarkably different microstructures. The grain size and the extent of the secondary phase, likely due to a phase separation, depended on the cooling rate. An increase in the cooling rate will result in smaller grain sizes and high homogeneity. As shown in Figure 3.4(a), 3.4(b), it was confirmed that the grain size of the slow-cooled sample was much larger than that of the quenched sample. This different grain size may affect not only the electrical properties but also the  $\kappa$  value for the ZnIn<sub>18</sub>SiSb<sub>20</sub> samples. Si precipitates as a minor phase existed in the slow-cooled sample, as indicated by arrows in Figure 3.4(a). It was confirmed that the substitution of Zn and Si was not complete in the slow-cooled sample.

**Table 3.1** Lattice parameters, sample densities, results of Hall measurements, and chemical compositions of the quenched and slow-cooled  $\text{ZnIn}_{18}\text{SiSb}_{20}$  samples.

|   | Sample name                                 |  |
|---|---|--|
|   | Quenched $\text{ZnIn}_{18}\text{SiSb}_{20}$ | Slow-cooled $\text{ZnIn}_{18}\text{SiSb}_{20}$ |
| Lattice parameter, $a$ (nm)   | 0.6462                                      | 0.6467   |
| Theoretical density, $d$ ( $\text{gcm}^{-3}$ )                              | 5.62  | 5.62   |
| Relative density (%)  | 93  | 93   |
| Carrier concentration, $n$ ( $10^{20}\text{cm}^{-3}$ )                      | 3.52  | 4.41   |
| Mobility, $\mu$ ( $\text{cm}^2\text{V}^{-1}\text{s}^{-1}$ )                 | 50.4  | 63.9   |
| Chemical composition of matrix phase determined through EDX analysis (at %) |   |  |
| Zn  | 1.2   | 1.4  |
| Si  | 2.1   | 0.5  |
| In  | 47.1  | 47.9   |
| Sb  | 49.6  | 50.2   |

The lattice parameters, sample bulk densities, results of Hall measurements, and chemical compositions of the samples are summarized in Table 3.1. The lattice parameters of both samples were smaller than that of InSb (0.6479 nm), due to the substitution of Zn and Si into the In sites of InSb. However, the lattice parameter of the slow-cooled sample was larger than that of the quenched sample. This is probably due to the incomplete substitution of Si in the slow-cooled sample, which may lead to a variation of the chemical composition in the matrix phase. As listed in Table 3.1, the carrier concentration ( $n$ ) of the slow-cooled sample was larger than that of the quenched sample. This difference of  $n$  is presumably due to the variation of the chemical composition of the matrix phase. The carrier mobilities ( $\mu_{\text{H}}$ ) of the slow-cooled and quenched samples were  $63.9 \text{ cm}^2\text{V}^{-1}\text{s}^{-1}$  and  $50.4 \text{ cm}^2\text{V}^{-1}\text{s}^{-1}$ , respectively. The lower  $\mu_{\text{H}}$  value for the quenched sample would be due to the increase of carrier scattering induced by Zn substitution and the grain boundaries.

### 3.1.3.2 Electrical Properties

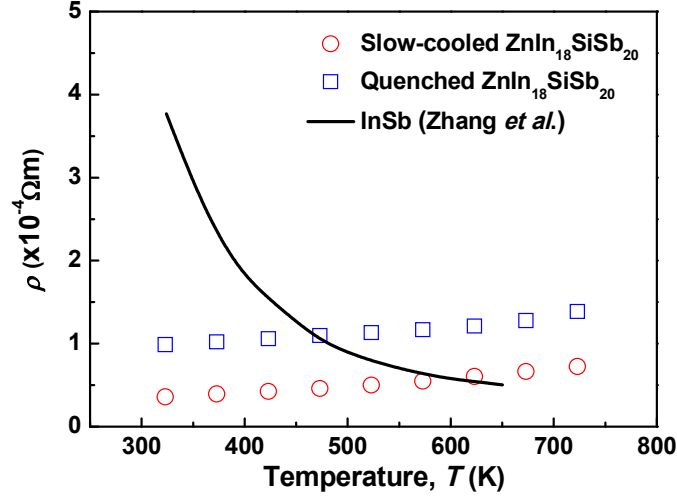


**Figure 3.5** Temperature dependences of the electrical resistivity,  $\rho$  of ZnIn<sub>18</sub>SiSb<sub>20</sub>, together with the data for pure InSb [7].

The temperature dependences of the electrical resistivity ( $\rho$ ) of the ZnIn<sub>18</sub>SiSb<sub>20</sub> samples with different cooling rates, and for InSb as reported by Zhang et al., [7] are shown in Figure 3.5. As shown in Figure 3.5, the  $\rho$  of both samples showed metal-like behavior, unlike InSb, of intrinsic semiconductors. The values for both samples were between  $2 \times 10^{-6}$   $\Omega\text{m}$  and  $2 \times 10^{-5}$   $\Omega\text{m}$ . The  $\rho$  values for the quenched sample were larger than those for the slow-cooled sample due to the low  $\mu_{\text{H}}$  as summarized in Table 3.1.

Figure 3.6 shows Seebeck coefficient ( $S$ ) as a function of temperature for the quenched and slow-cooled ZnIn<sub>18</sub>SiSb<sub>20</sub> samples. The  $S$  values of both samples were positive over the entire temperature range, indicating that the samples were  $p$ -type. The  $S$  values increased with increasing temperature: between  $68 \mu\text{VK}^{-1}$  and  $111 \mu\text{VK}^{-1}$  for the quenched sample and between  $14 \mu\text{VK}^{-1}$  and  $41 \mu\text{VK}^{-1}$  for the slow-cooled sample. The  $S$  values of the quenched sample were larger than those of the slow-cooled sample due to its low  $n$  as summarized in Table 3.1. It is considered that Zn or Si ions would be doped at the In sites in InSb, but the solubility limit of Si in InSb would be quite small. Therefore, we considered that Zn is the dopant in the present study and Zn-doping leads to the difference in carrier

concentration between quenched and slow-cooled samples and thus results in the different transport properties. Moreover, Zn doping of the In site can increase the number of holes and resulted in an alteration to metallic behavior.

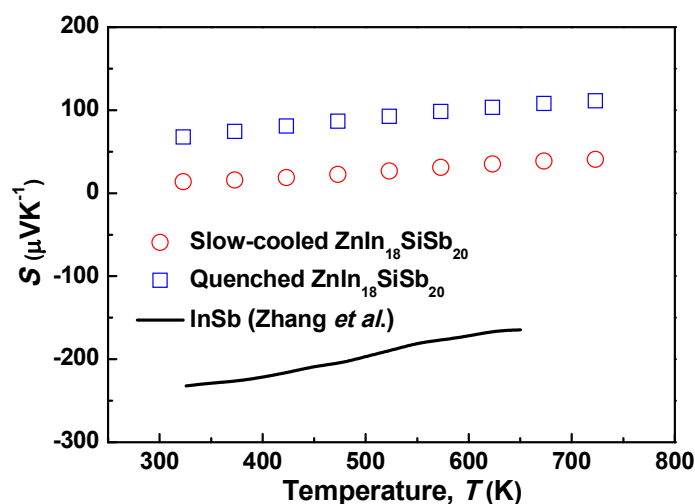


**Figure 3.6** Temperature dependences of Seebeck coefficient,  $S$  of  $\text{ZnIn}_{18}\text{SiSb}_{20}$ , together with the data for pure InSb [7].

The quenched sample also exhibited a larger power factor ( $S^2/\rho$ ) than that of the slow-cooled sample. The maximum value was  $0.91 \times 10^{-3} \text{ Wm}^{-1}\text{K}^{-2}$  at 673 K for the quenched sample, as shown in Figure 3.7.

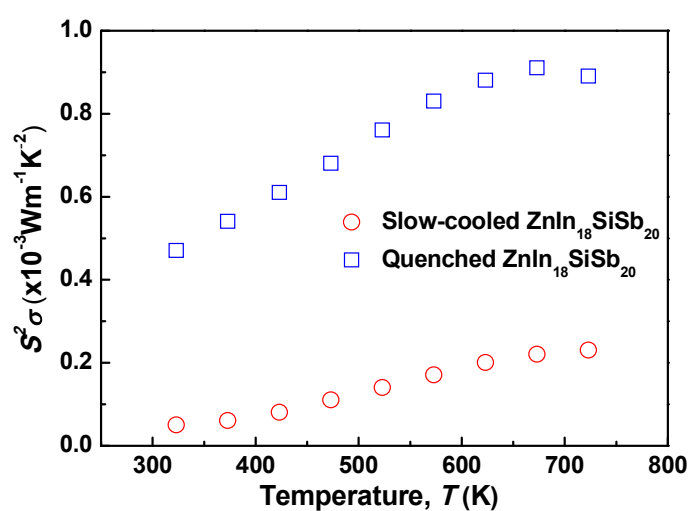


**Figure 3.7** Temperature dependences of power factor,  $S^2\sigma$  ( $\sigma = 1/\rho$ ) of  $\text{ZnIn}_{18}\text{SiSb}_{20}$

### 3.1.3.3 Thermal Conductivity

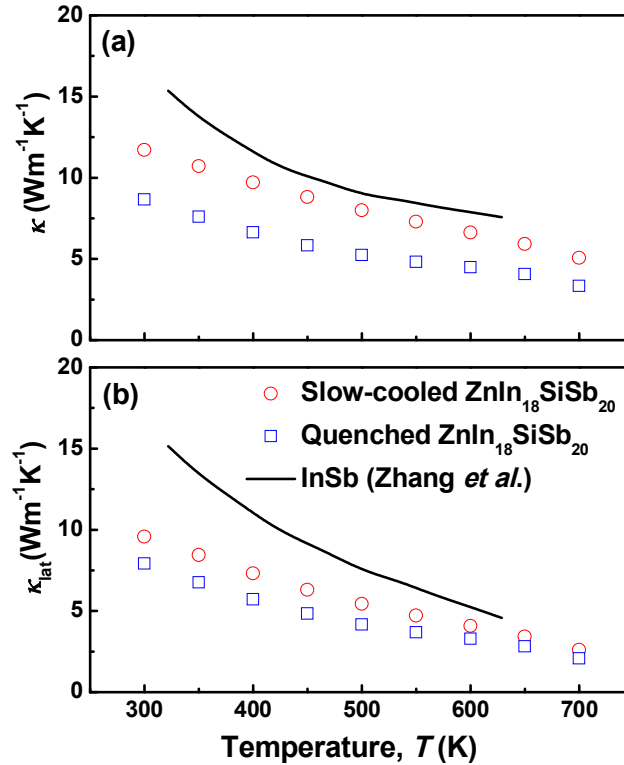


**Figure 3.8** Temperature dependences of the thermal conductivity of ZnIn<sub>18</sub>SiSb<sub>20</sub>, together with the data for pure InSb [7]. (a) total (measured) thermal conductivity,  $\kappa$ , and (b) lattice thermal conductivity,  $\kappa_{\text{lat}}$  ( $= \kappa - LT/\rho$ )

It is well known that the  $\kappa$  of solids is composed mainly of two components:  $\kappa_{\text{lat}}$  and  $\kappa_{\text{el}}$ . We roughly estimated  $\kappa_{\text{el}}$  on the basis of the Wiedemann Franz relationship, using the  $\rho$  data and the Lorenz number ( $L = 2.45 \times 10^{-8} \text{ W}\Omega\text{K}^{-2}$ ), i.e.,  $\kappa_{\text{el}} = LT/\rho$ .  $\kappa_{\text{lat}}$  was obtained by subtracting  $\kappa_{\text{el}}$  from  $\kappa$ . The temperature dependences of  $\kappa$  and  $\kappa_{\text{lat}}$  ( $= \kappa - LT/\rho$ ) for the ZnIn<sub>18</sub>SiSb<sub>20</sub> samples and of  $\kappa_{\text{lat}}$  for InSb are shown in Figure 3.8(a) and 3.8(b), respectively. The  $\kappa$  of the quenched and slow-cooled samples of ZnIn<sub>18</sub>SiSb<sub>20</sub> varied between 8.6 Wm<sup>-1</sup>K<sup>-1</sup> and 3.3 Wm<sup>-1</sup>K<sup>-1</sup> and between 11.2 Wm<sup>-1</sup>K<sup>-1</sup> and 4.9 Wm<sup>-1</sup>K<sup>-1</sup>, respectively, over the measurement temperature range. These decreases in  $\kappa$  with increasing temperature indicate that the phonon contribution is dominant for both samples. The  $\kappa_{\text{lat}}$  values of the quenched and slow-cooled samples were lower than that of  $\kappa_{\text{lat}}$  for InSb due to increasing phonon

scattering by point defects. These results indicate that substitution of Zn into the In site for InSb effectively enhanced phonon scattering.

### 3.1.3.4 Thermoelectric properties

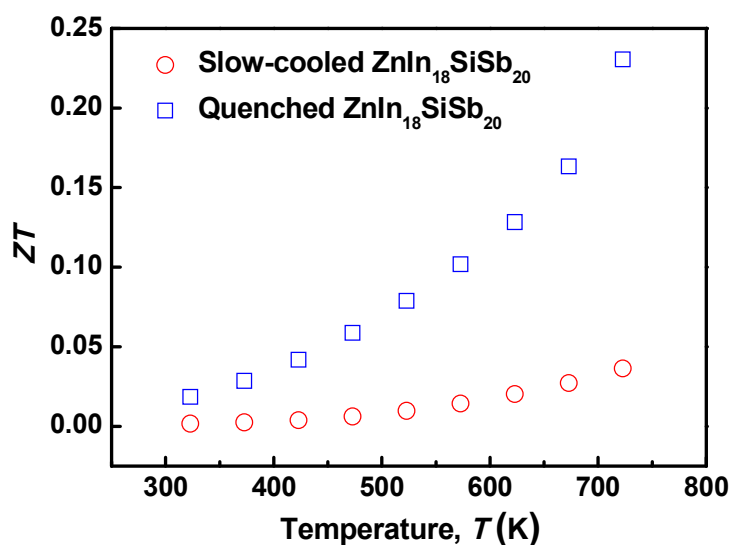


**Figure 3.9** Temperature dependence of  $ZT$  of  $\text{ZnIn}_{18}\text{SiSb}_{20}$ .

Finally, the temperature dependence of the  $ZT$  value of the  $\text{ZnIn}_{18}\text{SiSb}_{20}$  samples is shown in Figure 3.9. The maximum  $ZT$  obtained in the present study was 0.23 at 723 K for the quenched sample.

### 3.1.4 Conclusions

Polycrystalline samples of ZnIn<sub>18</sub>SiSb<sub>20</sub> were prepared by solid-state reaction and hot pressing. The microstructures and TE properties, such as  $\rho$ ,  $S$ , and  $\kappa$ , were investigated for samples subjected to different cooling conditions. The XRD and SEM/EDX results revealed that all samples, regardless of the cooling rate, exhibited zincblende structure. However, the samples showed remarkably different microstructures; i.e., the quenched sample showed smaller grain size than that of the slow-cooled sample, and the slow-cooled sample contained a small amount of Si impurities. These different microstructures affected the carrier concentration and mobility, resulting in differences in not only the electrical properties but also  $\kappa$  for the ZnIn<sub>18</sub>SiSb<sub>20</sub> samples. Both samples showed  $p$ -type conduction and metallic behavior. The slow-cooled sample showed relatively low  $\rho$  values and low absolute  $S$  values owing to its larger grain size and the Zn doping. The  $\kappa$  values of the ZnIn<sub>18</sub>SiSb<sub>20</sub> samples were significantly reduced compared with InSb, presumably due to effective point-defect phonon scattering by the doped Zn that partially displaced In in InSb. The maximum ZT obtained in the present study was 0.23 at 723 K for the quenched sample.



## 3.2 InSb-ZnGeSb<sub>2</sub> System

### 3.2.1 Introduction

Many studies have been made to maximize  $ZT$  value through minimizing the thermal conductivity. For example, the PGEC (phonon glass electron-crystal approach) as in Skutterudites [14] and clathrates [15], where loosely bound atoms rattle in cage structures, and the thin-film multilayer approach, where the introduction of interfaces significantly reduces phonon propagation [16]. The key feature of these systems is the large number of interfaces introduced by the inherent nanofabrication technique that in turn reduce the lattice thermal conductivity. Interestingly, “nanocomposites” in bulks have been recently identified in the  $\text{AgPb}_m\text{SbTe}_{2+m}$  system where compositional fluctuations at the nanoscopic level seem to play a key role for the previously reported high thermoelectric performance [13].

The ball-milling and hot-pressing method has been employed to produce thermoelectric composites since the 1960s [17]. This method can prepare many thermoelectric materials with different chemical compositions and doping levels in a short time. Moreover, Zhou et. al. [18] revealed that a powder metallurgy process combining mechanical alloying and hot-pressing is suitable for fabricating the  $\text{AgPb}_m\text{SbTe}_{2+m}$  bulk materials, which produces fine-grained materials with enhanced  $ZT$  values.

Against this background, in the present chapter, the author prepared Zn/Ge codoped InSb using the ball-milling and hot-pressing method and investigated thermoelectric properties. Compared with the material fabricated by melting slow cooling, the materials prepared by the combined ball-milling and hot pressing methods may be hard to reach an equilibrium state. Therefore, the present work was conducted to study the effect of cooling conditions on the thermoelectric performance.

## 3.2.2 Experimental Procedures

### 3.2.2.1 Sample Preparation

Polycrystalline samples of  $\text{ZnIn}_{18}\text{GeSb}_{20}$  were prepared from powders of InSb (99.999%), Zn (99.99%), Ge (99.99%) and Sb (99.99%) by mechanical alloying (MA). The MA conditions are summarized in Table 3.2. The as-prepared powders were sintered by hot pressing in graphite dies under a pressure of 45 MPa at the temperature of slightly below the melting temperature of InSb for 1.5 h in flowing Ar. The hot-pressed samples were quenched or slowly cooled after annealing at 783K for 72 h.

**Table 3.2** Mechanical alloying conditions.

|                                |              |
|--------------------------------|--------------|
| Weight ratio of ball to powder | 30:1         |
| Type of container and ball     | WC and steel |
| Mill speed                     | 250 rpm      |

### 3.2.2.2 Experimental Details

#### 3.2.2.2.1 X-ray Diffraction Analysis

X-ray diffraction (XRD) measurements were performed on a Rigaku, RINT2000 series X-ray diffractometer using  $\text{Cu-K}\alpha$  radiation at room temperature. The powder X-ray diffraction patterns were taken from 10 to  $120^\circ$ . The lattice parameter, unit cell volume and theoretical density were estimated from the XRD results.

#### 3.2.2.2.2 Electrical Resistivity and Seebeck coefficient

The electrical resistivity ( $\rho$ ) and the Seebeck coefficient ( $S$ ) were performed by using a commercially available apparatus ULVAC, ZEM-1 in a helium atmosphere and over the temperature range of 300 to 723 K.

#### 3.2.2.2.3 Carrier Concentration and Mobility

The Hall effect was measured by the van der Pauw method using a dc Hall effect measurement apparatus Resitest8300 (Toyo Technica) in vacuum at room temperature under an applied magnetic field of 0.5 T.

#### **3.2.2.2.4 Thermal Diffusivity**

The thermal diffusivity was performed by the laser flash method using ULVAC, TC-7000 in vacuum and over the temperature range of 300 to 723 K. The thermal conductivity ( $\kappa$ ) of the specimens was evaluated from the thermal diffusivity ( $\alpha$ ), the heat capacity ( $C_P$ ) and the experimental density ( $d$ ) using the following relationship ( $\kappa = \alpha C_P d$ ).

#### **3.2.2.2.5 Heat Capacity**

The heat capacity ( $C_P$ ) of the sample was estimated from the Dulong-Petit model,  $C_P = 3nR$ , where  $n$  is the number of atoms per formula unit and  $R$  is the gas constant.

#### **3.2.2.2.6 Density**

The densities ( $d$ ) of the samples were calculated on the basis of the measured weight and dimensions. Density is a measure of mass per unit of volume. The unit of density is the kilogram per cubic meter (kg/m<sup>3</sup>). To obtain accurate densities, the measurements were performed several times after careful polishing of all samples.

#### **3.2.2.2.7 Scanning Electron Microscopy**

The Field Emission Scanning Electron Microscopy (FE-SEM) was used to observe microstructures of the samples. The FE-SEM observations were performed on a JEOL, JSM-6500F in vacuum at room temperature.

#### **3.2.2.2.8 Energy Dispersive X-Ray Spectroscopy**

Energy Dispersive X-ray spectroscopy (EDX) is a micro-analytical technique that uses the characteristic spectrum of X-rays emitted by the specimen after excitation by high-energy electrons to obtain information about its elemental composition. The EDX analysis here was performed on a JEOL, JSM-6500F in vacuum at room temperature.

#### **3.2.2.2.9 Dimensionless Figure of Merit**

The dimensionless figure of merit ( $ZT$ ) was calculated by using the above mentioned values of the Seebeck coefficient ( $S$ ), electrical resistivity ( $\rho$ ) and thermal conductivity ( $\kappa$ ), according to the relation ( $ZT = \frac{S^2 T}{\rho \kappa}$ ).

### 3.2.3 Results and Discussion

#### 3.2.3.1 Sample identification

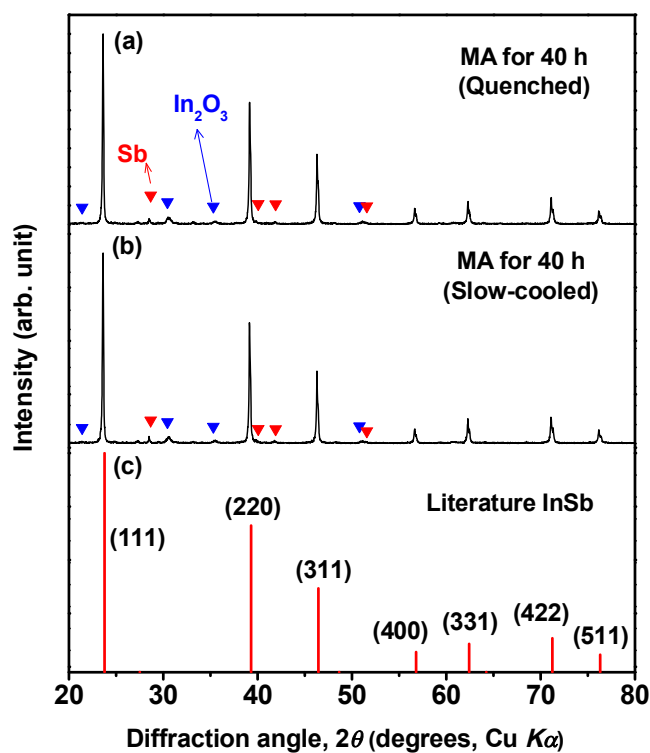


**Figure 3.10** Powder XRD pattern of the polycrystalline samples of  $\text{ZnIn}_{18}\text{GeSb}_{20}$  prepared by MA: (a) quenched after MA for 40 h, (b) slow-cooled after MA for 40 h, and (d) literature data for InSb.

XRD patterns of the ZnIn<sub>18</sub>GeSb<sub>20</sub> samples are shown in Figure 3.10, together with literature data for InSb (JCPDS 06-0208). Figures 3.10(a) and 3.10(b) show the XRD patterns of the samples after quenching and slow cool-down, respectively. These samples were prepared by hot pressing from the MA powders with the ball milling time of 40 h. It was confirmed that MA, with the ball milling for 40 h followed by hot pressing yielded mainly single phase with the zincblende structure but involving a little impurity phase viz., Sb and In<sub>2</sub>O<sub>3</sub>. The intensities of the impurity phases were significantly decreased after 40 h ball milling. It was also confirmed that there were no significant differences between the XRD patterns of the quenched and slow-cooled samples. The chalcopyrite structure could not be identified in all samples.

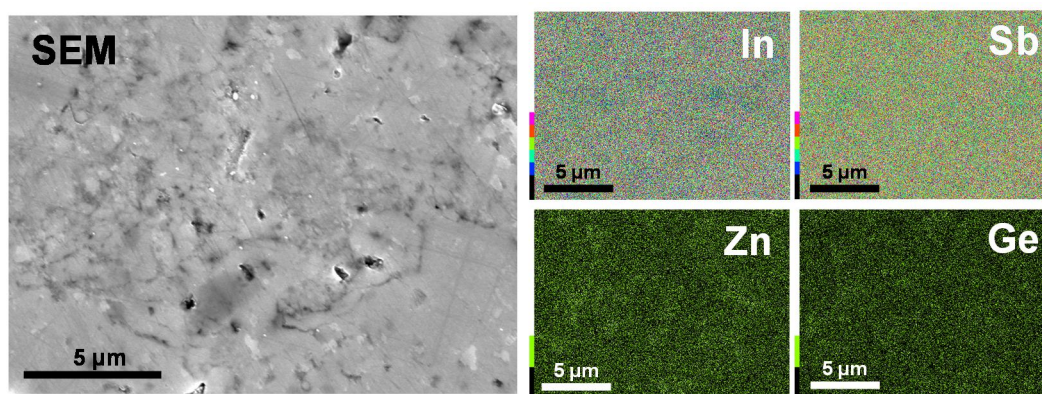


**Figure 3.11** SEM and EDX mapping images of quenched sample of ZnIn<sub>18</sub>GeSb<sub>20</sub> prepared by MA

The SEM and EDX mapping images of the quenched sample after MA for 40 h are shown in Figure 3.11. These images indicate that the quenched sample after hot-pressed sample is homogeneous and Zn, In, Ge, and Sb are uniformly distributed. The quantitative EDX analysis confirmed that the chemical composition of the hot-pressed sample was consistent with stoichiometric composition.

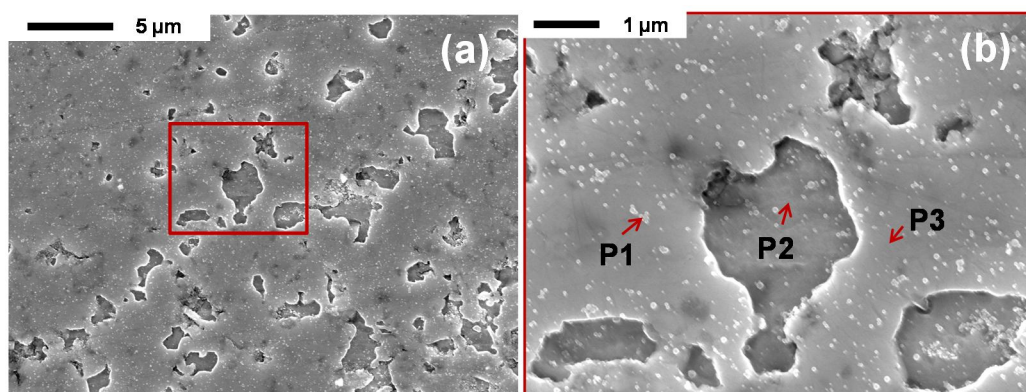


**Figure 3.12** Microstructure of slow-cooled  $\text{ZnIn}_{18}\text{GeSb}_{20}$  prepared by MA: (a) SEM image (b) the high-magnification SEM image of the selected area in (a).

**Table 3.3** Chemical compositions of points P1, P2, and P3 in Figure 3.12, determined from the quantitative EDX analysis.

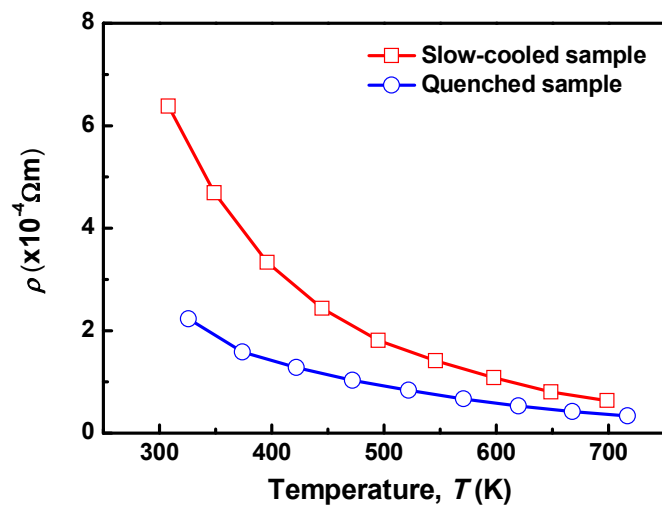
|                     | Chemical composition (at %) |     |      |      |
|---------------------|-----------------------------|-----|------|------|
|                     | Zn                          | Ge  | In   | Sb   |
| Nano InSb (P1)      | 0.7                         | 0.8 | 48.2 | 50.3 |
| Sb-rich region (P2) | 0.9                         | 1.3 | 11.4 | 86.4 |
| Matrix (P3)         | 4.1                         | 2.1 | 40.6 | 53.2 |

Figure 3.12 show the microstructure of slow-cooled sample of  $\text{ZnIn}_{18}\text{GeSb}_{20}$  prepared by MA. In the Figure 3.11 and 3.12(a) indicated that the difference in cooling rate has led to remarkably different microstructures. The quenched sample was more homogeneous than the slow-cooled sample, which was heterogeneous and contained two phases in addition to the matrix phase. These secondary and ternary phases (P1 and P2) and the matrix (P3) region are represented by arrows in the high-magnification SEM image of Figure 3.12(b).

In Figure 3.12(b), the nano-sized particles can be clearly observed. To determine the chemical compositions of these phases, the EDX qualitative analysis was performed. The EDX results shown in Table 3.3 demonstrate that the two secondary phases were the Sb-rich precipitated phase and nano-sized InSb phase (50 ~ 100 nm). Although small peaks for  $\text{In}_2\text{O}_3$  and Sb were observed in the XRD patterns (Figures 3.10(a) and 3.10(b)), such impurity phase were not clearly observed from the SEM and EDX analysis. As described before, the present

study is based on the concept of the LAST compound system, in which the nano-sized AgSb inclusions are embedded in PbTe matrix. However, in the present study, the ZnGeSb<sub>2</sub> inclusions of chalcopyrite structure were not identified in the InSb matrix, but nano-sized InSb precipitates with the size of 50 ~ 100 nm were observed.

### 3.2.3.2 Electrical Properties



**Figure 3.13** Temperature dependence of the electrical resistivity,  $\rho$  of ZnIn<sub>18</sub>GeSb<sub>20</sub> prepared by MA.

The temperature dependences of the electrical properties of the ZnIn<sub>18</sub>GeSb<sub>20</sub> samples prepared by MA for 40 h are shown in Figure 3.13. As seen in Figure 3.13, the  $\rho$  values of both samples were in the order of  $10^4$   $\Omega\text{m}$  around room temperature and decreased with increasing temperature. It has been reported that the  $\mu$  values of bulk InSb are  $3.1 \times 10^5$   $\Omega\text{m}$  at 326 K to  $5.5 \times 10^6$   $\Omega\text{m}$  at 567 K [19]. The  $\rho$  values of the ZnIn<sub>18</sub>GeSb<sub>20</sub> samples are larger than that of bulk InSb, presumably due to an influence of remnant Sb and In<sub>2</sub>O<sub>3</sub> phases as observed in the XRD patterns (Figure 3.10). The  $\rho$  values of the quenched sample were slightly lower than those of the slow-cooled sample, presumably owing to the high homogeneity of the quenched sample and boundary scattering of electrons by the secondary phase in the slow-cooled sample.

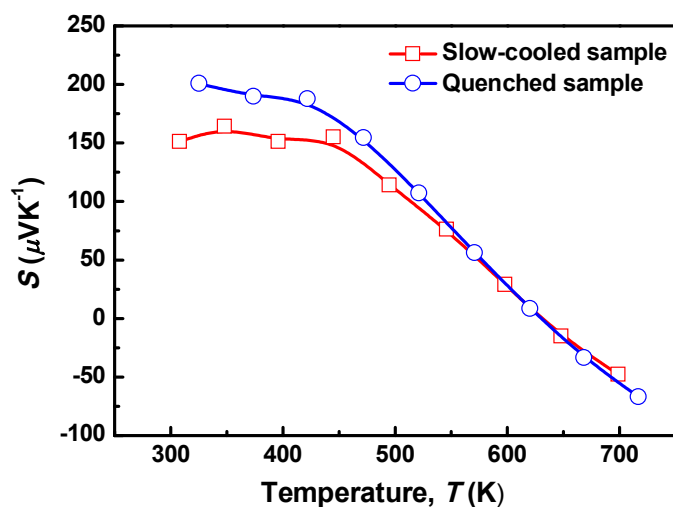


**Figure 3.14** Temperature dependence of Seebeck coefficient,  $S$  of  $\text{ZnIn}_{18}\text{GeSb}_{20}$  prepared by MA.

Figure 3.14 shows the  $S$  as a function of temperature for the  $\text{ZnIn}_{18}\text{GeSb}_{20}$  samples. Positive  $S$  values mean  $p$ -type electrical transport properties, but the  $S$  values of all the samples decreased gradually, becoming negative at high temperatures. This indicates that the carriers were governed by a mixed conduction mechanism at high temperatures. The room-temperature  $S$  values obtained for the quenched and slow-cooled samples were  $201 \mu\text{V}$  and  $164 \mu\text{V}$ , respectively. The Sb-rich secondary phase existed in the slow-cooled sample might be metallic with small Seebeck coefficient, leading to the smaller Seebeck coefficient of the slow-cooled sample than that of the quenched sample.

### 3.2.3.3 Thermal Conductivity

It is well known that the  $\kappa$  of solids is composed mainly of two components:  $\kappa_{\text{lat}}$  and  $\kappa_{\text{el}}$ . We roughly estimated  $\kappa_{\text{el}}$  on the basis of the Wiedemann Franz relation, using the  $\sigma$  data and the Lorenz number ( $L = 2.45 \times 10^8 \text{ W}\Omega\text{K}^{-2}$ ), i.e.,  $\kappa_{\text{el}} = L\sigma T$ , and  $\kappa_{\text{lat}}$  was obtained by subtracting  $\kappa_{\text{el}}$  from  $\kappa$ .

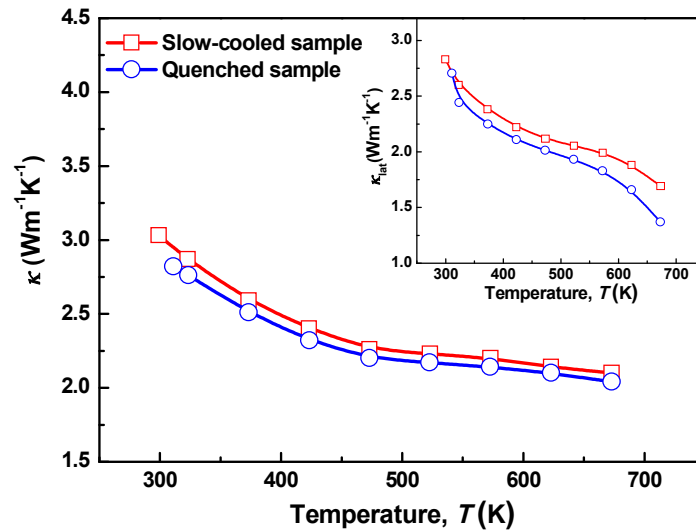


**Figure 3.15** Temperature dependences of the total (measured) conductivities,  $\kappa$ , and lattice thermal conductivity,  $\kappa_{\text{lat}}$  (insert diagram) of  $\text{ZnIn}_{18}\text{GeSb}_{20}$  prepared by MA:  $\kappa_{\text{lat}} (= \kappa - L\sigma T)$ , where  $L$  is the Lorentz number ( $= 2.45 \times 10^8 \text{ W}\Omega\text{K}^{-2}$ ),  $\sigma$  is the electrical conductivity ( $= 1/\rho$ ), and  $T$  is the absolute temperature.

The temperature dependences of the  $\kappa$  and  $\kappa_{\text{lat}} (= \kappa - L\sigma T)$  values of the polycrystalline samples of  $\text{ZnIn}_{18}\text{GeSb}_{20}$  prepared by MA for 40 h are shown in Figure 3.15. The  $\kappa$  of the quenched and slow-cooled samples varied between  $2.04 \text{ Wm}^{-1}\text{K}^{-1}$  and  $2.82 \text{ Wm}^{-1}\text{K}^{-1}$  and between  $2.10 \text{ Wm}^{-1}\text{K}^{-1}$  and  $3.03 \text{ Wm}^{-1}\text{K}^{-1}$ , respectively, over the measured temperature range. These values are much lower than those reported for bulk InSb: 11 to  $18 \text{ Wm}^{-1}\text{K}^{-1}$  [3]. These low  $\kappa$  values are presumably attributable to grain refinement through MA and to alloy scattering from the multi-component system. Unfortunately, both samples exhibited low densities, i.e., about 86% of the theoretical density. The pores in the sintered samples are also attributable to the reduction of the  $\kappa$ . The  $\kappa$  of the quenched sample was lower than that of the slow-cooled sample. As indicated above,  $\kappa_{\text{lat}} = \kappa - \kappa_{\text{el}}$ . The  $\kappa_{\text{el}}$  value of quenched sample is higher because of the lower  $\mu$ . Thus, the decrease of  $\kappa$  can be attributed to the significant reduction of the  $\kappa_{\text{lat}}$  caused by the partial substitution of In by Zn and Ge. Moreover, the  $\kappa_{\text{lat}}$  of the slow-cooled sample was higher than that of the quenched sample, which was probably due to the Sb-rich region of the secondary phase with its large  $\kappa_{\text{lat}}$ . The present study confirmed that a nano-sized InSb phase was formed in the slow-cooled sample.

Although this phase was dispersed uniformly across the slow-cooled sample, the Sb-rich region, which has a high  $\kappa$ , was the dominating factor in the large  $\kappa_{\text{lat}}$ .

### 3.2.3.4 Thermoelectric Properties

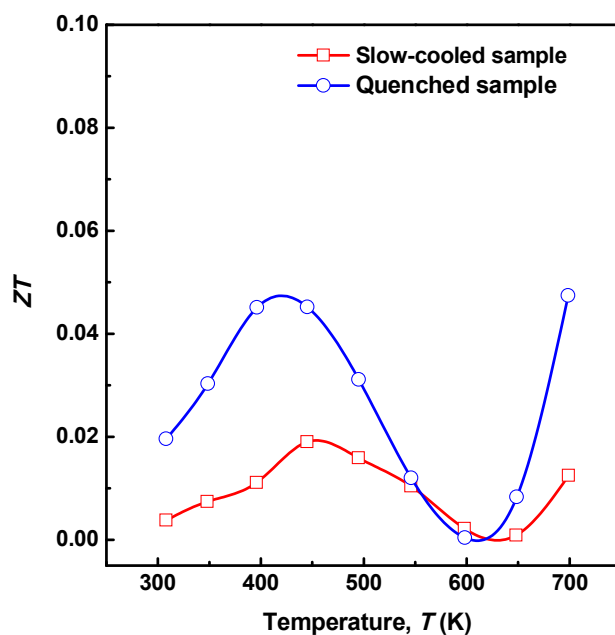


**Figure 3.16** Temperature dependences of  $ZT$  of  $\text{ZnIn}_{18}\text{GeSb}_{20}$ , samples prepared by MA.

Finally, the temperature dependence of the  $ZT$  of the polycrystalline samples of  $\text{ZnIn}_{18}\text{GeSb}_{20}$  is shown in Figure 3.16. The maximum  $ZT$  obtained in the present study was 0.05 at around 700 K for the quenched sample. Although the  $ZT$  values of the solid solution are lower than those of InSb, all samples showed a roughly 60% reduction in  $\kappa$  as compared to that of bulk InSb. This means that there is further room for improvement in  $ZT$  through optimization of the carrier concentration and annealing procedure.

### 3.2.4 Conclusions

Polycrystalline samples of ZnIn<sub>18</sub>GeSb<sub>20</sub> were prepared by MA and hot pressing. The microstructure and TE properties, such as  $\rho$ ,  $S$  and  $\kappa$ , were investigated in samples cooled at different rates after annealing. The XRD and SEM/EDX results revealed that all samples, regardless of the cooling rate, exhibited an almost single phase with the zincblende structure, but each sample showed a remarkably different microstructure. The quenched sample was homogeneous, while the slow-cooled sample was composed of a matrix phase and a Sb-rich, nano-sized InSb phase. The slow-cooled sample showed relatively large  $\rho$  values and low absolute  $S$  values, owing to the presence of the Sb-rich secondary phase. The  $\kappa$  value of the ZnIn<sub>18</sub>GeSb<sub>20</sub> sample was significantly reduced compared to that of InSb, presumably due to grain refinement through MA and effective point-defect phonon scattering by the bivalent Zn and tetravalent Ge ions that partially replaced the trivalent In ions. In the LAST system, Ag-Sb nano-inclusions formed in the PbTe matrix play an important role to decrease the  $\kappa$ . However, in the present case, Zn-Ge nano-inclusions were not formed in the InSb matrix. Hence, the secondary phase observed in the samples should play an important role to decrease the  $\kappa$ . The maximum  $ZT$  obtained in the present study was 0.05 at around 700K for the quenched sample.



## 3.3 InSb-ZnSnSb<sub>2</sub> and InSb-ZnPbSb<sub>2</sub> System

### 3.3.1 Introduction

In the previous chapter, the author has been investigated the thermoelectric properties (TE) of isoelectric and isostructural solid solutions, e.g., 18InSb-ZnSiSb<sub>2</sub> and 18InSb-ZnGeSb<sub>2</sub>. The thermal conductivity,  $\kappa$  values of these solid solutions were reduced compared with InSb due to effective point-defect phonon scattering by the partial substitution of In in InSb. Since Si, Ge, Sn and Pb are in the same column in the periodic table, InSb-ZnSnSb<sub>2</sub> and InSb-ZnPbSb<sub>2</sub> can be also expected to show lower  $\kappa$  due isoelectric and isostructrueal solid solutions. Moreover, as Pb has the largest mass difference with In, Zn/Pb codoping in In site can be expected to reduce  $\kappa$  due to the mass fluctuation effect.

The alloying scattering approach has already achieved significant increase in  $ZT$  for both SiGe [20] and the half-Heusler compounds [21-23]. It has been clearly demonstrated that the atomic mass difference between the guest and host plays the key role on the reduction in the lattice thermal conductivity ( $\kappa_{\text{lat}}$ ), and the scattering parameter ( $A$ ) can be written as the following expression: [24]

$$A = \frac{\Omega_0}{4\pi v^2} x(1-x) \left(\frac{\Delta M}{M}\right)^2$$

Here,  $\Omega_0$ ,  $v$ ,  $x$ ,  $\Delta M$ , and  $M$  stand for the volume of the unit cell, the lattice sound velocity, the fraction of the guest atom, the atomic mass difference between the guest and host, and the average mass of the cell, respectively. Based on this equation, a larger the mass difference between the guest and host atom will produce a more effective scattering of phonons by the mass fluctuation effect. Thus, increase of phonon scattering can achieve more reduction in  $\kappa_{\text{lat}}$ .

Against this background, the present study investigates the high-temperature TE properties of ZnIn<sub>18</sub>SnSb<sub>20</sub> and ZnIn<sub>18</sub>PbSb<sub>20</sub> compounds by codoping Zn<sup>2+</sup> and Sn<sup>4+</sup> or Pb<sup>4+</sup> ions into In<sup>3+</sup> sites of InSb.

### 3.3.2 Experimental Procedures

#### 3.3.2.1 Sample Preparation

The synthesis of the polycrystalline samples of  $\text{ZnIn}_{18}\text{SnSb}_{20}$  and  $\text{ZnIn}_{18}\text{PbSb}_{20}$  prepared from the starting materials was chunks of InSb (99.999 %), Zn (99.99 %), Sn and Pb (> 99.99 %), and Sb (99.99 %). The starting materials were weighed out in a stoichiometric ratio and loaded into the silica tubes which were covered by carbon sheet. The silica tube was sealed under vacuum and transferred into a programmable furnace. The silica tube was heated to 1273 K at 5 K/min and kept for 12 h, and annealed at 783 K for 3 days to correct crystallographic phase. The completely reacted solid was removed from the silica tube and cleaned to remove small amounts of carbon from the surface. The obtained ingots of  $\text{ZnIn}_{18}\text{SnSb}_{20}$  and  $\text{ZnIn}_{18}\text{PbSb}_{20}$  were crushed into fine powders. The as-prepared powders of  $\text{ZnIn}_{18}\text{SnSb}_{20}$  and  $\text{ZnIn}_{18}\text{PbSb}_{20}$  were sintered by hot pressing in graphite dies under pressure of 45 MPa at a temperature slightly below the melting temperature of InSb for 1.5 h under flowing Ar. The hot-pressed samples were quenched or slowly cooled after annealing at 783 K for 72 h. The bulk samples were cleaned the surface for measuring the weight and dimensions.

#### 3.3.2.2 Experimental Details

##### 3.3.2.2.1 X-ray Diffraction Analysis

X-ray diffraction (XRD) measurements were performed on a Rigaku, RINT2000 series X-ray diffractometer using  $\text{Cu-K}\alpha$  radiation at room temperature. The powder X-ray diffraction patterns were taken from 10 to  $120^\circ$ . The lattice parameter, unit cell volume and theoretical density were estimated from the XRD results.

##### 3.3.2.2.2 Electrical Resistivity and Seebeck coefficient

The electrical resistivity ( $\rho$ ) and the Seebeck coefficient ( $S$ ) were performed by using a commercially available apparatus ULVAC, ZEM-1 in a helium atmosphere and over the temperature range of 300 to 723 K.

##### 3.3.2.2.3 Carrier Concentration and Mobility

The Hall effect was measured by the van der Pauw method using a dc Hall effect measurement apparatus Resitest8300 (Toyo Technica) in vacuum at room temperature under an applied magnetic field of 0.5 T.

#### **3.3.2.2.4 Thermal Diffusivity**

The thermal diffusivity was performed by the laser flash method using ULVAC, TC-7000 in vacuum and over the temperature range of 300 to 723 K. The thermal conductivity ( $\kappa$ ) of the specimens was evaluated from the thermal diffusivity ( $\alpha$ ), the heat capacity ( $C_P$ ) and the experimental density ( $d$ ) using the following relationship ( $\kappa = \alpha C_P d$ ).

#### **3.3.2.2.5 Heat Capacity**

The heat capacity ( $C_P$ ) of the sample was estimated from the Dulong-Petit model,  $C_P = 3nR$ , where  $n$  is the number of atoms per formula unit and  $R$  is the gas constant.

#### **3.3.2.2.6 Density**

The densities ( $d$ ) of the samples were calculated on the basis of the measured weight and dimensions. Density is a measure of mass per unit of volume. The unit of density is the kilogram per cubic meter (kg/m<sup>3</sup>). To obtain accurate densities, the measurements were performed several times after careful polishing of all samples.

#### **3.3.2.2.7 Scanning Electron Microscopy**

The Field Emission Scanning Electron Microscopy (FE-SEM) was used to observe microstructures of the samples. The FE-SEM observations were performed on a JEOL, JSM-6500F in vacuum at room temperature.

#### **3.3.2.2.8 Energy Dispersive X-Ray Spectroscopy**

Energy Dispersive X-ray spectroscopy (EDX) is a micro-analytical technique that uses the characteristic spectrum of X-rays emitted by the specimen after excitation by high-energy electrons to obtain information about its elemental composition. The EDX analysis here was performed on a JEOL, JSM-6500F in vacuum at room temperature.

### 3.3.2.2.9 Dimensionless Figure of Merit

The dimensionless figure of merit ( $ZT$ ) was calculated by using the above mentioned values of the Seebeck coefficient ( $S$ ), electrical resistivity ( $\rho$ ) and thermal conductivity ( $\kappa$ ), according to the relation ( $ZT = \frac{S^2 T}{\rho \kappa}$ ).

## 3.3.3 Results and Discussion

### 3.3.3.1 Sample identification

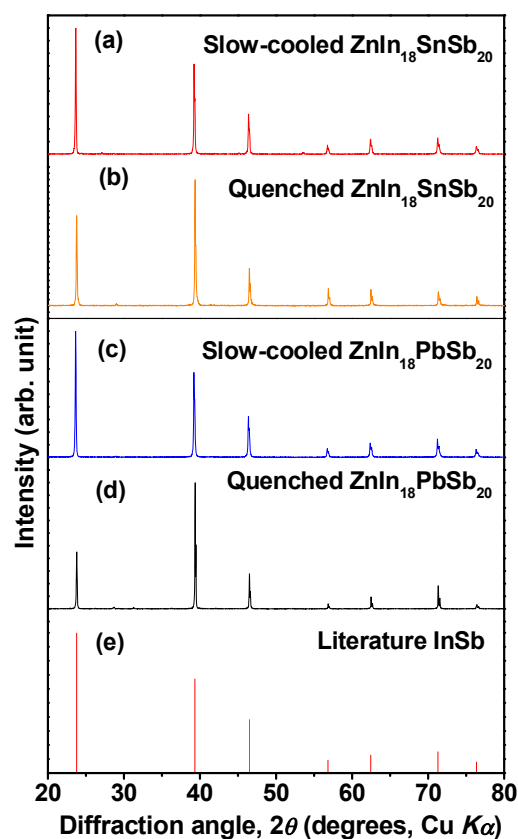


**Figure.3.17** XRD pattern of the  $\text{ZnIn}_{18}\text{SnSb}_{20}$  and  $\text{ZnIn}_{18}\text{PbSb}_{20}$  samples: (a, c) slow-cooled sample, and (b, d) quenched sample, together with the peak positions of literature  $\text{InSb}$ .

The XRD patterns of the polycrystalline samples of  $\text{ZnIn}_{18}\text{SnSb}_{20}$  and  $\text{ZnIn}_{18}\text{PbSb}_{20}$  with different cooling conditions, slow-cooled and quenched are shown in Figure 3.17. The XRD patterns of the prepared samples together with the peak positions of literature  $\text{InSb}$ . Almost all the peaks of the samples were indexed in terms of the zincblende structure with

the space group  $F-43m$ . The lattice parameters, sample bulk densities of the samples are summarized in Table 3.4. The hot-pressed ZnIn<sub>18</sub>SnSb<sub>20</sub> samples had lower bulk density than those of ZnIn<sub>18</sub>PbSb<sub>20</sub> samples, which is approximately 88 % and 95 % of the theoretical density, respectively.

**Table 3.4** Lattice parameters and sample bulk densities of ZnIn<sub>18</sub>SnSb<sub>20</sub> and ZnIn<sub>18</sub>PbSb<sub>20</sub> with different cooling conditions.

|  | Sample name                           |                                       |                                       |                                       |
|--|---------------------------------------|---------------------------------------|---------------------------------------|---------------------------------------|
|  | Quenched                              | Slow-cooled                           | Quenched                              | Slow-cooled                           |
|  | ZnIn <sub>18</sub> SnSb <sub>20</sub> | ZnIn <sub>18</sub> SnSb <sub>20</sub> | ZnIn <sub>18</sub> PbSb <sub>20</sub> | ZnIn <sub>18</sub> PbSb <sub>20</sub> |
| Lattice parameter, $a$ (nm)                        | 0.6475                                | 0.6475                                | 0.6474                                | 0.6474                                |
| Theoretical density, $d_{th}$ (gcm <sup>-3</sup> ) | 5.73                                  | 5.73                                  | 5.84                                  | 5.84                                  |
| Measured density, $d_{exp}$ (gcm <sup>-3</sup> )   | 4.88                                  | 5.07                                  | 5.55                                  | 5.49                                  |
| Relative density (%)                               | 85                                    | 88                                    | 95                                    | 94                                    |

### 3.3.3.2 Electrical Properties

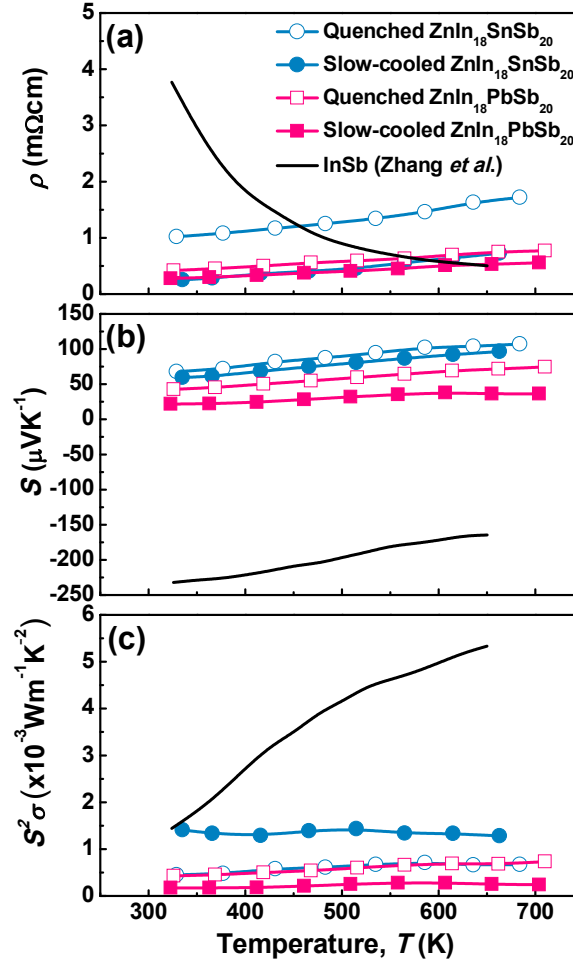


**Figure 3.18** Temperature dependences of the electrical properties of  $\text{ZnIn}_{18}\text{SnSb}_{20}$  and  $\text{ZnIn}_{18}\text{PbSb}_{20}$ , together with the data for pure InSb [7]. (a) electrical resistivity,  $\rho$ ; (b) Seebeck coefficient,  $S$ , and (c) power factor,  $S^2\sigma$  ( $\sigma = 1/\rho$ ).

The temperature dependences of the electrical resistivity ( $\rho$ ), Seebeck coefficient ( $S$ ), and power factor ( $\text{PF} = S^2/\rho$ ) of the samples of  $\text{ZnIn}_{18}\text{SnSb}_{20}$  and  $\text{ZnIn}_{18}\text{PbSb}_{20}$  with different cooling conditions, and for InSb as reported by Zhang *et al.*, [7] are summarized in Figure 3.18. As shown in Figure 3.18(a), the  $\rho$  of all samples slightly increased with increasing temperature, indicating metallic behavior unlike InSb of intrinsic semiconductors. The values for all samples were in the order of  $10^{-5} \Omega \text{ m}$ . As shown in Figure 3.18(b), the  $S$  values of the samples were positive over the entire temperature range, indicating that the majority of the

carriers were holes. The  $S$  values of the ZnIn<sub>18</sub>SnSb<sub>20</sub> samples were larger than those of the ZnIn<sub>18</sub>PbSb<sub>20</sub> samples. In general, since the large carrier concentration ( $n$ ) leads to the low  $\rho$  and the lower absolute  $S$ , ZnIn<sub>18</sub>PbSb<sub>20</sub> would have the larger  $n$  values than that of ZnIn<sub>18</sub>SnSb<sub>20</sub>.

### 3.3.3.3 Thermal Conductivity

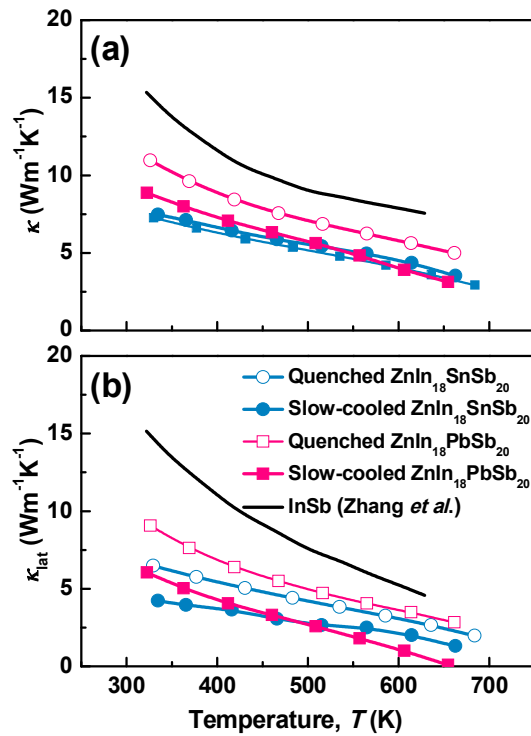


**Figure 3.19** Temperature dependences of the thermal conductivity of ZnIn<sub>18</sub>SnSb<sub>20</sub> and ZnIn<sub>18</sub>PbSb<sub>20</sub>, together with the data for pure InSb [7]. (a) total (measured) thermal conductivity,  $\kappa$ , and (b) lattice thermal conductivity,  $\kappa_{\text{lat}}$  ( $= \kappa - LT/\rho$ ).

The  $\kappa$  as a function of temperature data are shown in Figure 3.19. The  $\kappa$  decreased with increasing temperature indicate that the phonon contribution is dominant for all samples. Within the measured temperature range, the lowest  $\kappa$  is obtained for the quenched ZnIn<sub>18</sub>SnSb<sub>20</sub> sample which reaches 7.73 Wm<sup>-1</sup>K<sup>-1</sup> at 330 K and 2.93 Wm<sup>-1</sup>K<sup>-1</sup> at 684 K. The  $\kappa_{\text{lat}}$  was roughly estimated by subtracting  $\kappa_{\text{el}}$  ( $= LT/\rho$  where  $L$  is the Lorenz number  $L = 2.45$

$\times 10^{-8} \text{W}\Omega\text{K}^{-2}$ ) from the measured  $\kappa$ , i.e.  $\kappa_{\text{lat}} = \kappa - LT/\rho$ . The  $\kappa_{\text{lat}}$  values of the  $\text{ZnIn}_{18}\text{SnSb}_{20}$  and  $\text{ZnIn}_{18}\text{PbSb}_{20}$  samples were lower than that of  $\kappa_{\text{lat}}$  for InSb due to increasing phonon scattering by point defects.

### 3.3.3.4 Thermoelectric Properties

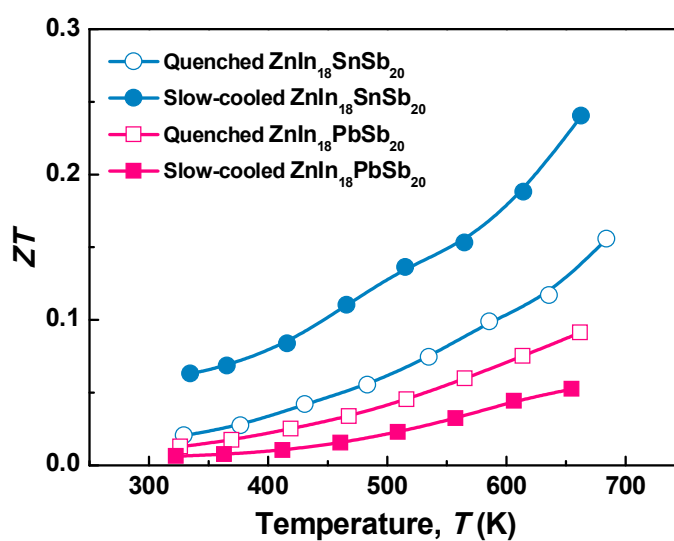


**Figure 3.20** Temperature dependences of  $ZT$  of  $\text{ZnIn}_{18}\text{SnSb}_{20}$  and  $\text{ZnIn}_{18}\text{PbSb}_{20}$ .

Finally, the temperature dependence of the  $ZT$  value of the  $\text{ZnIn}_{18}\text{SnSb}_{20}$  and  $\text{ZnIn}_{18}\text{PbSb}_{20}$  samples is shown in Figure 3.20. The maximum  $ZT$  obtained in the present study was 0.24 at 660 K for the slow-cooled  $\text{ZnIn}_{18}\text{SnSb}_{20}$  sample.

### 3.3.4 Conclusions

To investigate the effect of the codoping Zn/Sn and Zn/Pb on TE properties of InSb, the samples of ZnIn<sub>18</sub>SnSb<sub>20</sub> and ZnIn<sub>18</sub>PbSb<sub>20</sub> were prepared and investigated the high-temperature thermoelectric properties. The polycrystalline samples of ZnIn<sub>18</sub>SnSb<sub>20</sub> and ZnIn<sub>18</sub>PbSb<sub>20</sub> were prepared by solid-state reaction and hot-pressing. The TE properties, such as  $\rho$ ,  $S$ , and  $\kappa$ , were investigated for samples subjected to different cooling conditions. The values  $\rho$  for all samples were in the order of  $10^{-5}$   $\Omega$  m. All samples exhibited positive  $S$  values. The  $S$  values of the ZnIn<sub>18</sub>SnSb<sub>20</sub> samples were larger than those of the ZnIn<sub>18</sub>PbSb<sub>20</sub> samples, indicating that Zn/Pb codoping for InSb lead to the larger  $n$  than Zn/Sn codoping. The  $\kappa$  values of the ZnIn<sub>18</sub>SnSb<sub>20</sub> and ZnIn<sub>18</sub>PbSb<sub>20</sub> samples were significantly reduced compared with InSb, presumably due to effective point-defect phonon scattering by the codoped Zn/Sn and Zn/Pb ions that partially displaced In in InSb. The maximum  $ZT$  obtained in the present study was 0.24 at 660 K for the slow-cooled sample.



## 3.4 InSb-In<sub>2</sub>XTe (X = Si, Ge, or, Sn) System

### 3.4.1 Introduction

As has been shown by Goodman [25], it is possible to predict new semiconducting materials with zincblende or the associated chalcopyrite structure by process of cross-substitution. Effectively this keeps the ratio of valence electron to lattice sites equal to four. Thus the binary compounds such as GaAs, InSb, etc., may be considered as being cross-substitution products of group IV elements. One limitation on the production of new materials by this method is the stability of the resulting compounds. Thus, for the heavier compounds, e.g., InSb, the derived ternary compounds are unstable and so are not formed. However, it is possible in this case to carry out the process to a limited extent, i.e. in the case InSb to replace only some of the In atoms by combinations of Cd and Sn atoms. The resulting materials can be looked upon as alloys between the A<sup>III</sup>B<sup>V</sup> compound and the derived ternary compound, e.g., InSb-CdSnSb<sub>2</sub> [26]. In the previous chapter, the author prepared the samples of InSb-ZnXSb<sub>2</sub> (X = Si, Ge, Sn, or Pb) using this method of cross-substitution and investigated the thermoelectric properties at high temperature.

In the present chapter, in view of the possibility of cross-substitution in the anionic sub-lattice, an attempt was made to prepare some III<sub>2</sub>-IV-V anti-chalcopyrite compounds as shown Figure 3.21. Wooley and Williams [26] have demonstrated that In<sub>2</sub>GeTe, In<sub>2</sub>SnTe, and In<sub>2</sub>SnSe can crystallize in the zincblende (sphalerite) structure when they form solid solutions with InSb. Thus, we prepared various alloys of InSb in which Sb is replaced by (Si, Te), (Ge, Te) and (Sn, Te) and investigated the thermoelectric properties at high temperature.

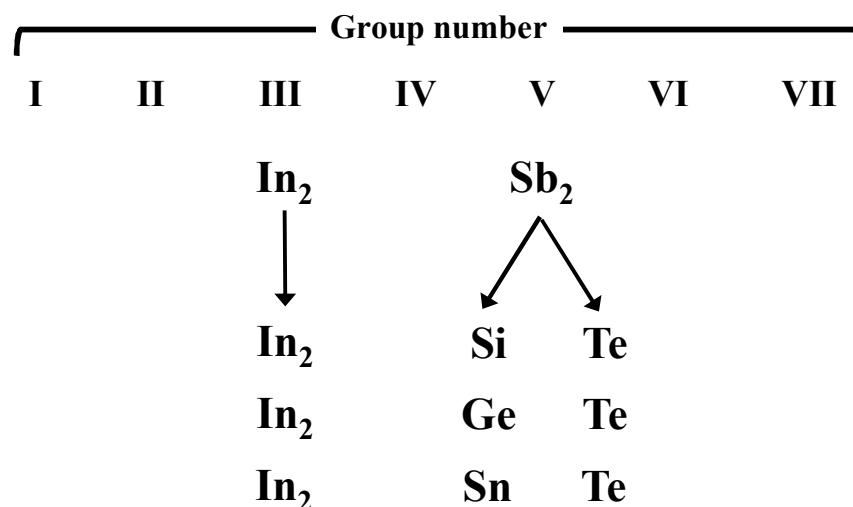


**Figure 3.21** Schematic illustration of the formation of III<sub>2</sub>-V-VI anti-chalcopyrite compounds.

## 3.4.2 Experimental Procedures

### 3.4.2.1 Sample Preparation

The synthesis of the polycrystalline samples of InSb-10 mole % In<sub>2</sub>XTe ( $X = \text{Si, Ge, or Sn}$ ) prepared from the starting materials was chunks of InSb (99.999 %), Te (99.999 %), Si, Ge, and Sn (> 99.99 %). The starting materials were weighed out in a stoichiometric ratio and loaded into the silica tubes which were covered by carbon sheet. The silica tube was sealed under vacuum and transferred into a programmable furnace. The silica tube was heated to 1273 K at 5 K/min and kept for 12 h. The silica tube containing the homogeneous molten liquid was quenched into a water bath and annealed at 673 K for 14 days to correct crystallographic phase. The completely reacted solid was removed from the silica tube and cleaned to remove small amounts of carbon from the surface. The obtained ingots of InSb-10 mole % In<sub>2</sub>XTe ( $X = \text{Si, Ge, or Sn}$ ) were crushed into fine powders. The as-prepared powders of InSb-10 mole % In<sub>2</sub>XTe ( $X = \text{Si, Ge, or Sn}$ ) were sintered by hot pressing in graphite dies under pressure of 45 MPa at a temperature slightly below the melting temperature of InSb for 1.5 h under flowing Ar. The bulk samples were cleaned the surface for measuring the weight and dimensions.

### 3.4.2.2 Experimental Details

#### 3.4.2.2.1 X-ray Diffraction Analysis

X-ray diffraction (XRD) measurements were performed on a Rigaku, RINT2000 series X-ray diffractometer using Cu-K $\alpha$  radiation at room temperature. The powder X-ray diffraction patterns were taken from 10 to 120°. The lattice parameter, unit cell volume and theoretical density were estimated from the XRD results.

#### 3.4.2.2.2 Electrical Resistivity and Seebeck coefficient

The electrical resistivity ( $\rho$ ) and the Seebeck coefficient ( $S$ ) were performed by using a commercially available apparatus ULVAC, ZEM-1 in a helium atmosphere and over the temperature range of 300 to 673 K.

#### 3.4.2.2.3 Thermal Diffusivity

The thermal diffusivity was performed by the laser flash method using ULVAC, TC-7000 in vacuum and over the temperature range of 300 to 673 K. The thermal conductivity ( $\kappa$ ) of the specimens was evaluated from the thermal diffusivity ( $\alpha$ ), the heat capacity ( $C_P$ ) and the experimental density ( $d$ ) using the following relationship ( $\kappa = \alpha C_P d$ ).

#### 3.4.2.2.4 Heat Capacity

The heat capacity ( $C_P$ ) of the sample was estimated from the Dulong-Petit model,  $C_P = 3nR$ , where  $n$  is the number of atom per formula unit and  $R$  is the gas constant.

#### 3.4.2.2.5 Density

The densities ( $d$ ) of the samples were calculated on the basis of the measured weight and dimensions. Density is a measure of mass per unit of volume. The unit of density is the kilogram per cubic meter (kg/m<sup>3</sup>). To obtain accurate densities, the measurements were performed several times after careful polishing of all samples.

#### 3.4.2.2.6 Dimensionless Figure of Merit

The dimensionless figure of merit ( $ZT$ ) was calculated by using the above mentioned values of the Seebeck coefficient ( $S$ ), electrical resistivity ( $\rho$ ) and thermal conductivity ( $\kappa$ ), according to the relation ( $ZT = \frac{S^2 T}{\rho \kappa}$ ).

### 3.4.3 Results and Discussion

#### 3.4.3.1 Sample identification

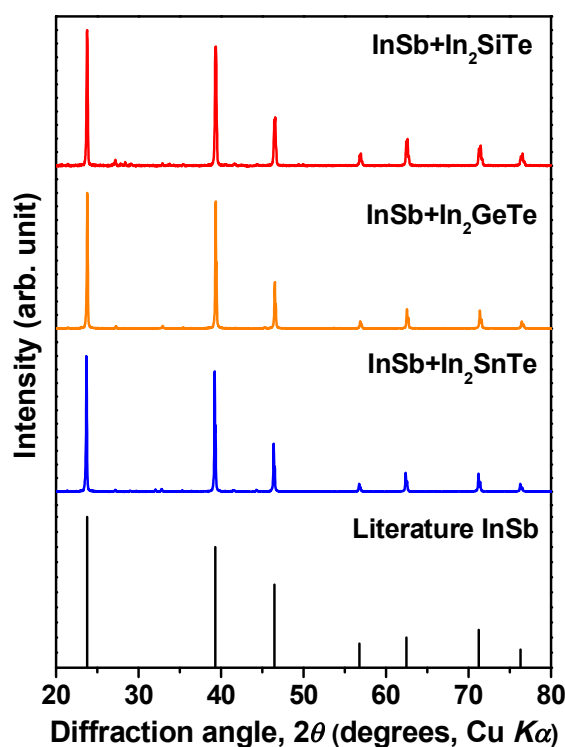


**Figure 3.22** Powder XRD pattern of the InSb-10 mole %  $\text{In}_2\text{XTe}$  ( $X = \text{Si}, \text{Ge}, \text{or Sn}$ ), together with the peak positions of literature InSb.

The XRD pattern of InSb-10 mole %  $\text{In}_2\text{XTe}$  ( $X = \text{Si}, \text{Ge}, \text{or Sn}$ ) is shown in Figure 3.22, together with the peak positions of literature InSb. The lattice parameter and densities of the samples are summarized in Table 3.5. In the table, the literature data of the lattice parameters for InSb- $\text{In}_2\text{GeTe}$  and InSb- $\text{In}_2\text{SnTe}$  are also shown for comparison. As reported in Ref. [26], all the peaks could be indexed in terms of the zincblende structure with the space group  $F-43m$ . The lattice parameters calculated from the XRD pattern were  $a = 0.6477$  nm

for InSb-In<sub>2</sub>SiTe,  $a = 0.6470$  nm for InSb-In<sub>2</sub>GeTe,  $a = 0.6480$  nm for InSb-In<sub>2</sub>SnTe. The bulk densities of InSb-In<sub>2</sub>SiTe, InSb-In<sub>2</sub>GeTe, and InSb-In<sub>2</sub>SnTe were 87, 82, and 96 % of the theoretical density, respectively.

**Table 3.5** Lattice parameters and sample bulk densities of InSb-10 mole % In<sub>2</sub>XTe (X = Si, Ge, or Sn).

| Compounds  | InSb-In <sub>2</sub> SiTe | InSb-In <sub>2</sub> GeTe        | InSb-In <sub>2</sub> SnTe        |
|--|---------------------------|----------------------------------|----------------------------------|
| Crystal structure                                  | cubic                     | cubic                            | cubic                            |
| Lattice parameter, $a$ (nm)                        | 0.6477                    | 0.6470<br>[0.6471] <sup>26</sup> | 0.6480<br>[0.6471] <sup>26</sup> |
| Theoretical density, $d_{th}$ (gcm <sup>-3</sup> ) | 5.68                      | 5.76                             | 5.78                             |
| Measured density, $d_{exp}$ (gcm <sup>-3</sup> )   | 4.90                      | 4.70                             | 5.53                             |
| Relative density (%)                               | 87                        | 82                               | 96                               |

### 3.4.3.2 Electrical Properties

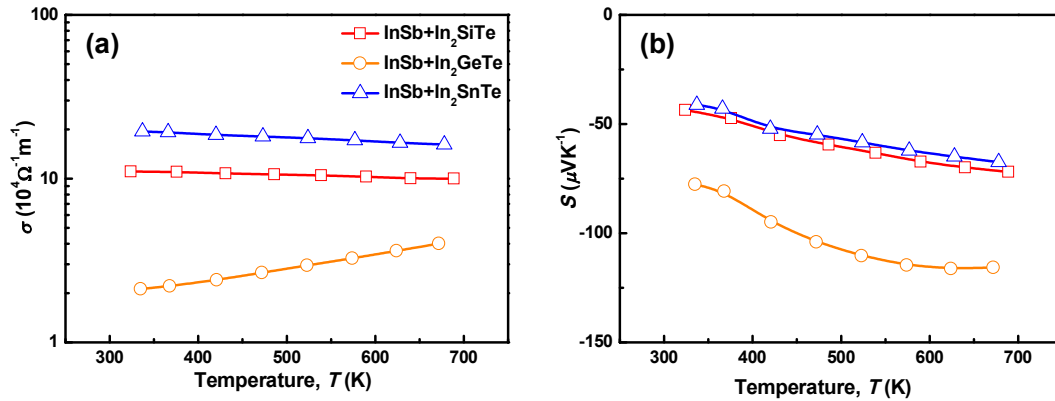


**Figure 3.23** Temperature dependences of (a) the electrical conductivity,  $\sigma$ , and (b) Seebeck coefficient,  $S$  of InSb-10 mole % In<sub>2</sub>XTe (X = Si, Ge, or Sn).

Figure 3.23(a) shows the temperature dependence of the electrical conductivity of InSb-10 mole % In<sub>2</sub>XTe (X = Si, Ge, or Sn). InSb-In<sub>2</sub>SiTe and InSb-In<sub>2</sub>SnTe samples show metallic behavior and the values for two samples were in the order of  $10^5 \Omega^{-1} \text{m}^{-1}$ . However,

the  $\sigma$  values of InSb-In<sub>2</sub>GeTe sample increase with increasing temperature, indicating typical intrinsic semiconductor behavior. The  $\sigma$  values were in the order of  $10^4 \Omega^{-1}\text{m}^{-1}$ . The InSb-In<sub>2</sub>GeTe sample possesses a lower  $\sigma$  value than those of other samples due to its semiconducting behavior. The temperature dependence of  $S$  values was presented in Figure 3.23(b). All samples are negative indicating that the majority of the charge carriers are electron. Since the  $S$  value increases with the decrease in the carrier concentration, the sample of InSb-In<sub>2</sub>GeTe which shows semiconductor behavior has a larger absolute value of  $S$ . The  $S$  value reached a maximum approximately  $-116 \mu\text{VK}^{-1}$  at 624 K for InSb-In<sub>2</sub>GeTe sample. Indeed, the power factor ( $S^2\sigma$ ), defining the electrical performance of TE materials, increases with temperature and reaches a maximum approximately 0.73 of InSb-In<sub>2</sub>GeTe was reached 0.73  $\text{mWm}^{-1}\text{K}^{-2}$  at 678 K as shown in Figure 3.24.

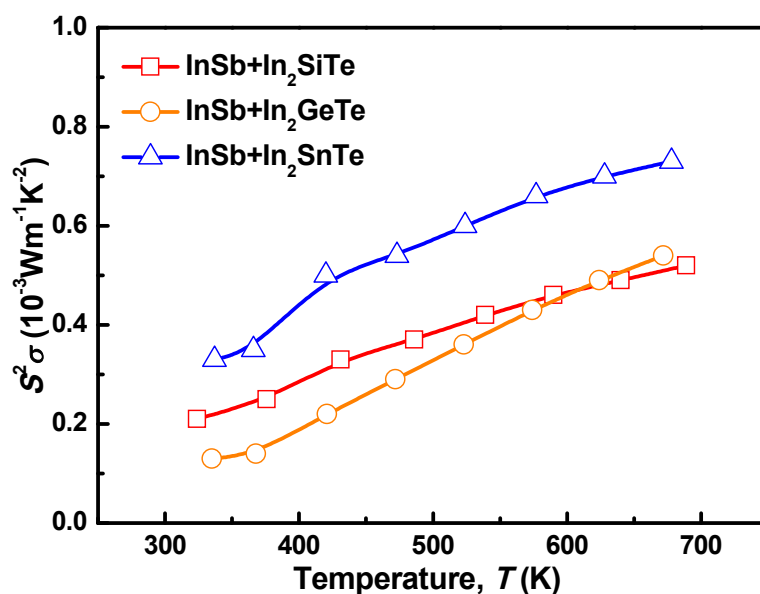


**Figure 3.24** Temperature dependences of power factor,  $S^2\sigma$  ( $\sigma = 1/\rho$ ) of InSb-10 mole % In<sub>2</sub>XTe ( $X = \text{Si}, \text{Ge}, \text{or Sn}$ ).

### 3.4.3.3 Thermal Conductivity

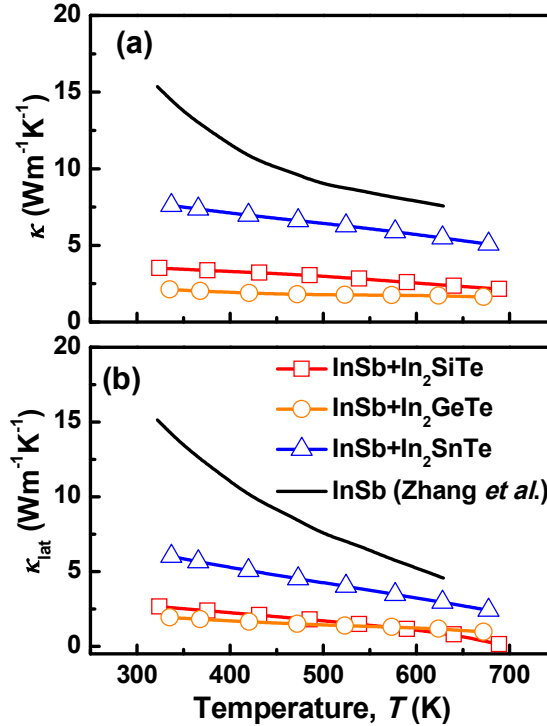


**Figure 3.25** Temperature dependences of the thermal conductivity of InSb-10 mole % In<sub>2</sub>XTe ( $X = \text{Si, Ge, or Sn}$ ), together with the data for pure InSb [7]. (a) total (measured) thermal conductivity,  $\kappa$ , and (b) lattice thermal conductivity,  $\kappa_{\text{lat}} (= \kappa - LT/\rho)$ .

It is well known that the  $\kappa$  of solids is composed mainly of two components:  $\kappa_{\text{lat}}$  and  $\kappa_{\text{el}}$ . We roughly estimated  $\kappa_{\text{el}}$  on the basis of the Wiedemann Franz relationship, using the  $\rho$  data and the Lorenz number ( $L = 2.45 \times 10^{-8} \text{ W}\Omega\text{K}^{-2}$ ), i.e.,  $\kappa_{\text{el}} = LT/\rho$ .  $\kappa_{\text{lat}}$  was obtained by subtracting  $\kappa_{\text{el}}$  from  $\kappa$ . Figure 3.25(a) and 3.25(b) show the temperature dependences of  $\kappa$  and  $\kappa_{\text{lat}} (= \kappa - LT/\rho)$  for the InSb-In<sub>2</sub>XTe ( $X = \text{Si, Ge, or Sn}$ ) samples, together with the data for literature InSb. The  $\kappa$  values of all samples were relatively lower than those of InSb and decreased with increasing temperature, indicating effective phonon scattering. Within the measured temperature range, the lowest  $\kappa$  value was obtained for InSb-In<sub>2</sub>GeTe sample which reaches  $1.63 \text{ Wm}^{-1}\text{K}^{-1}$  at 672 K. InSb-In<sub>2</sub>SnTe shows the largest  $\kappa$  value because of the high electrical conductivity and large density. The  $\kappa_{\text{lat}}$  values of all samples were lower than that of  $\kappa_{\text{lat}}$  for InSb due to increasing phonon scattering by point defects.

### 3.4.3.4 Thermoelectric Properties

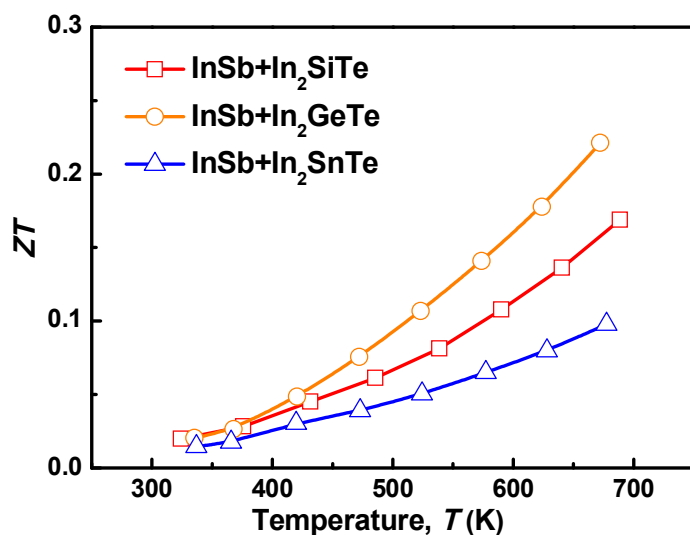


**Figure 3.26** Temperature dependences of  $ZT$  of InSb-10 mole % In<sub>2</sub>XTe ( $X = \text{Si, Ge, or Sn}$ ).

Finally, the temperature dependence of the  $ZT$  value of the InSb-10 mole % In<sub>2</sub>XTe ( $X = \text{Si, Ge, or Sn}$ ) samples is shown in Figure 3.26. The maximum  $ZT$  obtained in the present study was 0.22 at 672 K for InSb-In<sub>2</sub>GeTe sample which shows semiconductor behavior.

### 3.4.4 Conclusions

In this chapter, the author prepared polycrystalline samples of InSb-10 mole % In<sub>2</sub>XTe (X = Si, Ge, or Sn) and characterized its structural and TE properties. All samples were indexed in terms of the zincblende structure with the space group  $F-43m$ . The  $\sigma$  of InSb-In<sub>2</sub>GeTe sample increase with increasing temperature, indicating typical intrinsic semiconductor behavior. However, InSb-In<sub>2</sub>SiTe and InSb-In<sub>2</sub>SnTe samples show metallic behavior. The  $S$  values of all samples are negative indicating that the majority of the charge carriers are electron. InSb-In<sub>2</sub>GeTe sample which show semiconductor behavior has larger absolute value of  $S$  than those of InSb-In<sub>2</sub>SiTe and InSb-In<sub>2</sub>SnTe. The  $\kappa$  values of all samples were relatively lower than those of InSb, likely due to the increasing phonon scattering by point defects. The maximum  $ZT$  obtained in the present study was 0.22 at 672 K for InSb-In<sub>2</sub>GeTe sample.

## Reference

- [1] D. Rode, Phys. Rev. B 3 (1971).
- [2] N. Mingo, Appl. Phys. Lett. 84 (2004).
- [3] S. Yamaguchi, T. Matsumoto, J. Yamazaki, N. Kaiwa and A. Yamamoto, Appl. Phys. Lett. 87 (2005).
- [4] L. I. Berger, *Semiconductor materials*, (CRC Press, Boca Raton, FL, 1997).
- [5] Y. Pei and D. T. Morelli, Appl. Phys. Lett. 94 (2009).
- [6] X. Su, H. Li and X. Tang, J. Phys. D: Appl. Phys. 43 (2010).
- [7] Q. Zhang, Z. Xiong, J. Jiang, W. Li, G. Xu, S. Bai, P. Cui and L. Chen, J. Mater. Chem. 21 (2011).
- [8] E. J. Skoug, J. D. Cain, D. T. Morelli, M. Kirkham, P. Majsztrik and E. Lara-Curzio, J. Appl. Phys. 110 (2011).
- [9] I. Kudman, J Mater Sci 7 (1972).
- [10] I. V. Gasenkova and T. E. Svechnikova, Inorg. Mater. 40 (2004).
- [11] A. G. Briggs, L. J. Challis and F. W. Sheard, Journal of Physics C: Solid State Physics 3 (1970).
- [12] B. Abeles, D. S. Beers, G. D. Cody and J. P. Dismukes, Physical Review 125 (1962).
- [13] K. F. Hsu, S. Loo, F. Guo, W. Chen, J. S. Dyck, C. Uher, T. Hogan, E. K. Polychroniadis and M. G. Kanatzidis, Science 303 (2004).
- [14] B. C. Sales, D. Mandrus and R. K. Williams, Science 272 (1996).
- [15] G. S. Nolas, G. A. Slack and S. B. Schujman, in, 2001, pp. 255-300.
- [16] D. M. Rowe, *CRC handbook of thermoelectrics*, (Boca Raton, FL, CRC Press, 1995).
- [17] D. M. Rowe and R. W. Bunce, J. Phys. D: Appl. Phys. 2 (1969).
- [18] M. Zhou, J.-F. Li and T. Kita, J. Am. Chem. Soc. 130 (2008).
- [19] N. Kaiwa, J. Yamazaki, T. Matsumoto, M. Saito, S. Yamaguchi and A. Yamamoto, Appl. Phys. Lett. 90 (2007).
- [20] V. Cronin, Silicon Germanium, in: CRC Handbook of Thermoelectrics, CRC Press, 1995.
- [21] C. Uher, J. Yang, S. Hu, D. T. Morelli and G. P. Meisner, Phys. Rev. B 59 (1999).
- [22] J. Yang, G. P. Meisner and L. Chen, Appl. Phys. Lett. 85 (2004).
- [23] S. Sakurada and N. Shutoh, Appl. Phys. Lett. 86 (2005).

- [24] J. Callaway and H. C. Von Baeyer, *Physical Review* 120 (1960).
- [25] C. H. L. Goodman, *J. Phys. Chem. Solids* 6 (1958).
- [26] J. C. Woolley and E. W. Williams, *J. Electrochem. Soc.* 111 (1964).



## CHAPTER IV

### Thermoelectric Properties of CoSb<sub>3</sub>-based System

#### 4.1 Tl<sub>x</sub>Fe<sub>1</sub>Co<sub>3</sub>Sb<sub>12</sub> system

##### 4.1.1 Introduction

###### 4.1.1.1 Skutterudites

The name of skutterudite is derived from a naturally occurring mineral with CoAs<sub>3</sub> structure, which was firstly discovered in Skutterud (Norway). Skutterudite compounds have the composition MX<sub>3</sub> where M is one of the group 8 transition metal atom such as Co, Rh, or Ir and X represents a pnictogen atom such as P, As, or Sb. These compounds crystallize in a body-centered cubic structure (*Im3* space group) with 32 atoms in the unit cell, where the transition metals occupy the 8c-sites ( $\frac{1}{4}, \frac{1}{4}, \frac{1}{4}$ ), the pnictogen atoms occupy the 24g-sites (0, y, z), and the most important point is that there are two voids in the unit cell in the 2a-sites (0,0,0) or ( $\frac{1}{2}, \frac{1}{2}, \frac{1}{2}$ ), which can be filled by filler atoms with an ionic radius lower than the cage radius acting as “rattlers” to enhance phonon scattering. Two structural voids in the unit cell can be filled by a variety of guest atoms such as rare earth elements [1-4], alkaline earth metals [5-7], alkali metals [8, 9], and group 13 elements [10-14]. When the guest atom denoted by R incorporates into the cages, the formula of the compounds turns out to be RM<sub>4</sub>X<sub>12</sub>, called filled skutterudites [15]. Figure 1-4 depicts such a structure: the voids inside (red sphere), the transition metals (blue sphere), and the rectangular pnictogen rings (green sphere) [15-17].

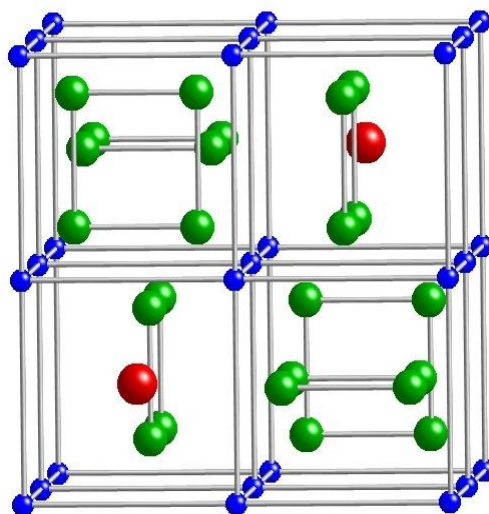


**Figure 4.1** The skutterudite structure of  $RM_4X_{12}$ .

The first such filled skutterudite,  $LaFe_4P_{12}$  was synthesized in 1977 by Jeitschko and Brown [18]. Shortly after, such filled skutterudites were prepared also in the arsenide and antimonide families. A general formula describing a filled skutterudite compound is  $R^{4+}[M_4X_{12}]^{4-}$ , where R is an electropositive filler ion and the exponents indicate the charge balance. It is important to recognize that it is not the neutral  $[M_4X_{12}]$  complex introduced above, but the charged  $[M_4X_{12}]^{4-}$  complex that forms the basis of the filled skutterudites. The filled skutterudite  $R^{4+}[M_4X_{12}]^{4-}$  thus yields a valence electron count 72 and represents a semiconductor and diamagnetic material. The R atom is loosely bonded to the other surrounding atoms and rattles in the oversized cage around its equilibrium position. It is thought that these rattling of the R atoms within the cages resonantly scatter heat carrying phonons and lead to significant reduction in  $\kappa_{lat}$  [19].

Recently, the  $CoSb_3$ -based skutterudites filled by group 13 elements such as Ga, In, or Tl have been drawing attention in the TE research area due to their excellent thermoelectric performance (TE). Herein, the author investigated their composition and TE properties and summarized in Table 4.1. Since the filling atoms in the cages donate their valence electron to the  $CoSb_3$  framework, all  $CoSb_3$ -based skutterudites are *n*-type. However, for a powerful TE module, the similar performance in both *n*- and *p*-type TE materials is required. Compared with *n*-type filled skutterudites, the enthusiasm and efforts on *p*-type skutterudites seem not so significant although *p*-type materials are identically important for TE application as shown in

Figure 4.2. Therefore, the *p*-type CoSb<sub>3</sub>-based skutterudites should be developed. For *p*-type filled skutterudites, charge compensation can be attempted on the 8c site occupied by the iron-group metal. Thus, as the formal valences of Co and Fe in the skutterudites are close to +3 and +2, the partial replacement of Fe with Co can increase the hole concentration and results in *p*-type conduction. In addition, the carrier density can be adjusted by not only the Fe/Co ratio but also the filling fraction of the guest atom in the (Fe, Co)Sb<sub>3</sub> framework. In fact, filling of group 13 elements compensates the hole concentration doped by the replacement of Fe with Co. Among the group 13 elements, Tl is considered as a typical filling atom [12, 20], because the valence of Tl is close to +1. Therefore, I selected Tl as the filling atom in the present study. Furthermore, since the cost of Fe is remarkably lower than that of Co, the partial replacement of Fe with Co can lead to not only *p*-type conduction but also benefit of the material's cost.

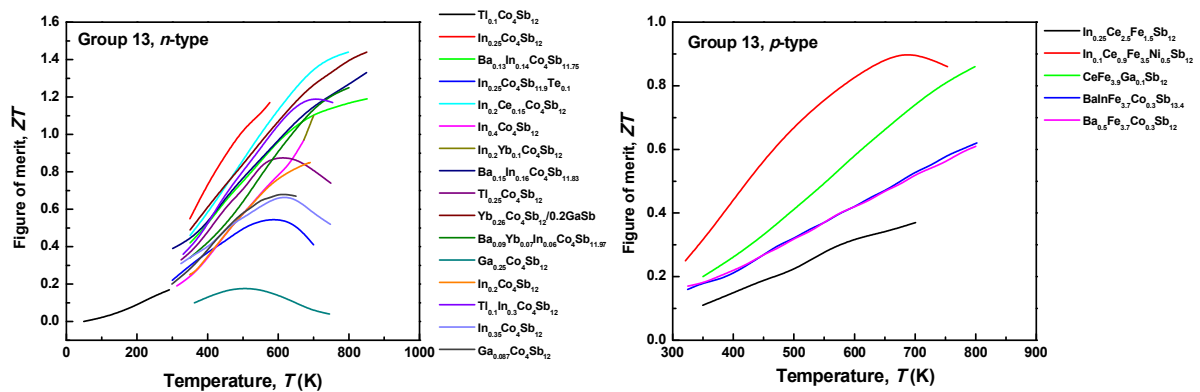


**Figure 4.2** Temperature dependence of  $ZT$  for *n*- and *p*-type skutterudites filled by group 13 elements.

Against this background, I determined the compositions for *p*-type Tl-filled skutterudites to be studied in the present study as Tl<sub>*x*</sub>Fe<sub>1</sub>Co<sub>3</sub>Sb<sub>12</sub> (*x* = 0, 0.2, 0.4, 0.6, and 0.8). Polycrystalline samples of Tl<sub>*x*</sub>Fe<sub>1</sub>Co<sub>3</sub>Sb<sub>12</sub> were prepared and their TE properties were examined.

**Table 4.1** TE properties and composition of Skutterudites filled by group 13 elements (Ga, In, and Tl).

| No | <i>p/n</i> | Group 13 elements |    |    | Cofilling atom | Dopant | Nano inclusion                 | Micro inclusion                       | FFL                | TE properties<br>Max. ZT        | Composition  | Ref. |
|----|------------|-------------------|----|----|----------------|--------|--------------------------------|---------------------------------------|--------------------|---------------------------------|--|------|
|    |            | Ga                | In | Tl |                |        |                                |                                       |                    |                                 |  |      |
| 1  | <i>p/n</i> | -                 | -  | O  | -              | -      | -                              | -                                     | -                  | 0.175 at 300 K                  | Tl <sub>0.1</sub> Co <sub>4</sub> Sb <sub>12</sub>   | [20] |
| 2  | -          | -                 | -  | O  | -              | Fe, Sn | -                              | -                                     | -                  | -                               | -  | [21] |
| 3  | <i>p</i>   | -                 | -  | O  | -              | -      | -                              | -                                     | -                  | -                               | -  | [22] |
| 4  | <i>n</i>   | -                 | O  | -  | -              | -      | -                              | InSb                                  | 0.22               | 1.2 at 575 K                    | In <sub>0.25</sub> Co <sub>4</sub> Sb <sub>12</sub>  | [10] |
| 5  | <i>n</i>   | -                 | O  | -  | Ba             | -      | -                              | -                                     | 0.22 (In)          | 1.19 at 850 K                   | Ba <sub>0.13</sub> In <sub>0.14</sub> Co <sub>4</sub> Sb <sub>11.75</sub>  | [23] |
| 6  | <i>n</i>   | -                 | O  | -  | -              | Te     | -                              | -                                     | 0.25               | 0.54 at 600 K                   | In <sub>0.25</sub> Co <sub>4</sub> Sb <sub>11.9</sub> Te <sub>0.1</sub>  | [24] |
| 7  | -          | -                 | -  | O  | -              | -      | -                              | -                                     | -                  | -                               | -  | [25] |
| 8  | <i>n</i>   | -                 | O  | -  | -              | -      | -                              | -                                     | 0.25               | -                               | -  | [11] |
| 9  | <i>n</i>   | -                 | O  | -  | Ce             | -      | InSb                           | -                                     | <0.15              | 1.43 at 800 K                   | In <sub>0.2</sub> Ce <sub>0.15</sub> Co <sub>4</sub> Sb <sub>12</sub>  | [26] |
| 10 | <i>n</i>   | -                 | O  | -  | -              | -      | -                              | $\gamma$ -CoSb <sub>2</sub> ,<br>InSb | 0.22 (In)          | 0.96 at 673 K                   | In <sub>0.4</sub> Co <sub>4</sub> Sb <sub>12</sub>   | [27] |
| 11 | <i>n</i>   | -                 | O  | -  | Yb             | -      | -                              | -                                     | ~0.2               | 1.1 at 700 K                    | In <sub>0.2</sub> Yb <sub>0.1</sub> Co <sub>4</sub> Sb <sub>12</sub>   | [28] |
| 12 | <i>n</i>   | -                 | O  | -  | Ba             | -      | -                              | BaSb <sub>3</sub> ,<br>InSb           | -                  | 1.34 at 850 K,<br>1.33 at 850 K | Ba <sub>0.15</sub> In <sub>0.16</sub> Co <sub>4</sub> Sb <sub>11.83</sub> ,<br>Ba <sub>0.14</sub> In <sub>0.23</sub> Co <sub>4</sub> Sb <sub>11.84</sub> | [29] |
| 13 | <i>n</i>   | -                 | -  | O  | -              | -      | -                              | -                                     | 0.20-0.2<br>5      | 0.9 at 600 K                    | Tl <sub>0.25</sub> Co <sub>4</sub> Sb <sub>12</sub>  | [12] |
| 14 | <i>p</i>   | -                 | O  | -  | -              | Fe     | -                              | FeSb <sub>2</sub> , Sb                | 0.25               | 0.37 at 700 K                   | In <sub>0.25</sub> Ce <sub>2.5</sub> Fe <sub>1.5</sub> Sb <sub>12</sub>  | [30] |
| 15 | <i>n</i>   | O                 | -  | -  | Yb             | -      | GaSb                           | -                                     | -                  | 1.45 at 850 K                   | Yb <sub>0.26</sub> Co <sub>4</sub> Sb <sub>12</sub> /0.2GaSb   | [31] |
| 16 | <i>n</i>   | -                 | O  | -  | Ba, Yb         | -      | InSb, YbO                      | -                                     | -                  | 1.25 at 800 K                   | Ba <sub>0.090</sub> Yb <sub>0.070</sub> In <sub>0.060</sub> Co <sub>4</sub> Sb <sub>11.97</sub>  | [32] |
| 17 | <i>n</i>   | -                 | O  | -  | -              | -      | In-rich                        | -                                     | -                  | -                               | -  | [33] |
| 18 | <i>n</i>   | O                 | -  | -  | -              | -      | -                              | GaSb                                  | <0.05              | 0.18 at 500 K                   | Ga <sub>0.25</sub> Co <sub>4</sub> Sb <sub>12</sub>  | [13] |
| 19 | <i>n</i>   | -                 | O  | -  | -              | -      | Sb, InSb                       | -                                     | <0.2               | 0.7 at 675 K                    | In <sub>0.2</sub> Co <sub>4</sub> Sb <sub>12</sub> <sup>quenching</sup>  | [34] |
| 20 | <i>p/n</i> | -                 | O  | -  | Lu             | -      | -                              | CoSb <sub>2</sub> , Sb                | -                  | 0.27 at 365 K                   | In <sub>0.13</sub> Lu <sub>0.05</sub> Co <sub>4.02</sub> Sb <sub>12</sub>  | [35] |
| 21 | <i>n</i>   | -                 | O  | O  | -              | -      | In <sub>2</sub> O <sub>3</sub> | -                                     | Tl<0.1,<br>In<0.09 | 1.2 at 700 K                    | Tl <sub>0.1</sub> In <sub>0.3</sub> Co <sub>4</sub> Sb <sub>12</sub>   | [36] |
| 22 | <i>n</i>   | -                 | O  | -  | -              | -      | -                              | InSb,<br>CoSb <sub>2</sub>            | 0.22               | 0.67 at 600 K                   | In <sub>0.35</sub> Co <sub>4</sub> Sb <sub>12</sub>  | [37] |
| 23 | <i>pin</i> | -                 | O  | -  | -              | Ge     | -                              | -                                     | -                  | 0.58 at 673                     | In <sub>0.16</sub> Co <sub>4</sub> Sn <sub>11.95</sub> Ge <sub>0.05</sub>  | [38] |
| 24 | <i>p</i>   | -                 | O  | -  | -              | Fe     | -                              | FeSb <sub>2</sub> , Sb                | -                  | -                               | -  | [39] |
| 25 | <i>p</i>   | -                 | O  | -  | Ce             | Fe     | -                              | InSb                                  | -                  | 0.9 at 650 K                    | In <sub>0.1</sub> Ce <sub>0.9</sub> Fe <sub>3.5</sub> Ni <sub>0.5</sub> Sb <sub>12</sub>   | [40] |
| 26 | <i>p</i>   | O                 | -  | -  | -              | -      | -                              | GaSb, Sb                              | 0.11               | 0.85 at 800 K                   | CeFe <sub>3.9</sub> Ga <sub>0.1</sub> Sb <sub>12</sub>   | [41] |
| 27 | <i>p</i>   | -                 | O  | -  | Ba             | Fe     | -                              | InSb,<br>FeSb <sub>2</sub>            | -                  | 0.63 at 800 K                   | BaInFe <sub>3.7</sub> Co <sub>0.3</sub> Sb <sub>13.4</sub>   | [42] |
| 28 | <i>n</i>   | O                 | -  | -  | -              | -      | -                              | GaSb, Sb                              | -                  | 0.7 at 600 K                    | Ga <sub>0.087</sub> Co <sub>4</sub> Sb <sub>12</sub>   | [14] |
| 29 | <i>p</i>   | -                 | O  | -  | Ba             | -      | -                              | BaSb <sub>3</sub> , Sb                | -                  | 0.61 at 800 K                   | Ba <sub>0.5</sub> Fe <sub>3.7</sub> Co <sub>0.5</sub> Sb <sub>12</sub>   | [43] |

## 4.1.2 Experimental Procedures

### 4.1.2.1 Sample Preparation

The synthesis of the polycrystalline samples of Tl<sub>x</sub>Fe<sub>1</sub>Co<sub>3</sub>Sb<sub>12</sub> prepared from the starting materials was chunks of Tl (99.999 %), Fe (99.99 %), Co (> 99.99 %), and Sb (99.99 %). The starting materials were weighed out in a stoichiometric ratio and loaded into the silica tubes which were covered by carbon sheet. Because Tl metal readily oxidizes in air and is toxic, it was handled and loaded in the glove box under a N<sub>2</sub> atmosphere. The silica tube was sealed under vacuum and transferred into a programmable furnace. The silica tube was heated to 1323 K at 1 K/min and kept for about 48 h. The silica tube containing the homogeneous molten liquid was quenched into a water bath and then annealed at 773 K for 1 week to correct crystallographic phase. The completely reacted solid was removed from the silica tube and cleaned to remove small amounts of carbon from the surface. The obtained ingots of Tl<sub>x</sub>Fe<sub>1</sub>Co<sub>3</sub>Sb<sub>12</sub> were crushed into fine powders. The as-prepared powders of Tl<sub>x</sub>Fe<sub>1</sub>Co<sub>3</sub>Sb<sub>12</sub> were sintered by hot pressing in graphite dies under pressure of 45 MPa at 932 K for 2 h under flowing Ar. The bulk samples were cleaned the surface for measuring the weight and dimensions.

### 4.1.2.2 Experimental Details

#### 4.1.2.2.1 X-ray Diffraction Analysis

X-ray diffraction (XRD) measurements were performed on a Rigaku, RINT2000 series X-ray diffractometer using Cu-K $\alpha$  radiation at room temperature. The powder X-ray diffraction patterns were taken from 10 to 120°. The lattice parameter, unit cell volume and theoretical density were estimated from the XRD results.

#### 4.1.2.2.2 Electrical Resistivity and Seebeck coefficient

The electrical resistivity ( $\rho$ ) and the Seebeck coefficient ( $S$ ) were performed by using a commercially available apparatus ULVAC, ZEM-1 in a helium atmosphere and over the temperature range of 300 to 723 K.

#### 4.1.2.2.3 Carrier Concentration and Mobility

The Hall effect was measured by the van der Pauw method using a dc Hall effect measurement apparatus Resitest8300 (Toyo Technica) in vacuum at room temperature under an applied magnetic field of 0.5 T.

#### **4.1.2.2.4 Thermal Diffusivity**

The thermal diffusivity was performed by the laser flash method using ULVAC, TC-7000 in vacuum and over the temperature range of 300 to 723 K. The thermal conductivity ( $\kappa$ ) of the specimens was evaluated from the thermal diffusivity ( $\alpha$ ), the heat capacity ( $C_P$ ) and the experimental density ( $d$ ) using the following relationship ( $\kappa = \alpha C_P d$ ).

#### **4.1.2.2.5 Heat Capacity**

The heat capacity ( $C_P$ ) of the sample was estimated from the Dulong-Petit model,  $C_P = 3nR$ , where  $n$  is the number of atoms per formula unit and  $R$  is the gas constant.

#### **4.1.2.2.6 Density**

The densities ( $d$ ) of the samples were calculated on the basis of the measured weight and dimensions. Density is a measure of mass per unit of volume. The unit of density is the kilogram per cubic meter ( $\text{kg/m}^3$ ). To obtain accurate densities, the measurements were performed several times after careful polishing of all samples.

#### **4.1.2.2.7 Scanning Electron Microscopy**

The Field Emission Scanning Electron Microscopy (FE-SEM) was used to observe microstructures of the samples. The FE-SEM observations were performed on a JEOL, JSM-6500F in vacuum at room temperature.

#### **4.1.2.2.8 Energy Dispersive X-Ray Spectroscopy**

Energy Dispersive X-ray spectroscopy (EDX) is a micro-analytical technique that uses the characteristic spectrum of X-rays emitted by the specimen after excitation by high-energy electrons to obtain information about its elemental composition. The EDX analysis here was performed on a JEOL, JSM-6500F in vacuum at room temperature.

#### **4.1.2.2.9 Dimensionless Figure of Merit**

The dimensionless figure of merit ( $ZT$ ) was calculated by using the above mentioned values of the Seebeck coefficient ( $S$ ), electrical resistivity ( $\rho$ ) and thermal conductivity ( $\kappa$ ), according to the relation ( $ZT = \frac{S^2 T}{\rho \kappa}$ ).

## 4.1.3 Results and Discussion

### 4.1.3.1 Sample identification

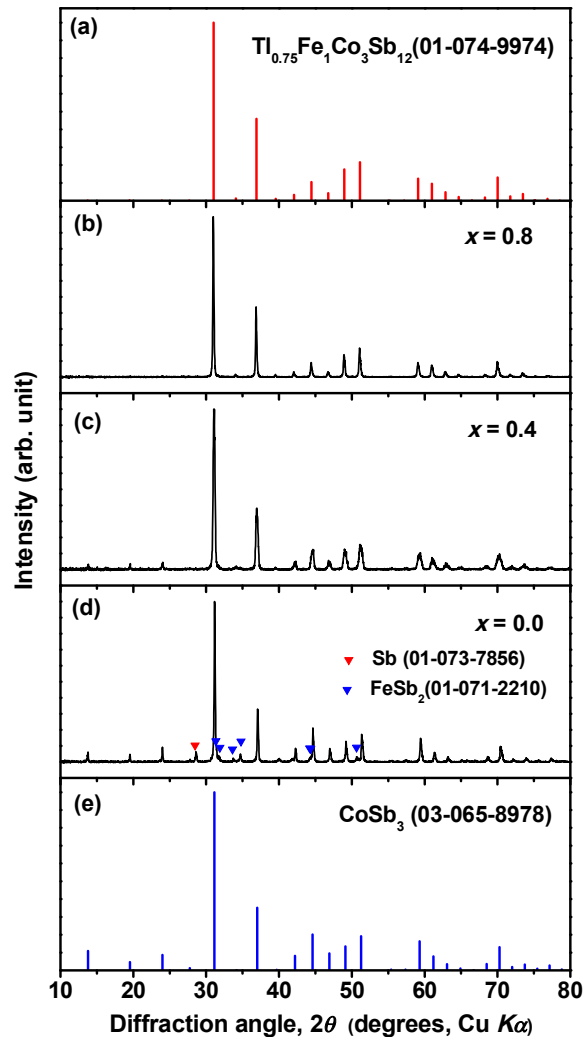


**Figure 4.3** (b~d) Powder XRD patterns of polycrystalline samples of  $Ti_xFe_1Co_3Sb_{12}$  ( $x = 0, 0.4,$  and  $0.8$ ), together with the peak position of (a)  $Ti_{0.75}Fe_1Co_3Sb_{12}$  and (e)  $CoSb_3$ .

Figure 4.3 shows the powder XRD patterns of  $\text{Tl}_x\text{Fe}_1\text{Co}_3\text{Sb}_{12}$  ( $x = 0, 0.4, \text{ and } 0.8$ ) polycrystalline samples, together with the literature data of  $\text{Tl}_{0.75}\text{Fe}_1\text{Co}_3\text{Sb}_{12}$  and  $\text{CoSb}_3$ . All samples were identified as skutterudite compounds, although a few small peaks of Sb and  $\text{FeSb}_2$  as an impurity phase existed in the XRD pattern of the sample of  $x = 0$ . It was clearly observed that the intensity of the peak at around  $2\theta = 24^\circ$  decreased with increasing Tl-filling fraction,  $x$ . This decrease is an evidence of Tl filling, because this peak will disappear when the structural cages are fully occupied by the filling atom [44].

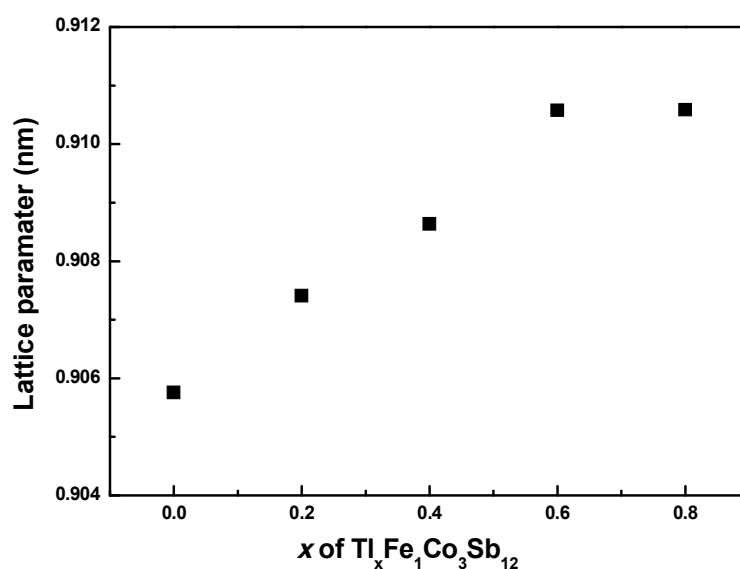


**Figure 4.4** The lattice parameter as a function of Tl-filling fraction,  $x$  for  $\text{Tl}_x\text{Fe}_1\text{Co}_3\text{Sb}_{12}$  ( $x = 0, 0.2, 0.4, 0.6, \text{ and } 0.8$ )

The lattice parameters calculated from the XRD patterns are summarized in Table 4.2 and plotted in Figure 4.4 as a function of  $x$ . The lattice parameters increased almost linearly with increasing  $x$  up to around  $x = 0.6$  and, after that, remained a constant. This result implies that the filling limit of Tl in  $\text{Fe}_1\text{Co}_3\text{Sb}_{12}$  is between  $x = 0.4$  and  $0.6$  in  $\text{Tl}_x\text{Fe}_1\text{Co}_3\text{Sb}_{12}$ . High density samples (above 98% of the theoretical density) were obtained in the present study, as summarized in Table 4.2.

**Table 4.2** Lattice parameter  $a$ , density  $d$ , Seebeck coefficient  $S$  (300 K), electrical resistivity (300 K), carrier concentration  $n_H$  (300 K), Hall mobility  $\mu_H$  (300 K) for polycrystalline samples of Tl <sub>$x$</sub> Fe<sub>1</sub>Co<sub>3</sub>Sb<sub>12</sub> ( $x = 0, 0.2, 0.4, 0.6, \text{ and } 0.8$ ).

|  | Tl filling fraction, $x$ of Tl <sub><math>x</math></sub> Fe <sub>1</sub> Co <sub>3</sub> Sb <sub>12</sub> |        |        |        |        |
|--|---|--------|--------|--------|--------|
|  | 0   | 0.2    | 0.4    | 0.6    | 0.8    |
| Lattice parameter, $a$ (nm)                        | 0.9058  | 0.9074 | 0.9086 | 0.9105 | 0.9106 |
| Theoretical density, $d_{th}$ (gcm <sup>-3</sup> ) | 7.57  | 7.71   | 7.86   | 8.00   | 8.17   |
| Measured density, $d_{exp}$ (gcm <sup>-3</sup> )   | 7.54  | 7.63   | 7.78   | 7.90   | 8.02   |
| Relative density (%)                               | 99  | 99     | 99     | 98     | 98     |

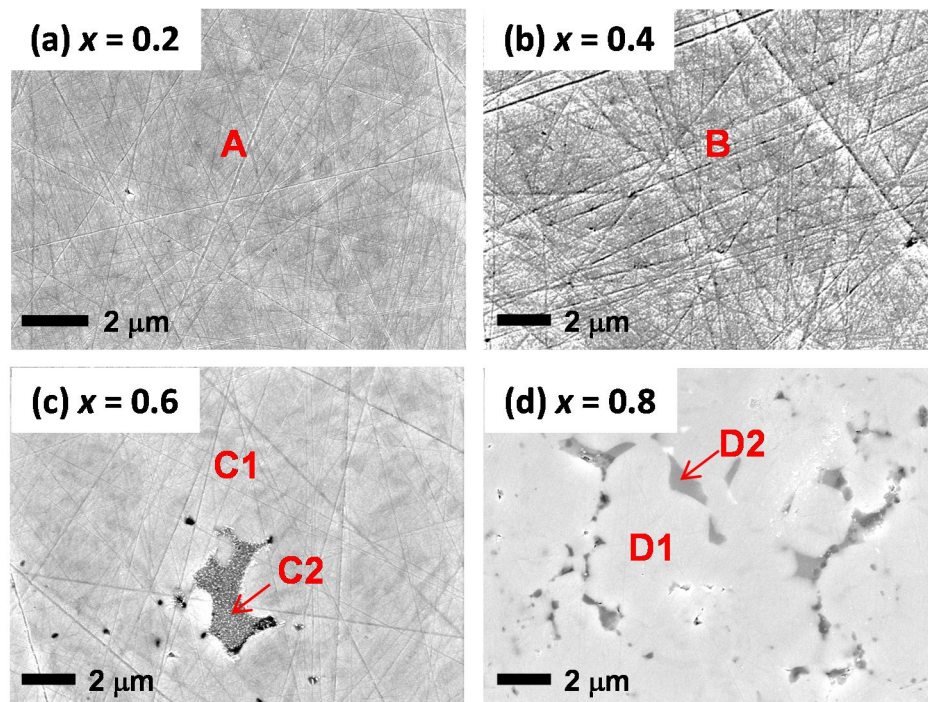


**Figure 4.5** FE-SEM images of hot-pressed samples of Tl <sub>$x$</sub> Fe<sub>1</sub>Co<sub>3</sub>Sb<sub>12</sub>; (a)  $x = 0.2$ , (b)  $x = 0.4$ , (c)  $x = 0.6$  and (d)  $x = 0.8$ .

In order to clarify the filling limit of Tl in Fe<sub>1</sub>Co<sub>3</sub>Sb<sub>12</sub>, the FE-SEM and EDX analysis were performed on the surface of the hot-pressed samples. The FE-SEM images of the

samples of  $x = 0.2$ ,  $0.4$ ,  $0.6$ , and  $0.8$  are shown in Figure 4.5(a), 4.5(b), 4.5(c) and 4.5(d), respectively. The chemical compositions at points A, B, C1, C2, D1 and D2 in Figure 4.6 determined by the quantitative EDX analysis are summarized in Table 4.3. Figure 4.5(a) and (b) show that there are no impurity phases in the sample of  $x = 0.2$  and  $x = 0.4$ . The chemical composition of these phases are  $\text{Tl}_{0.16}\text{Fe}_{1.00}\text{Co}_{3.17}\text{Sb}_{12.33}$  for  $x = 0.2$  and  $\text{Tl}_{0.39}\text{Fe}_{1.00}\text{Co}_{2.97}\text{Sb}_{12.03}$ , well consistent with the nominal composition. On the other hand, as shown in Figure 4.5(c) and 4.5(d), the impurity phases were clearly observed in the FE-SEM images of the samples of  $x = 0.6$  and  $0.8$ . As summarized in Table 4.3, the impurity phases indicated as points C2 and D2 in the FE-SEM images were composed mainly of Tl, Fe, and Sb. And at that time, the chemical compositions of the matrix phases indicated as points C1 and D1 were  $\text{Tl}_{0.42}\text{Fe}_{1.00}\text{Co}_{2.92}\text{Sb}_{12.16}$  and  $\text{Tl}_{0.71}\text{Fe}_{1.00}\text{Co}_{3.03}\text{Sb}_{12.20}$ , respectively. From the results of the XRD and the FE-SEM/EDX analyses, it is concluded that the filling limit of Tl in  $\text{Fe}_1\text{Co}_3\text{Sb}_{12}$  is between  $x = 0.4$  and  $0.6$  in  $\text{Tl}_x\text{Fe}_1\text{Co}_3\text{Sb}_{12}$  and Tl added after exceeding the maximum filling limit precipitates as a Tl-Fe-Sb ternary alloy. The filling fraction of  $\text{Tl}_x\text{Fe}_1\text{Co}_3\text{Sb}_{12}$  was larger than that of  $\text{Tl}_x\text{Co}_4\text{Sb}_{12}$  [13]. Experimentally it was found that a maximum filling fraction can be increased by increasing the amount of Fe substituting for Co in  $\text{CoSb}_3$  skutterudite. When Co is replaced by Fe in  $\text{CoSb}_3$  frame, the void becomes larger because the void radius of  $\text{FeSb}_3$  is larger than that of  $\text{CoSb}_3$  (the void radius is  $\sim 1.89\text{\AA}$  for  $\text{CoSb}_3$  and  $\sim 1.98\text{\AA}$  for  $\text{FeSb}_3$ ).

**Table 4.3.** Chemical compositions of points 1, 2, 3, 4, and 5 in Figure 4.5, determined from the quantitative EDX analysis.

| Points in Figure<br>4.5 | Chemical composition (at %) |    |    |    | Phase   |
|-------------------------|-----------------------------|----|----|----|---|
|                         | Tl                          | Fe | Co | Sb |   |
| A                       | 1                           | 6  | 19 | 74 | $\text{Tl}_{0.16}\text{Fe}_{1.00}\text{Co}_{3.17}\text{Sb}_{12.33}$ |
| B                       | 3                           | 6  | 18 | 73 | $\text{Tl}_{0.39}\text{Fe}_{1.00}\text{Co}_{2.97}\text{Sb}_{12.03}$ |
| C1                      | 3                           | 6  | 18 | 73 | $\text{Tl}_{0.42}\text{Fe}_{1.00}\text{Co}_{2.92}\text{Sb}_{12.16}$ |
| C2                      | 50                          | 28 | 4  | 18 | A Tl-Fe-Sb ternary alloy  |
| D1                      | 40                          | 23 | 7  | 30 | A Tl-Fe-Sb ternary alloy  |
| D2                      | 4                           | 6  | 18 | 72 | $\text{Tl}_{0.71}\text{Fe}_{1.00}\text{Co}_{3.03}\text{Sb}_{12.20}$ |

### 4.1.3.2 Thermoelectric Properties

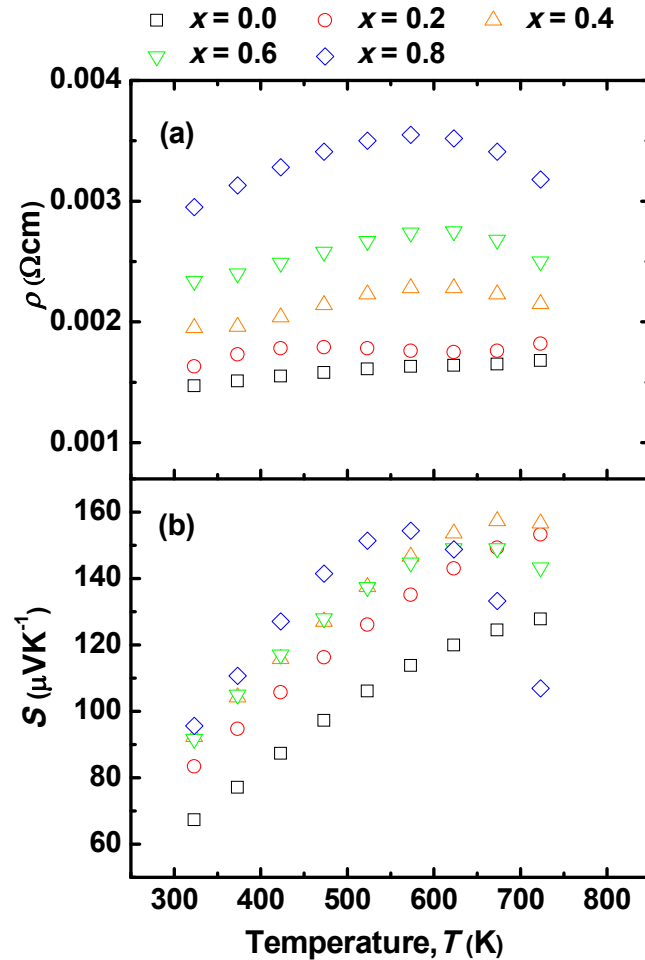


**Figure 4.6** Temperature dependence of (a) electrical resistivity  $\rho$ , (b) Seebeck coefficient  $S$  for polycrystalline samples of Tl<sub>*x*</sub>Fe<sub>1</sub>Co<sub>3</sub>Sb<sub>12</sub> ( $x = 0, 0.2, 0.4, 0.6, \text{ and } 0.8$ ).

Figure 4.6 shows the temperature dependence of (a) electrical resistivity,  $\rho$ , (b) Seebeck coefficient,  $S$  for polycrystalline samples of Tl<sub>*x*</sub>Fe<sub>1</sub>Co<sub>3</sub>Sb<sub>12</sub>. All samples showed positive  $S$  values, which is caused by the fact that the partial replacement of Fe with Co in CoSb<sub>3</sub> increases the hole concentration and results in the  $p$ -type conduction. At 330 K, the values of  $\rho$  and  $S$  of the parent compound, Fe<sub>1</sub>Co<sub>3</sub>Sb<sub>12</sub>, were 0.0014  $\Omega\text{ cm}$  and 63  $\mu\text{V K}^{-1}$ , respectively. As shown in Figure 4.6(a) and 4.6(b), both the  $\rho$  and  $S$  of Tl<sub>*x*</sub>Fe<sub>1</sub>Co<sub>3</sub>Sb<sub>12</sub> increased with increasing  $x$ , indicating that the hole concentration decreased with increasing  $x$ . Since the valence of Tl is +1, the Tl-filling donates an electron in Tl<sub>*x*</sub>Fe<sub>1</sub>Co<sub>3</sub>Sb<sub>12</sub>. The  $S$  of Tl<sub>0.8</sub>Fe<sub>1</sub>Co<sub>3</sub>Sb<sub>12</sub> increased with temperature to the maximum value at around 573 K and then

decreased dramatically. One of the reasons of this decrease in  $S$  at high temperature is onset of bipolar conduction. It can be seen that this onset of bipolar conduction shifts to lower temperature with increasing  $x$ . This observation implies that the Tl-adding results in the decrease of the hole concentration and enhances the effect of minority carriers (in the present case, electrons) on the transport properties at high temperature.

### 4.1.3.3 Thermal Conductivity

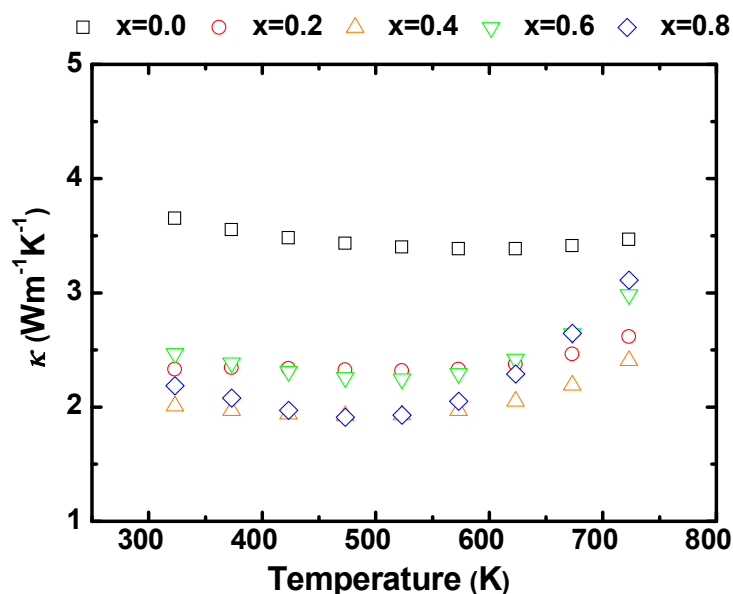


**Figure 4.7** Temperature dependence of thermal conductivity  $\kappa$  for polycrystalline samples of  $\text{Tl}_x\text{Fe}_1\text{Co}_3\text{Sb}_{12}$  ( $x = 0, 0.2, 0.4, 0.6,$  and  $0.8$ ).

The  $\kappa$  of  $\text{Tl}_x\text{Fe}_1\text{Co}_3\text{Sb}_{12}$  was significantly reduced by Tl addition, as shown in Figure 4.7. At room temperature, the  $\kappa$  values of  $\text{Fe}_1\text{Co}_3\text{Sb}_{12}$  and  $\text{Tl}_{0.4}\text{Fe}_1\text{Co}_3\text{Sb}_{12}$  were approximately 3.7 and 2.0  $\text{Wm}^{-1}\text{K}^{-1}$ , respectively.  $\text{Tl}_{0.4}\text{Fe}_1\text{Co}_3\text{Sb}_{12}$  exhibited the lowest  $\kappa$  values over the entire temperature range. Owing to effective phonon scattering by the rattling of Tl,  $\kappa$  was dramatically reduced by Tl addition in the composition range of  $x \leq 0.4$ . However, for  $x \geq 0.6$ ,  $\kappa$  increased slightly with increasing  $x$ , likely due to the secondary phase in these samples. That is, the Tl-Fe-Sb ternary alloy, whose  $\kappa$  values were larger than those for the skutterudite matrix phases, increased the  $\kappa$  of the samples.

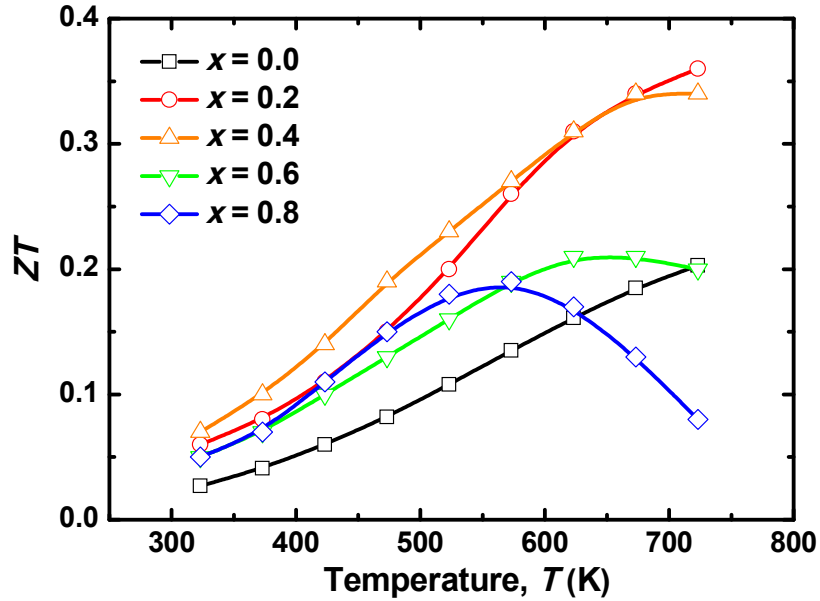


**Figure 4.8** Temperature dependence of (a) electrical resistivity  $\rho$ , (b) Seebeck coefficient  $S$ , (c) thermal conductivity  $\kappa$ , and (d) dimensionless figure of merit  $ZT$  for polycrystalline samples of Tl<sub>x</sub>Fe<sub>1</sub>Co<sub>3</sub>Sb<sub>12</sub> ( $x = 0, 0.2, 0.4, 0.6, \text{ and } 0.8$ ).

The lowest  $\kappa$  of Tl<sub>0.2</sub>Fe<sub>1</sub>Co<sub>3</sub>Sb<sub>12</sub> resulted in a relatively large  $ZT$ , as shown in Figure 4.8. A maximum  $ZT$  value of 0.36 was obtained at 723 K for Tl<sub>0.2</sub>Fe<sub>1</sub>Co<sub>3</sub>Sb<sub>12</sub>.

The temperature dependences of the  $\kappa_{\text{lat}}$  of Co<sub>4</sub>Sb<sub>12</sub>, Tl<sub>0.2</sub>Co<sub>4</sub>Sb<sub>12</sub>, and Tl<sub>0.2</sub>Fe<sub>1</sub>Co<sub>3</sub>Sb<sub>12</sub> are shown in Figure 4.9.  $\kappa_{\text{lat}}$  was obtained by subtracting  $\kappa_{\text{el}}$  ( $= L\sigma T$ , where  $\sigma$  is the electrical conductivity and  $L$  is the Lorentz number  $= 2.45 \times 10^{-8} \text{ W}\Omega\text{K}^{-2}$ ) from measured  $\kappa$ , i.e.,  $\kappa_{\text{lat}} = \kappa - L\sigma T$ . A comparison between the  $\kappa_{\text{lat}}$  values of Co<sub>4</sub>Sb<sub>12</sub> and Tl<sub>0.2</sub>CoSb<sub>12</sub> reveals a significant reduction of  $\kappa_{\text{lat}}$ . This reduction of  $\kappa_{\text{lat}}$  was due to effective phonon scattering by rattling of Tl [23]. Additionally, by comparing the  $\kappa_{\text{lat}}$  values of Tl<sub>0.2</sub>CoSb<sub>12</sub> and Tl<sub>0.2</sub>Fe<sub>1</sub>Co<sub>3</sub>Sb<sub>12</sub>, it can be seen that the partial replacement of Fe with Co yields a further reduction of  $\kappa_{\text{lat}}$ . Therefore, it can be said that not only Tl-filing but also the partial replacement of Fe with Co is effective to reduce the  $\kappa_{\text{lat}}$  of CoSb<sub>3</sub>.

#### 4.1.3.4 Lattice Thermal Conductivity

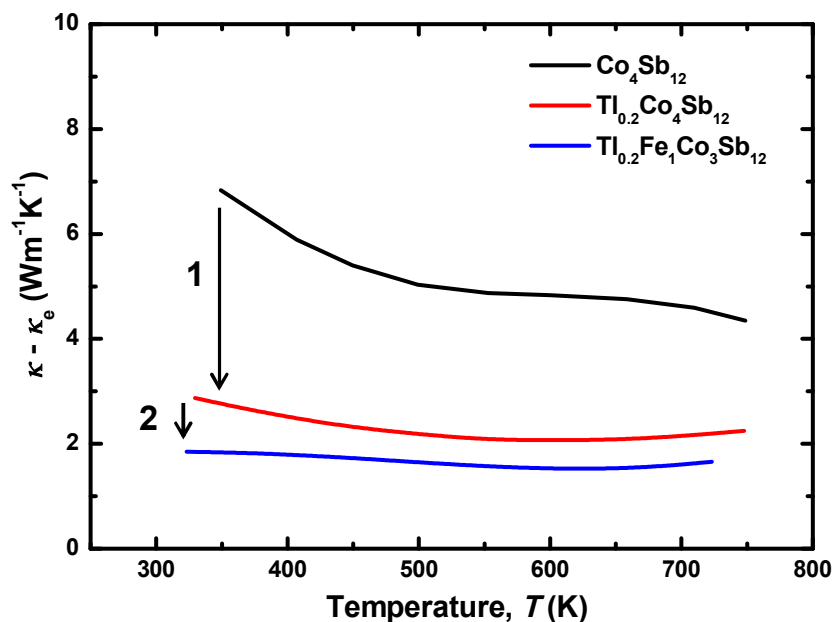


**Figure 4.9** Temperature dependence of the lattice conductivity ( $\kappa_{\text{lat}}$ ) of polycrystalline samples of  $\text{Co}_4\text{Sb}_{12}$ ,  $\text{Tl}_{0.2}\text{Co}_4\text{Sb}_{12}$ , and  $\text{Tl}_{0.2}\text{Fe}_1\text{Co}_3\text{Sb}_{12}$ . The numbers 1 and 2 in the figure represent phonon scattering by Tl-rattling and the partial replacement of Fe with Co in  $\text{CoSb}_3$ , respectively.

#### 4.1.4 Conclusions

In the present study, fully dense samples of polycrystalline *p*-type Tl-filled skutterudites having the compositions of  $\text{Tl}_x\text{Fe}_1\text{Co}_3\text{Sb}_{12}$  ( $x = 0, 0.2, 0.4, 0.6,$  and  $0.8$ ) were prepared, and their high-temperature TE properties were examined. The filling fraction limit was between  $x = 0.4$  and  $0.6$  in  $\text{Tl}_x\text{Fe}_1\text{Co}_3\text{Sb}_{12}$ . All samples exhibited positive  $S$  values. Tl-adding into  $\text{Fe}_1\text{Co}_3\text{Sb}_{12}$  increased the  $\rho$  and the absolute  $S$ , and effectively reduced the  $\kappa_{\text{lat}}$ . The partial replacement of Fe in Co also decreased the  $\kappa_{\text{lat}}$ . Tl-adding decreased the hole concentration because the valence of Tl is +1 so Tl-adding compensates the hole concentration doped by the replacement of Fe with Co.  $\text{Tl}_{0.2}\text{Fe}_1\text{Co}_3\text{Sb}_{12}$  showed the lowest  $\kappa$

over the entire temperature range. A maximum  $ZT$  was 0.36 at 723 K obtained for Tl<sub>0.2</sub>Fe<sub>1</sub>Co<sub>3</sub>Sb<sub>12</sub>. Consequently, a better TE performance was obtained at below the filling fraction limit due to low the  $\kappa$ . I consider that further improvement may be achieved by changing the Fe/Co ratio or by the alteration of filling atoms. The results will be reported in near future.

## Reference

- [1] D. T. Morelli, G. P. Meisner, B. Chen, S. Hu and C. Uher, *Phys. Rev. B* 56 (1997).
- [2] G. S. Nolas, M. Kaeser, R. T. Littleton Iv and T. M. Tritt, *Appl. Phys. Lett.* 77 (2000).
- [3] J. G. A. Lamberton, S. Bhattacharya, R. T. Littleton Iv, M. A. Kaeser, R. H. Tedstrom, T. M. Tritt, J. Yang and G. S. Nolas, *Appl. Phys. Lett.* 80 (2002).
- [4] V. L. Kuznetsov, L. A. Kuznetsova and D. M. Rowe, *J. Phys.: Condens. Matter* 15 (2003).
- [5] L. D. Chen, T. Kawahara, X. F. Tang, T. Goto, T. Hirai, J. S. Dyck, W. Chen and C. Uher, *J. Appl. Phys.* 90 (2001).
- [6] M. Puyet, B. Lenoir, A. Dauscher, M. Dehmas, C. Stiewe and E. Muller, *J. Appl. Phys.* 95 (2004).
- [7] X. Y. Zhao, X. Shi, L. D. Chen, W. Q. Zhang, W. B. Zhang and Y. Z. Pei, *J. Appl. Phys.* 99 (2006).
- [8] Y. Z. Pei, L. D. Chen, W. Zhang, X. Shi, S. Q. Bai, X. Y. Zhao, Z. G. Mei and X. Y. Li, *Appl. Phys. Lett.* 89 (2006).
- [9] Y. Z. Pei, J. Yang, L. D. Chen, W. Zhang, J. R. Salvador and J. Yang, *Appl. Phys. Lett.* 95 (2009).
- [10] T. He, J. Chen, H. D. Rosenfeld and M. A. Subramanian, *Chem. Mater.* 18 (2006).
- [11] R. C. Mallik, J. Y. Jung, S. C. Ur and I. H. Kim, *Met. Mater. Int.*, 14 (2008).
- [12] A. Harnwungmoung, K. Kurosaki, H. Muta and S. Yamanaka, *Appl. Phys. Lett.* 96 (2010).
- [13] A. Harnwungmoung, K. Kurosaki, T. Plirdpring, T. Sugahara, Y. Ohishi, H. Muta and S. Yamanaka, *J. Appl. Phys.* 110 (2011).
- [14] Y. Qiu, L. Xi, X. Shi, P. Qiu, W. Zhang, L. Chen, J. R. Salvador, J. Y. Cho, J. Yang, Y.-c. Chien, S.-w. Chen, Y. Tang and G. J. Snyder, *Adv. Funct. Mater.* (2013).
- [15] C. Uher, Chapter 5 Skutterudites: Prospective novel thermoelectrics, in: T.M. Tritt (Ed.) *Recent Trends in Thermoelectric Materials Research I, Semiconductors and Semimetals*, Academic, San Diego, 2001, pp. 139-253.
- [16] D. M. Rowe, *CRC handbook of thermoelectrics*, (Boca Raton, FL, CRC Press, 1995).
- [17] G. S. Nolas, J. Sharp and J. Goldsmid, *Thermoelectrics: Basic Principles and New Materials Developments*, (Springer, New York, 2001).
- [18] W. Jeitschko and D. Braun, *Acta Crystallographica Section B* 33 (1977).

- [19] G. S. Nolas, J. L. Cohn and G. A. Slack, *Phys. Rev. B* 58 (1998).
- [20] B. C. Sales, B. C. Chakoumakos and D. Mandrus, *Phys. Rev. B* 61 (2000).
- [21] G. J. Long, B. Mahieu, B. C. Sales, R. P. Hermann and F. Grandjean, *J. Appl. Phys.* 92 (2002).
- [22] R. P. Hermann, R. Jin, W. Schweika, F. Grandjean, D. Mandrus, B. C. Sales and G. J. Long, *Phys. Rev. Lett.* 90 (2003).
- [23] W. Y. Zhao, C. L. Dong, P. Wei, W. Guan, L. S. Liu, P. C. Zhai, X. F. Tang and Q. J. Zhang, *J. Appl. Phys.* 102 (2007).
- [24] J.-Y. Jung, S.-C. Ur and I.-H. Kim, *Mater. Chem. Phys.* 108 (2008).
- [25] A. Leithe-Jasper, W. Schnelle, H. Rosner, R. Cardoso-Gil, M. Baenitz, J. Mydosh, Y. Grin, M. Reissner and W. Steiner, *Phys. Rev. B* 77 (2008).
- [26] H. Li, X. Tang, Q. Zhang and C. Uher, *Appl. Phys. Lett.* 94 (2009).
- [27] R. Mallik, C. Stiewe, G. Karpinski, R. Hassdorf and E. Müller, *J. Electron. Mater.* 38 (2009).
- [28] J. Peng, J. He, Z. Su, P. N. Alboni, S. Zhu and T. M. Tritt, *J. Appl. Phys.* 105 (2009).
- [29] W. Zhao, P. Wei, Q. Zhang, C. Dong, L. Liu and X. Tang, *J. Am. Chem. Soc.* 131 (2009).
- [30] K.-H. Park, J.-Y. Jung, S.-C. Ur and I.-H. Kim, *J. Electron. Mater.* 39 (2010).
- [31] Z. Xiong, X. Chen, X. Huang, S. Bai and L. Chen, *Acta Mater.* 58 (2010).
- [32] S. Ballikaya, G. Wang, K. Sun and C. Uher, *J. Electron. Mater.* 40 (2011).
- [33] Y. Du, K. F. Cai, S. Chen, Z. Qin and S. Z. Shen, *J. Electron. Mater.* 40 (2011).
- [34] A. Sesselmann, T. Dasgupta, K. Kelm, E. Müller, S. Perlt and S. Zastrow, *J. Mater. Res.* 26 (2011).
- [35] G. D. Tang, Z. H. Wang, X. N. Xu, Y. He, L. Qiu and Y. W. Du, *J. Electron. Mater.* 40 (2011).
- [36] A. Harnwungmoung, K. Kurosaki, A. Kosuga, M. Ishimaru, T. Plirdpring, R. Yimnirun, J. Jutimoosik, S. Rujirawat, Y. Ohishi, H. Muta and S. Yamanaka, *J. Appl. Phys.* 112 (2012).
- [37] G. Li, K. Kurosaki, Y. Ohishi, H. Muta and S. Yamanaka, *J. Electron. Mater.* (2012).
- [38] R. C. Mallik, E. Mueller and I.-H. Kim, *J. Appl. Phys.* 111 (2012).
- [39] K. H. Park, S. W. You, S. C. Ur, I. H. Kim, S. M. Choi and W. S. Seo, *J. Korean Phys. Soc.* 60 (2012).
- [40] P. Puneet, J. He, S. Zhu and T. M. Tritt, *J. Appl. Phys.* 112 (2012).

- [41] G. Tan, S. Wang, X. Tang, H. Li and C. Uher, *J. Solid State Chem.* 196 (2012).
- [42] J. Yu, W. Y. Zhao, P. Wei, D. G. Tang and Q. J. Zhang, *J. Electron. Mater.* 41 (2012).
- [43] J. Yu, W. Zhao, H. Zhou, P. Wei and Q. Zhang, *Scripta Mater.* 68 (2013).
- [44] N. R. Dilley, E. D. Bauer, M. B. Maple and B. C. Sales, *J. Appl. Phys.* 88 (2000).

## CHAPTER V

### Summary

In the present thesis, in order to develop high performance thermoelectric (TE) materials for commercial application as the thermoelectric device, the author studied about the reduction of thermal conductivity in conventional TE materials such as InSb and CoSb<sub>3</sub>. The two approach used in this work to reduce a thermal conductivity were through the synthesis of isostructural solid solution for InSb and `rattling` atoms (phonon glass electron crystal) for CoSb<sub>3</sub> skutterudites.

First of all, in the work on InSb, the polycrystalline samples of InSb-ZnXSb<sub>2</sub> ( $X = \text{Si, Ge, Sn, or Pb}$ ) system and InSb-In<sub>2</sub>XTe ( $X = \text{Si, Ge, or Sn}$ ) solid solutions were prepared by hot-pressing techniques and investigated TE properties. The thermoelectric properties were measured from room temperature to around 723 K. Second, fully dense samples of polycrystalline *p*-type Tl-filled skutterudites having the compositions of Tl<sub>*x*</sub>Fe<sub>1</sub>Co<sub>3</sub>Sb<sub>12</sub> ( $x = 0, 0.2, 0.4, 0.6, \text{ and } 0.8$ ) were prepared by solid-state reaction and hot-pressing techniques, and their high-temperature TE properties were examined. The conclusions of this thesis are as follows:

In order to TE properties at high-temperature of the isostructural and isoelectronic solid solution of InSb, i.e. In<sup>3+</sup> in InSb was partly replaced by Zn<sup>2+</sup> ion and IV<sup>4+</sup> ion, the polycrystalline sample of ZnIn<sub>18</sub>XSb<sub>20</sub> ( $X = \text{Si, Ge, Sn, or Pb}$ ) were prepared by solid-state reaction and hot-pressing. Additionally, the author investigated the TE properties of samples cooled at different rates because it is well known that the performance of TE materials is sensitive to the fabrication conditions and procedure. The XRD patterns of ZnIn<sub>18</sub>XSb<sub>20</sub> ( $X = \text{Si, Ge, Sn, or Pb}$ ) samples, regardless of the cooling rate, exhibited zincblende structure. If these system show perfect stoichiometry, they may be expected to show low  $\kappa$  due to scattering of phonons by point-defect and chalcopyrite structured inclusions in the matrix.

However, such inclusions could not be obtained presumably due to a segregation of the excess Sb or lost as a vapor phase during hot-press process and only Zn doping. In the system of  $\text{ZnIn}_{18}\text{GeSb}_{20}$  prepared by mechanical alloying (MA) and hot-press, the inclusions of chalcopyrite structure were not identified in the InSb matrix, but nano-sized InSb precipitates with the size of 50 ~ 100 nm were observed. It can be confirmed that the samples of  $\text{ZnIn}_{18}\text{SiSb}_{20}$  and  $\text{ZnIn}_{18}\text{GeSb}_{20}$  showed remarkably different microstructure with different cooling conditions. These different microstructures affected the carrier concentration and mobility, resulting in differences in not only the electrical properties but also  $\kappa$  for these samples. Consequently, the  $\text{ZnIn}_{18}\text{XSb}_{20}$  ( $X=\text{Si, Ge, Sn, or Pb}$ ) system could significantly reduce their thermal conductivity owing to effective point-defect phonon scattering by partially replaced In in InSb.

In view of the possibility of cross-substitution in the anionic sub-lattice, an attempt was made to prepare InSb- $\text{In}_2\text{XTe}$  ( $X = \text{Si, Ge, or Sn}$ ) system. These solid solution compounds have been reported to have a zincblende structure. The author prepared solid solution of InSb in which Sb is replaced by (Si, Te), (Ge, Te), and (Sn, Te) and investigated the TE properties at high temperature. All samples were indexed in terms of the zincblende structure with the space group  $F-43m$ . InSb- $\text{In}_2\text{GeTe}$  sample which show semiconductor behavior has larger absolute value of  $S$  than those of InSb- $\text{In}_2\text{SiTe}$  and InSb- $\text{In}_2\text{SnTe}$  of metallic compounds. In this system, although the thermal conductivities were reduced through point-defects, but the TE figure of merit ( $ZT$ ) was not be enhanced compared to InSb.

Finally, in order to reduce a thermal conductivity of  $\text{CoSb}_3$  TE material and develop a  $p$ -type skutterudites, the author prepared polycrystalline samples of  $\text{Tl}_x\text{Fe}_1\text{Co}_3\text{Sb}_{12}$  were prepared and examined their TE properties. The system of  $\text{Tl}_x\text{Fe}_1\text{Co}_3\text{Sb}_{12}$  possesses between  $x = 0.4$  and  $0.6$  of the filling fraction limit. All samples exhibited positive  $S$  values. Tl-adding decreased the hole concentration because the valence of Tl is +1 so Tl-adding compensates the hole concentration doped by the replacement of Fe with Co and thus resulted in increasing the  $\rho$  and the absolute  $S$ . It could be confirmed that the Tl-adding and partial replacement of Fe in Co led to decrease the  $\kappa_{\text{lat}}$  significantly. In the present study, the maximum  $ZT$  was obtained 0.36 at 723 K for  $\text{Tl}_{0.2}\text{Fe}_1\text{Co}_3\text{Sb}_{12}$ . Table 1 shows the optimal concentration from the calculation of the number of holes per formula unit with various compounds. It can be considered that the optimized composition which expected from the

number of holes could not be obtained due to low filling fraction of Tl. Thus, the author suggests further two approach for an improvement of  $ZT$  value. The first approach is to increase the filling fraction limit by an increasing of the amount of Fe. In the  $\text{CoSb}_3$  skutterudite, the filling fraction can increase through the replacement of Fe in Co site. The second approach is the alteration of filling atom from  $\text{Tl}^{+1}$  to  $\text{Na}^{+1}$  ion. Since the ionic radius of  $\text{Na}^{+1}$  is smaller than that of  $\text{Tl}^{+1}$  ion, the filling fraction can increase. Also, if a bivalent or trivalent ion use as the filling atom, the optimal carrier concentration can be achieved through still less amount of filling atoms.

Table 1 Optimal concentration from the calculation of the number of holes per formula unit with power factor at  $ZT_{\text{max}}$  of various compounds.

| Composition  | Filling atom | Fe/Co ratio |     | # of holes <sup>1</sup> | $S^2\sigma$ at $ZT_{\text{max}}$<br>( $\mu\text{Wcm}^{-1}\text{K}^{-2}$ ) | $ZT_{\text{max}}$ | Ref.                 |
|--|--------------|-------------|-----|-------------------------|---|-------------------|----------------------|
|  |              | Fe          | Co  |                         |   |                   |                      |
| $\text{Ce}_{0.9}\text{Fe}_3\text{Co}_1\text{Sb}_{12}$          | Ce (3+)      | 0.9         | 3   | 1                       | 0.3   | 25                | 0.9<br>at 700 K [1]  |
| $\text{La}_{0.9}\text{Fe}_3\text{Co}_1\text{Sb}_{12}$          | La (3+)      | 0.9         | 3   | 1                       | 0.3   | 25                | 0.9<br>at 732 K [2]  |
| $\text{Yb}_{0.7}\text{Fe}_2\text{Co}_2\text{Sb}_{12}$          | Yb (2+)      | 0.7         | 2   | 2                       | 0.6   | 31                | 0.8<br>at 700 K [1]  |
| $\text{In}_{0.25}\text{Fe}_{1.5}\text{Co}_{2.5}\text{Sb}_{12}$ | In (3+)      | 0.25        | 1.5 | 2.5                     | 0.75  | 12                | 0.37<br>at 700 K [3] |
| $\text{Mm}_{0.9}\text{Fe}_{3.5}\text{Co}_{0.5}\text{Sb}_{12}$  | Mm (3+)      | 0.9         | 3.5 | 0.5                     | 0.8   | 31                | 0.84<br>at 700 K [4] |

<sup>1</sup> Calculated the number of holes per formula unit

## Reference

- [1] R. Liu, P. Qiu, X. Chen, X. Huang and L. Chen, *J. Mater. Res.* 26 (2011).
- [2] B. C. Sales, D. Mandrus, B. C. Chakoumakos, V. Keppens and J. R. Thompson, *Phys. Rev. B* 56 (1997).
- [3] K.-H. Park, J.-Y. Jung, S.-C. Ur and I.-H. Kim, *J. Electron. Mater.* 39 (2010).
- [4] L. Zhang and J. Sakamoto, *Mater. Chem. Phys.* 138 (2013).

## Research Achievement

### List of Publications

#### Research articles

1. Reduction in lattice thermal conductivity of InSb by formation of the  $\text{ZnIn}_{18}\text{GeSb}_{20}$  alloy  
Materials Transactions, **53**, 1976 (2012)  
Donghun Kim, Ken Kurosaki, Yuji Ohishi, Hiroaki Muta, and Shinsuke Yamanaka
2. Effect of Cooling Condition on the Microstructure and Thermoelectric Properties of Zn/Si-Codoped InSb  
Journal of Electronic Materials, **42**, 2388 (2013)  
Donghun Kim, Ken Kurosaki, Yuji Ohishi, Hiroaki Muta, and Shinsuke Yamanaka
3. High-temperature thermoelectric properties of *p*-type Tl-filled skutterudites:  
 $\text{Tl}_x\text{Fe}_1\text{Co}_3\text{Sb}_{12}$   
APL Materials, in press  
Donghun Kim, Ken Kurosaki, Yuji Ohishi, Hiroaki Muta, and Shinsuke Yamanaka

#### Proceeding

1. Thermoelectric properties of  $\text{ZnIn}_{18}\text{XSb}_{20}$  ( $X = \text{Si, Ge, Sn, or Pb}$ )  
Proceedings of ECO-MATES 2011, Vo. 2, pp. 141-142  
Donghun Kim, Ken Kurosaki, Yuji Ohishi, Hiroaki Muta, and Shinsuke Yamanaka

### **International Conference**

1. Thermoelectric properties of  $\text{ZnIn}_{18}\text{XSb}_{20}$  ( $X = \text{Si, Ge, Sn, or Pb}$ )  
ECO-MATES, Osaka, Japan, November 28-30 (2011)  
Donghun Kim, Ken Kurosaki, Yuji Ohishi, Hiroaki Muta, and Shinsuke Yamanaka
2. Thermoelectric properties of  $\text{ZnIn}_{18}\text{SiSb}_{20}$  and  $\text{ZnIn}_{18}\text{GeSb}_{20}$   
ICT/ECT2012, Aalborg, Denmark, June 9-12 (2012)  
Donghun Kim, Ken Kurosaki, Yuji Ohishi, Hiroaki Muta, and Shinsuke Yamanaka
3. Thermoelectric properties of the  $\text{InSb-ZnSiSb}_2$  and the  $\text{InSb-ZnGeSb}_2$  alloys  
IUMRS-ICEM 2012, Yokohama, Japan, September 23-28 (2012)  
Donghun Kim, Ken Kurosaki, Yuji Ohishi, Hiroaki Muta, and Shinsuke Yamanaka
4. Microstructure and Thermoelectric Properties of  $\text{ZnIn}_{18}\text{XSb}_{20}$  ( $X = \text{Si, Ge, Sn, or Pb}$ )  
PM2012, Yokohama, Japan, October 14-18 (2012)  
Donghun Kim, Ken Kurosaki, Yuji Ohishi, Hiroaki Muta, and Shinsuke Yamanaka

### **Domestic Conference**

1. Thermoelectric properties of the  $\text{InSb-ZnGeSb}_2$  alloy  
Annual Meeting of the Thermoelectrics Society of Japan (TSJ2011), Hokkaido University,  
Sapporo, Japan, August 8-9, (2011)  
Donghun Kim, Ken Kurosaki, Yuji Ohishi, Hiroaki Muta, and Shinsuke Yamanaka

## Acknowledgments

I would especially like to thank Professor Shinsuke Yamanaka for helpful advices, instructive support, kind guidance and valuable counsels on my study. I was lucky to be his graduate student.

My sincere thank is expressed to the thesis committee, Professor Takao Yamamoto and Associated Professor Hiroshi Nishikawa for their reading and criticizing the manuscript.

The most important contributor in completing my thesis was certainly my advisor Associated Professor Ken Kurosaki. I wish to give my gratitude to him for the instructive support, kind guidance, suggestions and providing me with a better technical understanding of thermoelectricity.

I would also like to thank Assistant Professor Hiroaki Muta, Assistant Professor Yuji Ohishi, and Dr. Aikebaier Yusufu for kind help and constructive comments. My thankfulness is also extended to all members in the Yamanaka Laboratory for their helpful advice and encouragement in my student life. I would like to acknowledgment help of Dr. Chang-eun Kim, Mr. Guanghe Li, Mr. Seong-ho Choi, and my partner, Mr. Do-young Jung.

I wish to express my gratitude to Professor Ki-won Kim in Gyeongsang National University, who gave me encouragement from the beginning of my academic degree. Thanks also goes out to those who provided me with sincere advice for my life; Dr. Seong-in Moon, Dr. Chil-hoon Doh, Dr. Bong-soo Jin, and Prof. Chang-woo Lee.

I am very much indebted to my parents and in-laws, who supported me in every possible way to see the completion of this work. I thank my younger brother' family for always cheering me up. Also, I am very thankful to all of Korean friends in Korea and Japan who have helped me overcome these tough times.

Finally, I would like to thank my wife and son, Jin-kyeong Kim and Ryeon-ho Kim, for their patience and great support in innumerable ways. I might say here cannot do full justice to the extent and the value of her contribution and love.